ORNL/SPR-2023/3025

Comparison between Pin-by-Pin Subchannel and System Level Thermal Hydraulic Results for High Burnup Loss-of-Coolant Applications

Robert Salko
Aaron Wysocki
Belgacem Hizoum
Nathan Capps

August 2023

OAK RIDGE National Laboratory

ORNL IS MANAGED BY UT-BATTELLE LLC FOR THE US DEPARTMENT OF ENERGY

ORNL/SPR-2023/3025

COMPARISON BETWEEN PIN-BY-PIN SUBCHANNEL AND SYSTEM LEVEL THERMAL HYDRAULIC RESULTS FOR HIGH BURNUP LOSS-OF-COOLANT APPLICATIONS

Robert Salko
Aaron Wysocki
Belgacem Hizoum
Nathan Capps

August 2023

Prepared by
OAK RIDGE NATIONAL LABORATORY
Oak Ridge, TN 37831
managed by
UT-BATTELLE LLC
for the
US DEPARTMENT OF ENERGY
under contract DE-AC05-00OR22725

CONTENTS

ABSTRACT

This milestone report summarizes recent work to investigate higher fidelity modeling and simulation practices for large-break loss-of-coolant accident (LBLOCA) analysis in high-burnup pressurized water reactor (PWR) cores. Because of current industry interest in extending fuel cycle lengths ranging from 18 to 24-months, the Nuclear Energy Advanced Modeling and Simulation (NEAMS) program has been investigating the susceptibility of high-burnup core designs to fuel fragmentation, release, and dispersal (FFRD) during accident conditions such as LBLOCA. This work has prioritized developing and demonstrating a methodology for calculating core-wide susceptibility to FFRD and addressing uncertainties identified in the analysis and the US Nuclear Regulatory Commission (NRC) Research Information Letter on FFRD. Part of this investigation seeks to quantify differences between system-level thermal hydraulic behavior and higher fidelity subchannel modeling methods to identify potential safety concerns or opportunities to minimize FFRD susceptibility.

To this end, the NEAMS subchannel code, CTF, is being used, along with the NRC system analysis code TRACE, for analysis of LBLOCA in a core containing high-burnup fuel. This project includes two thrusts: (1) improving on the existing TRACE model for a 4-loop PWR for LBLOCA so that the model is higher fidelity and consistent with current USNRC best practices, and (2) using CTF to perform pin-resolved modeling of the core region of the reflood phase of a LBLOCA in a high-burnup PWR.

Although CTF includes a wide range of closure models for modeling LOCA conditions, these models have not been assessed during recent CTF development activities, so the first step is to validate CTF using loss-of-coolant accident (LOCA) reflood experiments. A sensitivity study was also performed to identify high-impact models, which were then reviewed and corrected as needed. To strengthen the assessment, a code-to-code benchmark was performed against TRACE for these conditions. Both high- and low-flooding rate tests from the FEBA reflood experiments were modeled using lumped and pin-resolved CTF models, and the models were compared against lumped pin TRACE results. The lumped CTF and TRACE models demonstrated good agreement with experimental peak cladding temperatures (PCT) for all axial levels except near the top of the bundle. CTF pin-resolved PCT predictions were good for all thermocouple locations except for those facing the center subchannel, which were predicted to be about 40 K too low. A study on radial effects on the pin-resolved model was performed, and advanced CTF spacer grid droplet breakup and quenching models were tested to demonstrate the impact on better cooling the top of the bundle for better agreement with experimental data.

Several modifications and improvements were made to the full-system TRACE model in this work, to better align the model with industry and NRC best practices and improve the accuracy of the LBLOCA predictions. This included converting to the best-practice 3D vessel component in TRACE, increasing the radial and azimuthal fidelity within the core and vessel, discretely modeling all four primary loops in the system, improving the fuel rod heat conduction modeling approach, and accounting for additional burnup effects. The updated model exhibited greatly improved agreement with published results from the BEMUSE international LBLOCA benchmark study, in terms of both the peak PCT and the quench time of the hot rod. A step-by-step assessment was done to quantify the sensitivity of LBLOCA predictions to various modeling options and approaches.

The updated TRACE full system analysis also showed that radial thermal-hydraulic (TH) effects are important on a core-wide scale, particularly in terms of capturing the different average power levels in the core periphery and core interior, as well as the impact this has on the TH conditions of the high burnup rods. However, the cladding temperature variation between rods was relatively small within a given core radial and azimuthal region, which was attributed to the lack of local subchannel and neighboring assembly effects in the TRACE model. This reinforced the importance of using a high-fidelity code such as CTF to accurately predict such variations on a pin-by-pin level.

To investigate the impact of high-resolution LOCA modeling and to assess CTF's ability to model core-scale pin-resolved LOCA problems, a subregion (9 assemblies in a 3 × 3 configuration) of an existing high-burnup PWR core was modeled in three ways: (1) using a TRACE lumped model (one channel per assembly), (2) a CTF lumped model (one channel per assembly), and a CTF pin-resolved model (18 × 18 subchannels per assembly). The subregion was centered around a high-burnup assembly with neighboring high- and low-burnup assemblies and used the 3D power distribution at the end of the cycle as calculated by a VERA depletion simulation. Boundary conditions and total core power were set to LOCA reflood conditions. The TRACE and CTF lumped models were used to show agreement between the codes when using a similar meshing approach, and the pin-resolved CTF model was used to show the impact of using high-resolution modeling compared to the lumped approach. Findings from this study show that (1) the pin-resolved model achieves higher peak cladding temperatures because of local TH effects, (2) the neighboring low-burnup assemblies impact the value and distribution of PCT in the high burnup assemblies, and (3) the PCT values in high-burnup assemblies generally vary by as much as 50 K between the coolest and hottest pins in the assembly. Although the first finding suggests higher PCTs in certain rods, the latter suggest cooler temperatures in other rods. This is critical when considering FFRD susceptibility as a function of terminal temperature, which indicates that a subchannel tool may result in less FFRD simply because of calculating lower temperatures in certain regions of the core.

1. INTRODUCTION

The nuclear industry is developing a technical basis for extending fuel cycles from 18to 24 months to improve the economic viability of the nuclear fleet. However, longer cycles will result in fuel with discharge peak rod average burnups as high as 75 GWd/MTU (Capps, et al., 2021). This may require additional considerations with respect to potential design basis accidents. One potential issue involves the tendency of the high-burnup UO_2 fuel pellets to pulverize, which makes it more likely that fuel will be dispersed from the fuel cladding during a loss-of-coolant accident (LOCA). This could lead to the fuel being in an unknown geometry, which could impact coolability and criticality and which could also increase radiological release following the rupture. This phenomenon is known as *fuel fragmentation relocation and dispersal* (FFRD).

Some tests were performed to investigate this concern. In-pile LOCA tests were performed at the Halden Reactor on rod segments with very high burnup (92 GWd/MTU). These tests found finely pulverized fuel relocated into the balloon geometry (T. Fuketa, 2010). Out-of-pile tests were also performed at Studsvik Nuclear on rodlets closer to existing burnup conditions which also found finely fragmented fuel pellets; however, the fuel fragments were noticeably larger in the low-burnup rodlets (Flanagan, Askeljung, & Purana, 2013). It was found that higher burnup fuels experienced more fuel pulverization during a LOCA transient.

A large-break LOCA (LBLOCA) is one of the most severe accidents that can occur in a light-water reactor (LWR). In a pressurized water reactor (PWR), the transient starts from a break in the cold leg of the coolant system which results in rapid depressurization of the core as coolant escapes from the primary system. The voiding of the core is caused by liquid flashing to steam and escaping from the system. This results in heat-up of cladding because of significantly reduced heat transfer, as well as the presence of decay heat in the fuel rods. The LBLOCA progresses in three phases, commonly known as depressurization, refill, and reflood.

The depressurization phase starts after the break occurs and involves coolant escaping the system and primary system pressure dropping to containment pressure (near atmospheric). The refill phase starts when accumulators engage and begin refilling the lower plenum with subcooled liquid. The reflood phase begins once the subcooled liquid begins to fill the core region and quench the hot fuel. The peak cladding temperature (PCT) in the core will be encountered during the reflood phase of the transient. During this phase of the transient, several complex and interdependent phenomena, such as droplet entrainment, radiative heat transfer, and spacer grid effects, will determine the magnitude of the PCT and the amount of time it takes for the rods to be quenched. The combination of core depressurization, relatively high internal rod pressure, and increasing rod temperatures (reduced mechanical strength of the cladding) can lead to cladding ballooning and rupture, which can lead to dispersal of radioactive fuel particles.

The NEAMS program has been working with the US Nuclear Regulatory Commission (NRC) and the nuclear industry to investigate this problem, to support disposition of FFRD susceptibility, and to identify margin opportunities. Ultimately, the onus will be on the industry to develop topical reports for dispositioning FFRD susceptibility as a safety concern. In a previous study on FFRD, RELAP5-3D was used to perform a large-break LOCA analysis for a high-burnup core that was modeled by VERA (Capps, et al., 2021). The RELAP5-3D results were used as boundary conditions for BISON (Hales, et al., 2016)

simulations of limiting rods in the core, which was then used to determine fuel pulverization susceptibility and the likelihood of fuel rod rupture in high-burnup fuel rods. A standard coarse-mesh two-channel/pin modeling approach was used in the RELAP5-3D model in this analysis, which uses one pin/channel for representing limiting rods (high-burnup and high power) and another one for representing the remainder of the pins. However, this meshing approach fails to capture radial non-uniformity in the core power distribution and local thermal-hydraulic (TH) behavior.

Previous NEAMS work identified burnup, linear heat rate (LHR), and fuel rod performance gradients in high-burnup fuel which may impact the transient TH, transient fuel performance, and ultimately, FFRD susceptibility. Therefore, the purpose of this milestone is to improve on the TH analysis of the high-burnup LOCA transient in order to minimize FFRD susceptibility. First, a more advanced system model will be developed in the TRACE system analysis code in collaboration with the NRC and second, CTF will be used for analysis of the core region using a much higher pin-resolved modeling approach capable of capturing local TH and crossflow effects. This milestone also seeks to investigate the differences between the different meshing approaches (coarse mesh vs. pin-resolved) as well as to assess the differences between the CTF and TRACE LOCA modeling packages.

In addition to these high-level goals, a natural secondary goal is to perform a preliminary assessment of CTF for modeling of LOCA conditions. CTF was developed from the COBRA/TRAC code (Thurgood, Kelly, Guidotti, Kohrt, & Crowell, 1982), which was developed for modeling of LOCA conditions, so CTF already has many models needed for LOCA analysis; however, no work has been performed to date to assess the version of CTF maintained and developed at Oak Ridge National Laboratory (ORNL), so some baseline validation work is needed to provide assurance in CTF's capabilities for this new application. Because the LOCA transient requires a complex range of conditions and resources are limited, efforts are focused on assessing modeling of the reflood phase of LOCA only, as this is the phase where PCT will be encountered. Although the TRACE version employed for this work has been validated in the past, some assessment is also performed as described here to test the sensitivity of different models and to benchmark against CTF and experimental LOCA results.

In Section 2, the codes CTF and TRACE are introduced. In the CTF section, the models relevant for LOCA analysis are discussed. In Section 3, the experiments that were used for validation of CTF and TRACE are introduced, the CTF and TRACE models of the facility are discussed, and the results of sensitivity analyses on CTF and TRACE are shown to determine the most important models for LOCA reflood analysis. The section also presents the validation results for CTF and TRACE using flooding experiments with blocked array (FEBA) tests, as well as code-to-code benchmark results and a more in-depth analysis of the impact of different CTF models. Section 4 presents results of a core-scale reflood transient for a core containing high-burnup fuel. In this section, the impact of using pin-resolved over a coarse meshing approach is investigated. Section 5 shows results of a TRACE full core and loop model of the BEMUSE benchmark, which is an updated version of the model from a previous milestone on this work. Finally, a summary of findings in this report is presented in Section 6.

2. SUMMARY OF THERMAL HYDRUALIC CODES

2.1 CTF

CTF is a subchannel TH code developed by ORNL and North Carolina State University (Salko, et al., 2022). CTF is a modernized version of the COBRA/TRAC code (Thurgood, 1982). CTF includes most of the features of that code plus several new ones. CTF uses a two-fluid model for two-phase flow with a separate field used for tracking droplets in the system. This allows the continuous liquid and droplets to move at different velocities. CTF models crossflow between subchannels because of pressure gradients, turbulent mixing diffusion, and void-drift. A thermal conduction model is also included for predicting temperature in solid objects in the model, which includes tubes, solid rods, slabs, and nuclear fuel rod geometries. An advanced set of solvers is included for predicting dynamic pellet and clad behavior caused by thermal expansion and irradiation effects.

The bulk of CTF development work was performed under the Consortium for Advanced Simulation for Light Water Reactors (CASL) program (Kropaczek, 2020), which focused on developing the code for modeling of PWR operating conditions. There was some focus on modeling of fast transients such as reactivity insertion accident (RIA) modeling, but the code was assessed for pre-critical heat flux (CHF) conditions only. An industry funding opportunity announcement (iFOA) program allowed for further development of the code for boiling water reactor (BWR) under normal operating conditions (pre-dryout) (Salko, 2021). Whereas most of the development work focused on pre-CHF and pre-dryout conditions, CTF includes a series of models for modeling of post-CHF and LOCA conditions, although these models have not been assessed. One objective of this project is to assess the CTF LOCA models, thus ensuring their proper implementation and functioning. Because of time constraints of the project and the large scope of LOCA modeling, the assessment focused on reflood conditions and determination of the most important models requiring review through means of a sensitivity analysis.

Figure 1 presents an overview of the important phenomena that shall be considered during a LOCA reflood transient (R. Salko, 2023). There are two layers of categories in the plot: major (orange with a dashed line border) and minor (yellow with a solid line border). The solid yellow categories are models used for the following validation study, whereas the categories with a striped background were not assessed or enabled for the current study. However, the intent is to evaluate these models in future work. The black lines denote ownership of each subcategory, and the red dashed arrows denote a relationship between categories. For example, the figure shows that entrainment phenomena will impact the interfacial area in the model, as entrainment affects total amount of droplets in the flow. Likewise, interfacial area impacts interfacial drag and interfacial heat transfer.

In the case of interfacial heat transfer area and drag, the subcategories are mostly flow regimes that are encountered. Each flow regime will include its own set of closure models. For interfacial area, the flow regime defines the geometry of the flow fields and which geometric relationships should be used to determine interfacial area. For interfacial heat transfer, the flow regime determines which interfacial heat transfer coefficient correlation shall be used. One exception is the non-condensable gas model, which is modeled using a separate governing equation solved by CTF alongside the other primary governing equations to track total gas content of the fluid. This will impact interfacial heat transfer.

The entrainment models also consider different scenarios that can occur during the transient. Quench front includes models for droplet entrainment that occurs as the quench front moves up through the core. The remainder of the models are de-entrainment models which capture effects such as droplet de-entrainment in area changes and into the film.

The spacer grids play an important role in LBLOCA. As stated previously, the grids can quench earlier than the rods which will impact the magnitude of PCT and its location in the core. For this reason, CTF includes a grid quenching model, which tracks the balance of droplet de-entrainment into the grid film and film evaporation. The film evaporation will also cool the vapor and affect rod heat transfer. The droplet breakup will also affect the interfacial area, which in turn affects interfacial heat transfer and drag. The grids can directly cool the rods through radiative heat transfer if the model is enabled. The grids can also directly enhance vapor turbulence, which enhances cooling of the rods.

Rod heat transfer models are the direct heat transfer mechanisms between the vapor/liquid/droplets and the rods. These include convective heat transfer (either to single-phase liquid or vapor), subcooled or nucleate boiling, dispersed flow film boiling (DFFB), inverted annular film boiling (IAFB), and transition boiling. CTF implements two types of models for film boiling: IAFB and DFFB. IAFB is used when liquid content is high (low vapor content), and DFFB is used when liquid content is low (high vapor content). Determining which model to apply depends on the CHF and the minimum film boiling (MFB) temperature calculation. There are two types of radiative heat transfer: in the first case, the rods can directly transfer heat to other rods and spacer grids, and in the second case, the rods can transfer heat to the three different fields—film, droplets, and vapor. In the first type of heat transfer, the user must manually define the model geometry in the input file, whereas in the second type of heat transfer, the model is automatically applied without such information if enabled. Droplets can create turbulent enhancement of the vapor phase convective heat transfer and can also directly impinge on the surface of the rod.

Finally, a generic category called “Other” lists two features that relate to CTF LOCA modeling. Adaptive meshing allows the code to refine the rod mesh in the region of the quench front. This allows for more accurate modeling of the steep temperature gradient and drastic changes in closure models in the vicinity of the quench front. The three-field model denotes that CTF uses three sets of momentum equations—one for each of the three fields recognized by CTF. This solution approach was inherited from COBRA-TF, which applied the method specifically for capturing the important role played by droplets in LOCA modeling.

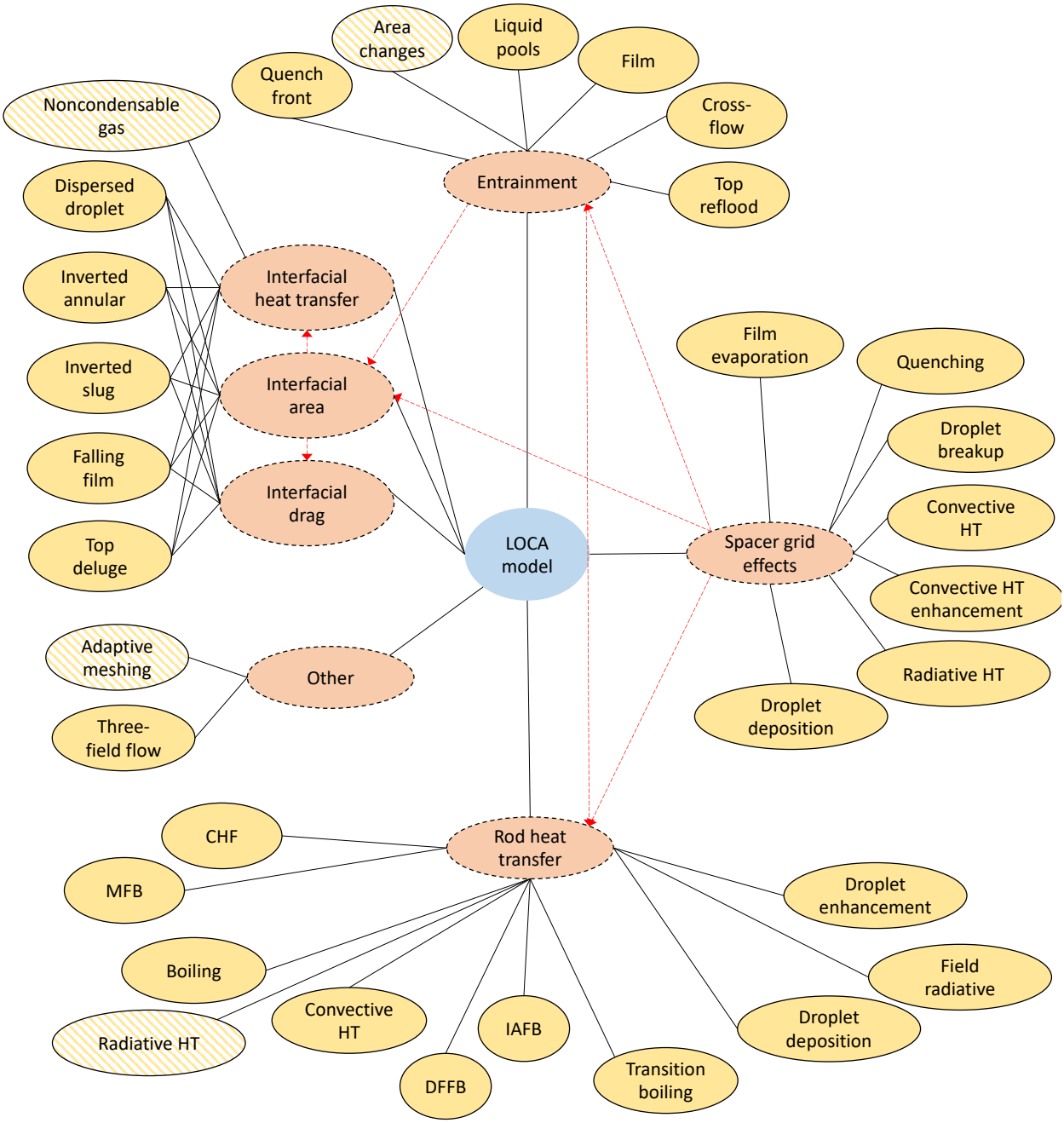

Figure *1*. Diagram of models included in CTF for modeling of LOCA conditions.

2.2 TRACE

TRACE is a best-estimate TH systems code developed by the NRC. The capabilities of prior systems codes TRAC-P, TRACE-B, RELAP5, and RAMONA were brought into TRACE as a more modernized computational tool (Bajorek, et al., 2015).

TRACE is applicable to a wide range of LWR operational and accident scenarios. This includes both small and large break LOCAs. The TRACE Assessment Manual defines small break LOCAs as having break flow areas between 7.125×10^{-5} and 0.7854 m^2, which is large enough to depressurize the primary system to the high pressure safety injection setpoint but not large enough to quickly reach the accumulator setpoint. Breaks larger than 0.7854 m^2, up to a double guillotine break of the primary leg, ar

e considered large break LOCAs (US Nuclear Regulatory Commission, 2012). The code's applicability to these conditions has been ensured through an extensive code assessment, verification, and validation process. For LBLOCAs, these efforts were guided by three LBLOCA-specific phenomena identification and ranking tables (PIRTs) (Shaw, Larson, & Dimenna, 1988) (Young, Bajorek, Nissley, & Hochreiter, 1998) (Martin & O'Dell, 2005). Important phenomena were identified across all major phases of LBLOCA events—blowdown, refill, and reflood—and were used to inform the TRACE validation and development efforts. The result was an extensive set of fundamental, separate effects, and integral tests for LBLOCA. An independent assessment was performed and concluded that TRACE provides reasonable agreement to these experimental data for LBLOCA, including correct prediction of LBLOCA trends with minor deficiencies noted in a few constitutive models (US Nuclear Regulatory Commission, 2012) (US Nuclear Regulatory Commission, 2022).

The TRACE solution approach is generally similar to the CTF solution approach in most important respects for LOCA modeling. Both codes solve conservation equations for the liquid and vapor phases separately. One difference is that CTF also solves conservation equations for the droplet phase and includes some more advanced models related to droplet behavior (e.g., droplet breakup on spacer grids, spacer grid quenching, and droplet interfacial area tracking). Each code employs a similar flow regime and heat transfer regime structure spanning single- and two-phase conditions, although the codes often use different models for modeling interfacial drag, interfacial heat transfer, and wall heat transfer.

The pre- and post-CHF heat transfer regime structure is also similar. Both codes calculate a "CHF temperature" based on closure models and compare the fuel outer surface temperature to this value. In both codes, if the surface temperature exceeds the CHF temperature, then the post-CHF heat transfer regime is entered. Both codes also divide the post-CHF heat transfer regime into transition boiling, inverted annular film boiling, and dispersed flow film boiling regimes. The pre-CHF heat transfer regime is reentered once the surface temperature drops below a rewet temperature based on additional closure models.

Because of TRACE's broad validation base and extensive previous applications to LOCA, this code is well-suited to performing the full core LBLOCA analyses shown in this report, and it is also suitable for providing a useful reference point against which to assess CTF's LOCA performance. The similar solution methodology employed in both codes also allowed direct code-to-code comparison for specific phenomena which helped highlight modeling differences and direct the CTF modeling improvement efforts.

3. CODE VALDIATION USING THE FEBA EXPERIMENT

An important part of this project was to assess the models in CTF that support modeling of LOCA conditions. Comparing the code predictions to experimental data is one of the primary ways in which this assessment is performed. A few experimental databases are available for validation, but the Flooding

Experiments with Blocked Arrays (FEBA) tests were selected for initial assessment because the experimental data is publicly available, provides important measurements for reflood conditions, and has been used in the past for assessment of CTF LOCA models.

3.1 DESCRIPTION OF FEBA TESTS

The FEBA tests were performed in the early 1980s by Institut für Reaktorbauelemente Projekt Nukleare Sicherheit (Ihle & Rust, FEBA---Flooding Experiments with Blocked Arrays Data Report 1, Test Series I through IV, 1984), (Ihle & Rust, FEBA---Flooding Experiments with Blocked Arrays Evaluation Report, KfK 3657, 1984). The tests involved quenching a 5×5 rod bundle test section initially filled with steam to simulate a LBLOCA reflood transient. The pins are instrumented with multiple thermocouples at different azimuthal and axial locations. The housing is also instrumented with thermocouples, as well as a selected subchannel in the bundle. Four pressure taps are used to collect pressure drop data in the lower, middle, and upper portions of the bundle. Droplet carryover at the bundle exit is also measured during the transient.

A primary goal of these tests was to investigate the impact of flow blockages in the bundle. In a LBLOCA, it is possible for rods to balloon and block channels, so tests such as FEBA are employed to provide a better understanding of the effects of this behavior. Another goal was to better understand the effect of spacer grids on the reflood behavior. With these goals in mind, eight series of tests were performed. Test series I and II were performed in a bundle with no flow blockages. Test series II had one spacer grid removed in the middle of the bundle so that results could be compared to those of Test series I to assess the impact of the spacer grid. Test series III–VIII had different variations of flow blockages to assess their impact. Only Test series II was used for initial CTF assessment. Test series II included test cases performed at 2, 4, and 6 bar pressure, as well as flooding velocities of 3.8 and 5.8 cm s^{-1}. The axial power shape for all cases was nonuniform, and the power level was set to simulate decay heat. Test case 229 was chosen for initial assessment of the CTF LOCA capabilities. To test the impact of flooding velocity, Test case 228 was also modeled.

Figure 2, which is reproduced from the FEBA specification (Ihle & Rust, FEBA---Flooding Experiments with Blocked Arrays Evaluation Report, KfK 3657, 1984) shows some of the important bundle geometry and measurement probe locations. The figure shows there are seven spacer grids and provides the location of the bottom edge of the spacer. Note that Test Series II has the middle spacer grid removed. Additionally, the axial locations of all rod thermocouples are shown; rods are identified as Type a through k, but note that not all thermocouples were present in all tests that were run. The axial shape of the power is shown by the shaded figure. The figure also shows the four pressure tap locations, as well as axial locations of fluid and housing thermocouples. Not all fluid and housing thermocouples were used in all tests.

Figure 3, which is reproduced from the FEBA specification (Ihle & Rust, FEBA---Flooding Experiments with Blocked Arrays Evaluation Report, KfK 3657, 1984) shows the top-view of the rod bundle with the thermocouple type letter of each pin identified. Furthermore, each pin is broken into four sectors, each with a numerical identifier ranging from 1—4. The axial location of each of these thermocouple types and azimuthal locations are shown in **Table** 1. **Figure** 4, which is reproduced from the FEBA specification (Ihle & Rust, FEBA---Flooding Experiments with Blocked Arrays Evaluation Report, KfK 3657, 1984) shows the top view of the rod-bundle with dimensions included. Note that this figure shows an example of a bundle with the blockage sleeve applied, but the blockage sleeve was not included in the test run by CTF.

Figure 5, which is reproduced from the FEBA specification (Ihle & Rust, FEBA---Flooding Experiments with Blocked Arrays Evaluation Report, KfK 3657, 1984) shows details of the outlet of the rod-bundle. Note there is a large upper plate with orifices that the flow must move through and then a diversion plate that forces the flow laterally prior to it moving out of the top of the facility. The diversion plate facilitates the capture and collection of the entrained droplets, which are then stored in a tank with a maximum capacity of 10 kg. This tank allows for measurement of droplet carryover during the transients.

Figure 6, which is reproduced from the FEBA specification (Ihle & Rust, FEBA---Flooding Experiments with Blocked Arrays Evaluation Report, KfK 3657, 1984) shows the composition of the heater rods and the placement of the thermocouple used for measurement of the pin surface temperature.

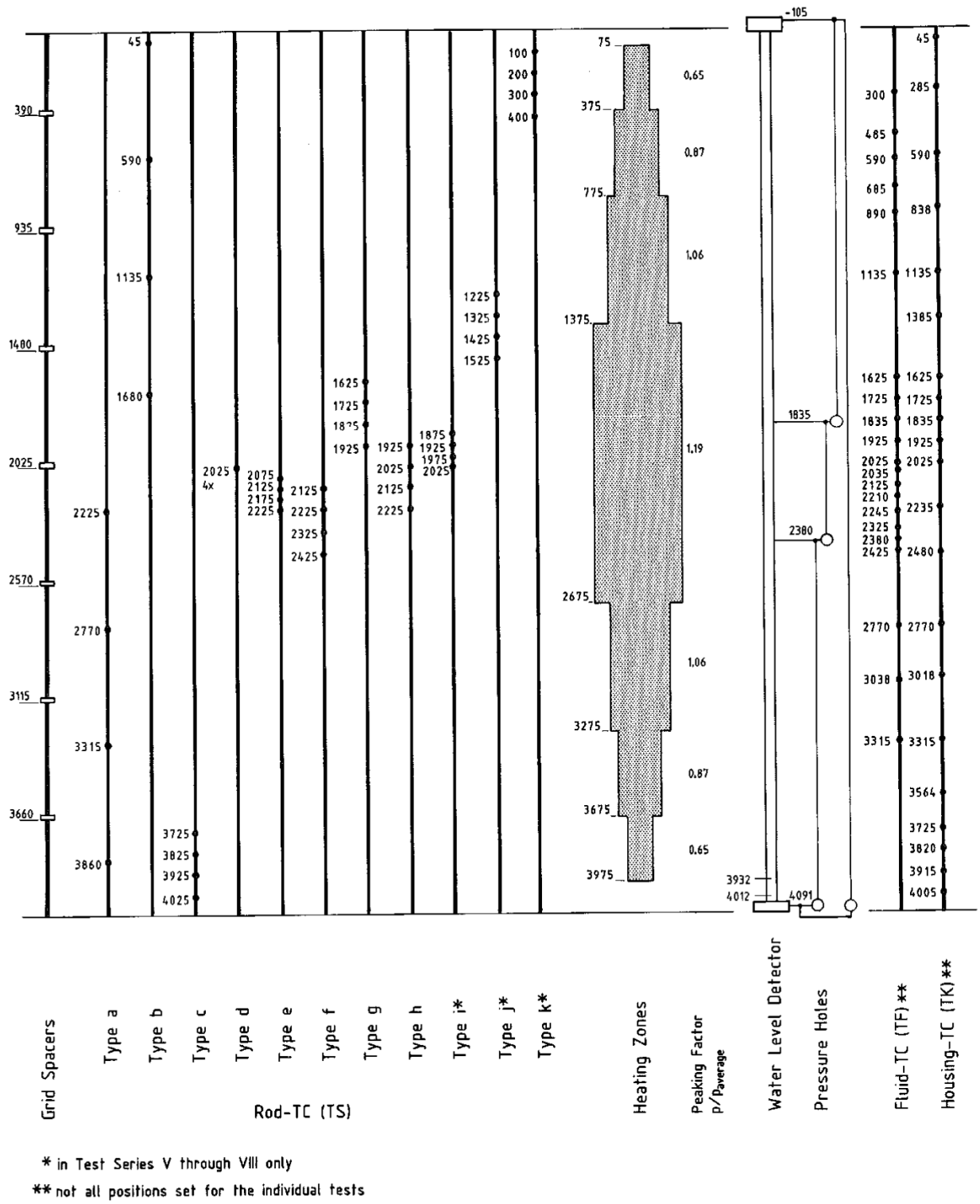

Figure *2*. FEBA Test section geometry and measurement locations.

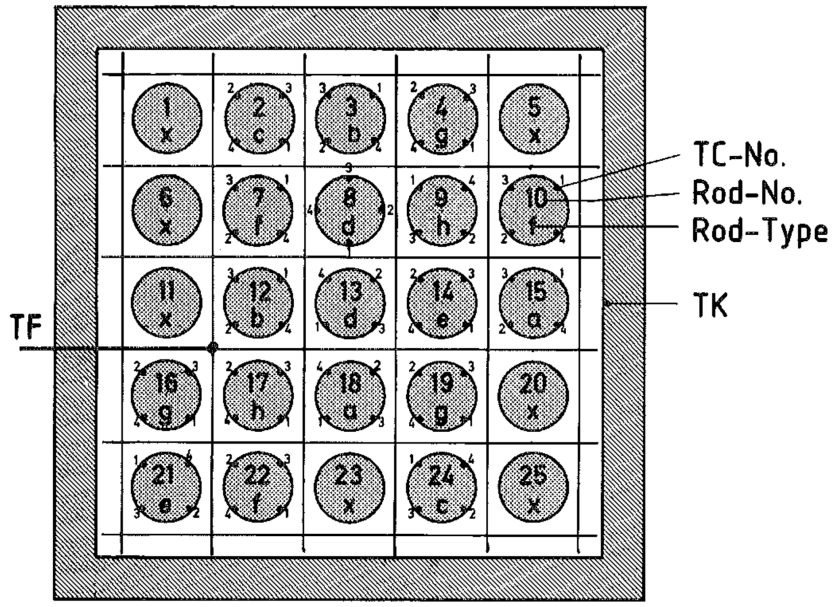

Figure *3*. Top view of FEBA rod bundle and housing.

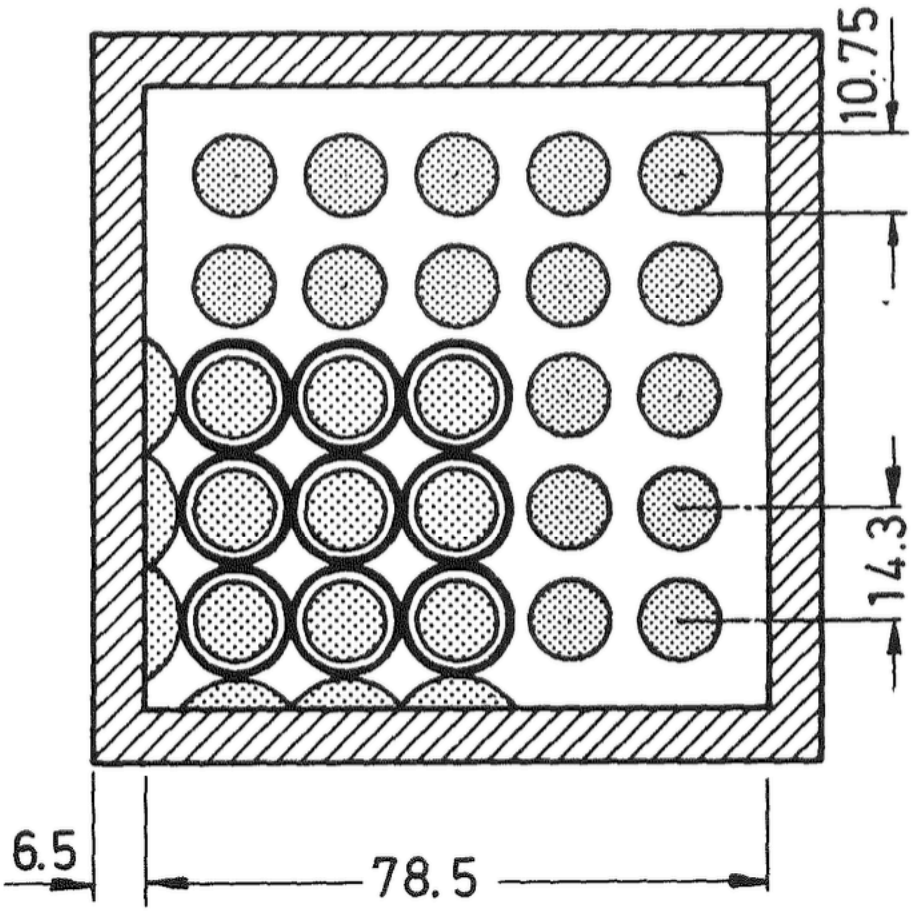

Figure *4*. Top view of the FEBA rod-bundle with dimensions provided in mm.

Table *1*. Rod thermocouple locations

Rod type	TC number	Axial level [mm]
a	1	2,225
	2	2,770
	3	3,315
	4	3,860
b	1	45
	2	590
	3	1,135
	4	1,680
c	1	3,725
	2	3,825
	3	3,925
	4	4,025
d	1	2,025

	2	2,025
	3	2,025
	4	2,025
e	1	2,075
	2	2,125
	3	2,175
	4	2,225
f	1	2,125
	2	2,225
	3	2,325
	4	2,425
g	1	1,625
	2	1,725
	3	1,825
	4	1,925
h	1	1,925
	2	2,025
	3	2,125
	4	2,225

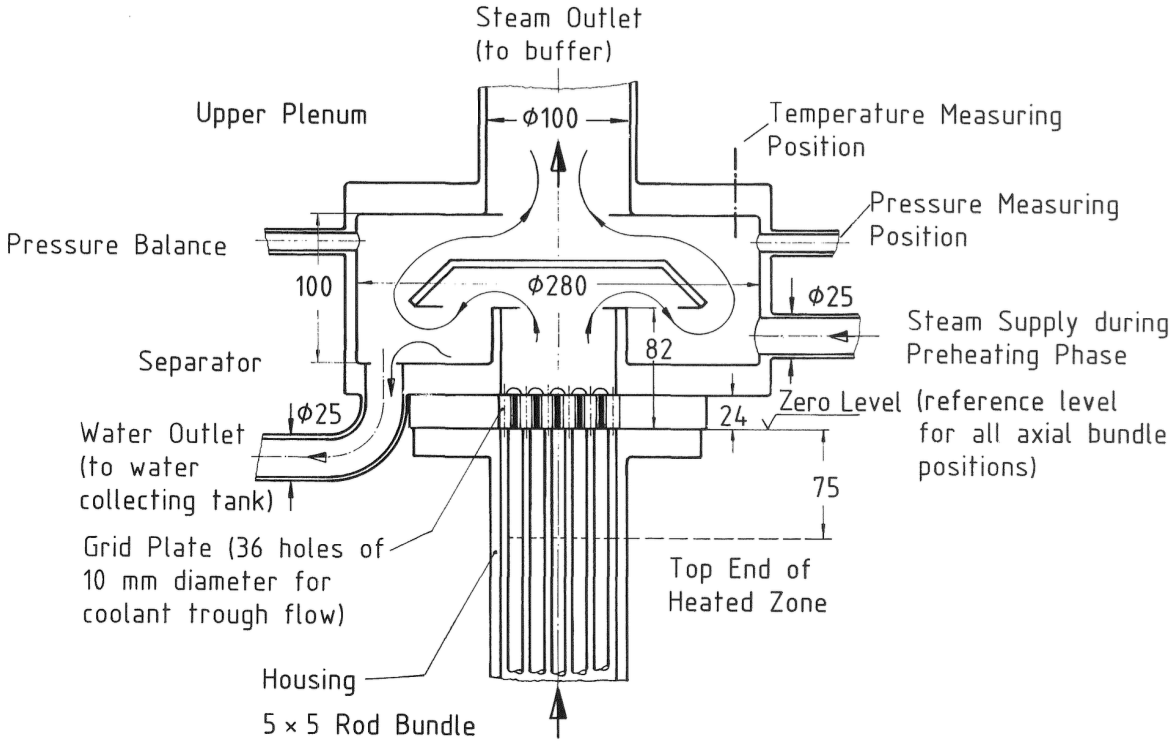

Figure 5. Details of the outlet of the FEBA rod bundle.

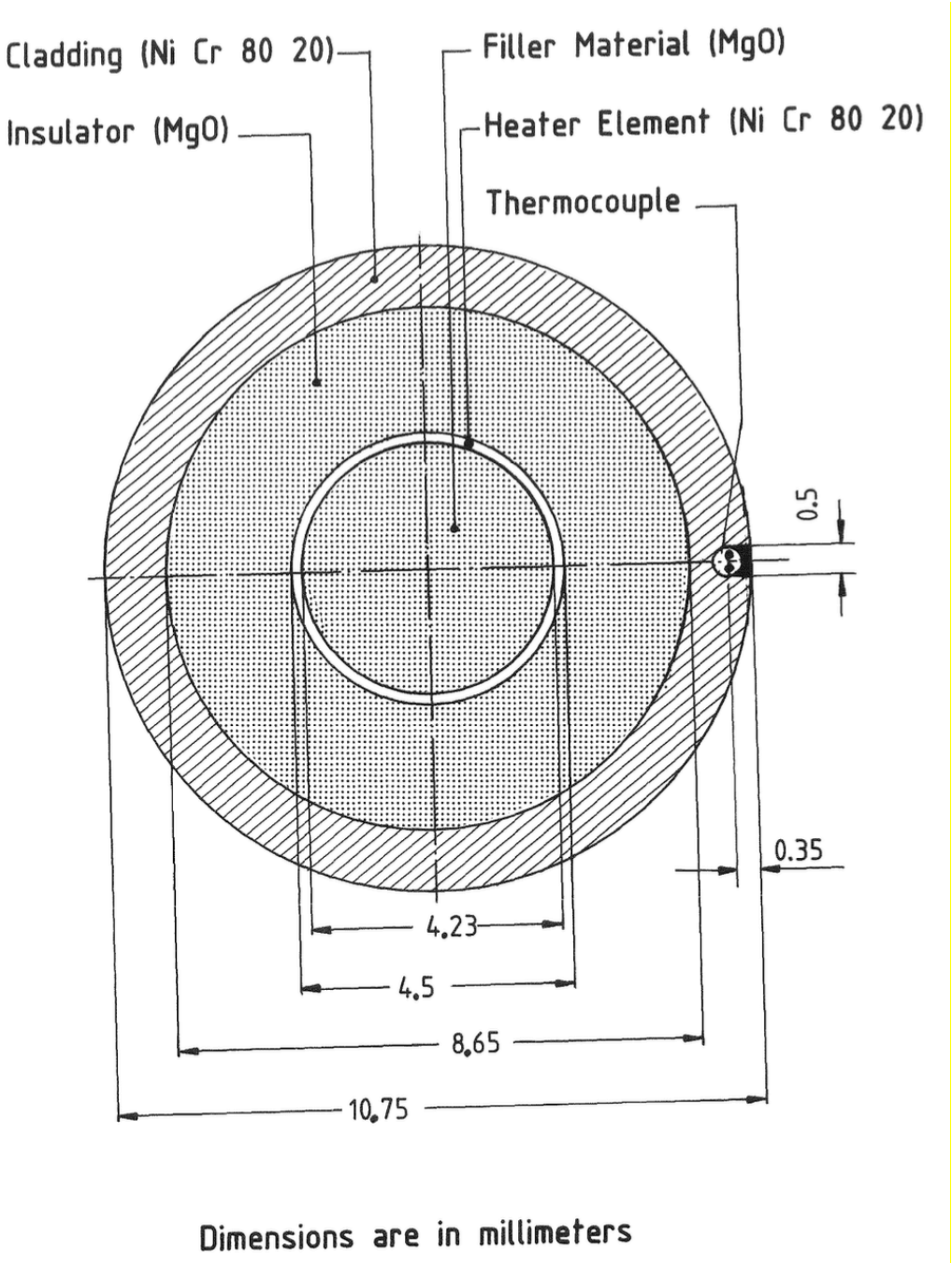

Figure 6. Composition of heater rods in FEBA.

3.2 DESCRIPTION OF THE CODE MODELS

3.2.1 CTF Models of FEBA

Two types of models were created for the facility: one model is the coarse-mesh model, which includes one representative subchannel and pin, and the second model is a pin-resolved model, meaning it resolves each pin and subchannel in the FEBA rod-bundle geometry. For the pin-resolved model, a 1/8 symmetry model was created because the FEBA Series II tests are radially uniform. The CTF model is shown in

Figure 7. The pin numbers in the CTF model are provided (1—6). The 1/8th symmetric CTF model is the region between the red dashed lines. The locations of the remapped thermocouple names (originally shown in Figure 3) are provided as well. For example, the 19g2 thermcouple maps to the 3a location in the CTF model. The dark gray boxes surrounding the figure are unheated conductor objects, which are used to model the impact of the experimental housing. The coarser lumped model simply includes one pin, one channel, and one unheated conductor for the experimental housing. Full symmetry is employed for the lumped model. A multiplier is used on the single pin to ensure total heat output from the pins are correct.

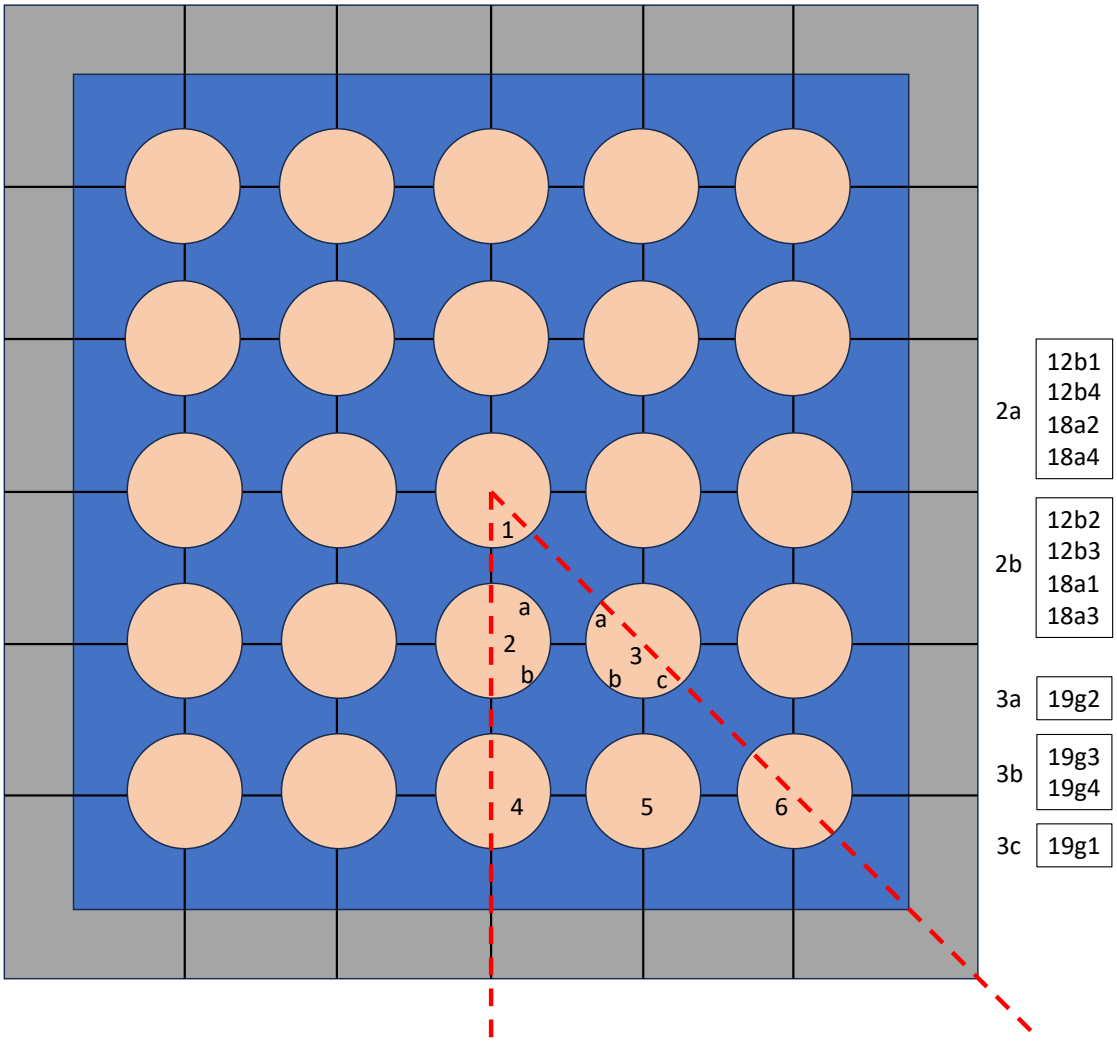

Figure 7. Diagram of the 1/8 symmetry pin-resolved FEBA model in CTF.

The axial mesh was the same in both lumped and pin-resolved models. A uniform mesh was employed with 41 axial levels, resulting in mesh cell heights of 10.23 cm. The CTF model starts at 13.9 cm below the beginning of heated length and ends at 8.2 cm above the end of heated length. The lower end of the housing corresponds to 13.9 cm below the beginning of heated length. As shown in Figure 5, the top of the model corresponds to the end of the bundle channel just before the droplet collection plate.

It was not possible to match grid axial locations or thermocouple axial locations perfectly with their experimental locations because the axial mesh was uniform. The mesh bounds also do not correspond to the beginnings and ends of different heating regions, but CTF internally integrates the provided axial power factor tables to ensure that total power to each mesh cell is consistent with the input and experimental data. **Figure *8*** shows a rough drawing of the scalar mesh cells (black boxes), the location of the heated region (blue box), and the location of the spacer grids and top grid plate. The drawing is not to scale, but indicates that spacer grids and locations of beginning and end of heated length do not perfectly align with the mesh boundaries. **Table** 2 shows the location of spacer grids in the model compared to their experimental locations. Note that the locations are measured from the bottom of the model instead of the top of the model, as was done in the FEBA report and **Figure** 2. **Table** 3 shows the location of thermocouples in the CTF model compared to their experimental location counterparts. **Table** 4 shows the location of pressure taps compared to their experimental location counterparts.

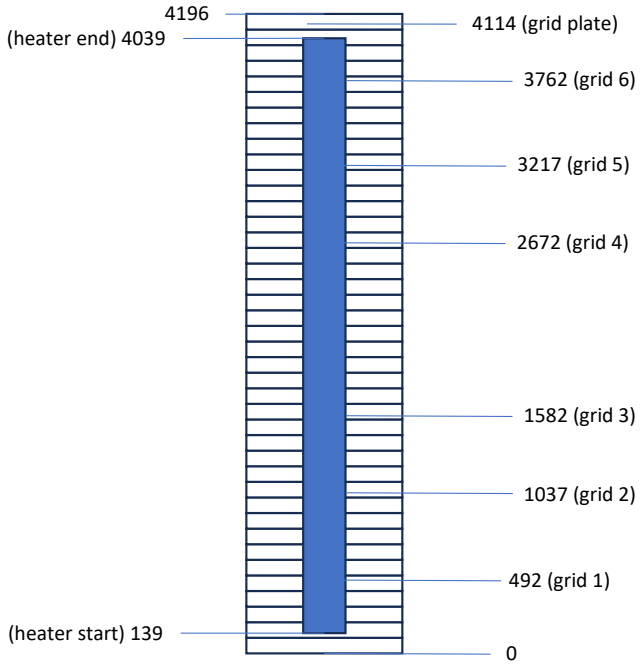

Figure 8. Diagram of axial mesh used, location of heated region (blue box), location of spacer grids, and location of top grid plate.

Table *2*. Location of spacer grids in CTF model (location measured from bottom of the model)

Spacer grid number	CTF grid location [mm]	Experimental grid location [mm]
1	512	492
2	1023	1037
3	1535	1582
4	2661	2672
5	3173	3217
6	3786	3762

Table 3. Location of thermocouples in CTF model compared to experimental location (location values with reference to bottom of CTF model)

Thermocouple	CTF axial location [mm]	Experimental location [mm]
18a4	256	254
18a3	768	799
18a2	1,382	1,344
18a1/7f2	1,893	1,889
19g2	2,405	2,389
12b4	2,405	2,434
12b3	3,019	2,979
12b2	3,531	3,524
12b1	4,042	4,069
Housing	2,354	2,389

Table 4. Location of pressure taps in CTF model compared to experimental locations (locations given with respect to bottom of CTF model)

Pressure tap	CTF axial location [mm]	Experimental location [mm]
1	51	23
2	1791	1734
3	2303	2279
4	4145	4219

As shown in Figure 5, there is an orificed plate at the top of the bundle. An attempt was made to model the flow area contraction and expansion in the CTF model; however, stability issues were encountered during the transient and so this feature was removed for future analysis. It is anticipated that this feature will cause droplet de-entrainment and possible top-quenching of the model.

The spacer grids were modeled using an explicit form loss coefficient of 1.4. The FEBA documentation provided insufficient detail to determine the actual form loss coefficient, and no form loss coefficient was provided by the authors, so this estimated value was used instead. It is anticipated that the form loss coefficient will have a relatively low impact on the solution pressure drop due to the low velocity of the fluid in reflood conditions.

The grid-spacer heat transfer enhancement model in CTF, which uses the Yao-Hochreiter-Leech model, was enabled. The FEBA documentation stated that the grid spacers had a 20% blockage ratio. This was divided evenly in the CTF grid model, so the springs represented 10% blockage and the strap represented the remaining 10% blockage. The mixing vane portion of the Yao-Hochreiter-Leech model was disabled so that mixing vanes do not provide additional heat transfer enhancement.

The base CTF model does not include the impact of grid quenching or grid droplet breakup because of the limited information on spacer grid design. However, an additional model was created to investigate the impact of this model using estimated grid parameters. For this additional model, the spacer grid height is set to 3.8 cm, and the total spacer grid's wetted perimeter is set to 1,884 mm. This was calculated by considering the bundle pitch is 78.5 mm and by assuming the strap spans the entire length for each row of subchannels, of which there are 6. Considering there are two sides per strap, a total wetted perimeter for all rows is 942 mm. The straps also span the orthogonal direction in the 6 columns of subchannels, which doubles the total wetted perimeter to 1,884 m. The strap thickness is assumed to be 0.5 mm.

The heater pins are modeled using a multi-region solid rod with the regions shown in Figure 6. Heat was applied to the NiCr ring inside the rod. The housing was modeled using an unheated slab geometry with a thickness of 6.5 mm. Both radial and azimuthal thermal conduction are enabled in the pin model.

The noncondensable gas model was disabled because there is no impact of noncondensable gas in these experiments. The droplet entrainment model is enabled. The tabular form of the IAPWS97 fluid properties is used. The turbulent mixing model was enabled for the pin-resolved model (this model will have no effect for the lumped one, which has no lateral connections). The void-drift was disabled, and the single-phase turbulent mixing parameter was set to 0.037 with the Beus two-phase mixing multiplier set to 5.0. The turbulent mixing value is the default value used for all VERA simulations, which was originally obtained by tuning CTF to STAR-CCM+ results for PWR rod bundle geometry (Gordon, 2017). The Beus value is the default value, which was recommended by Sato (Sato, 1992). Boundary conditions included inlet mass flow rate and enthalpy and outlet pressure. A timestep refinement study was performed to determine the impact of maximum timestep size. One important caveat is that the fine-mesh renodalization feature was not enabled because the model has known issues that must be resolved prior to its use. This feature was designed for use in LOCA reflood cases and works to re-mesh the rod axial mesh in the region of the quench front. This allows for better resolution of the quench front. The Groeneveld lookup tables are used for the CHF model and the Chen model is used for subcooled and saturated boiling.

Operating conditions for the FEBA 229 case are shown in Figure 9, which is reproduced from the FEBA data report (Ihle & Rust, FEBA---Flooding Experiments with Blocked Arrays Data Report 1, Test Series I through IV, 1984). This plot was digitized to obtain forcing functions for total bundle power, inlet mass flow rate, and inlet temperature. The outlet pressure was quite steady, so no forcing function was obtained for this boundary condition. These forcing functions were applied in the CTF model. The inlet enthalpy in the CTF model was adjusted so that the inlet temperature matched the experimental inlet temperature.

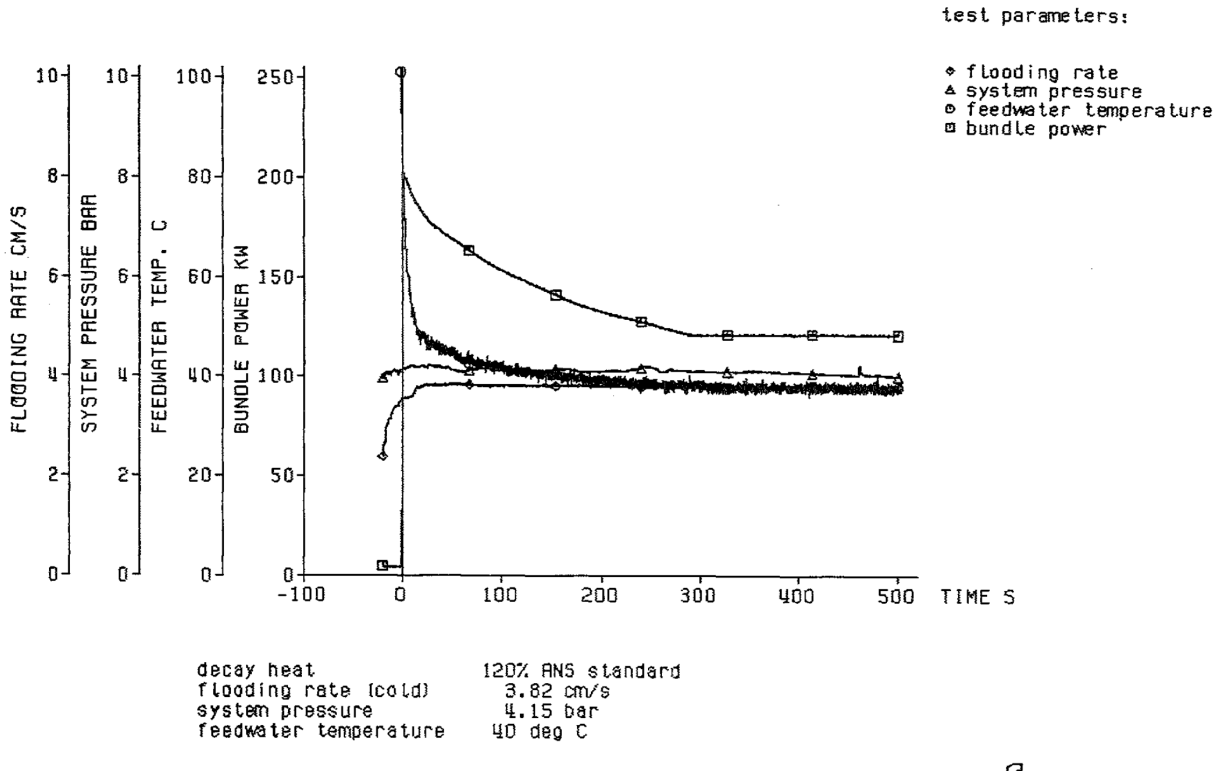

Figure 9. Case 229 transient boundary condition behavior.

The initial temperature distribution of the pins was also provided in Figure 10, which is reproduced from the FEBA documentation (Ihle & Rust, FEBA---Flooding Experiments with Blocked Arrays Data Report 1, Test Series I through IV, 1984). This plot was digitized to obtain the axial temperature table for the pins.

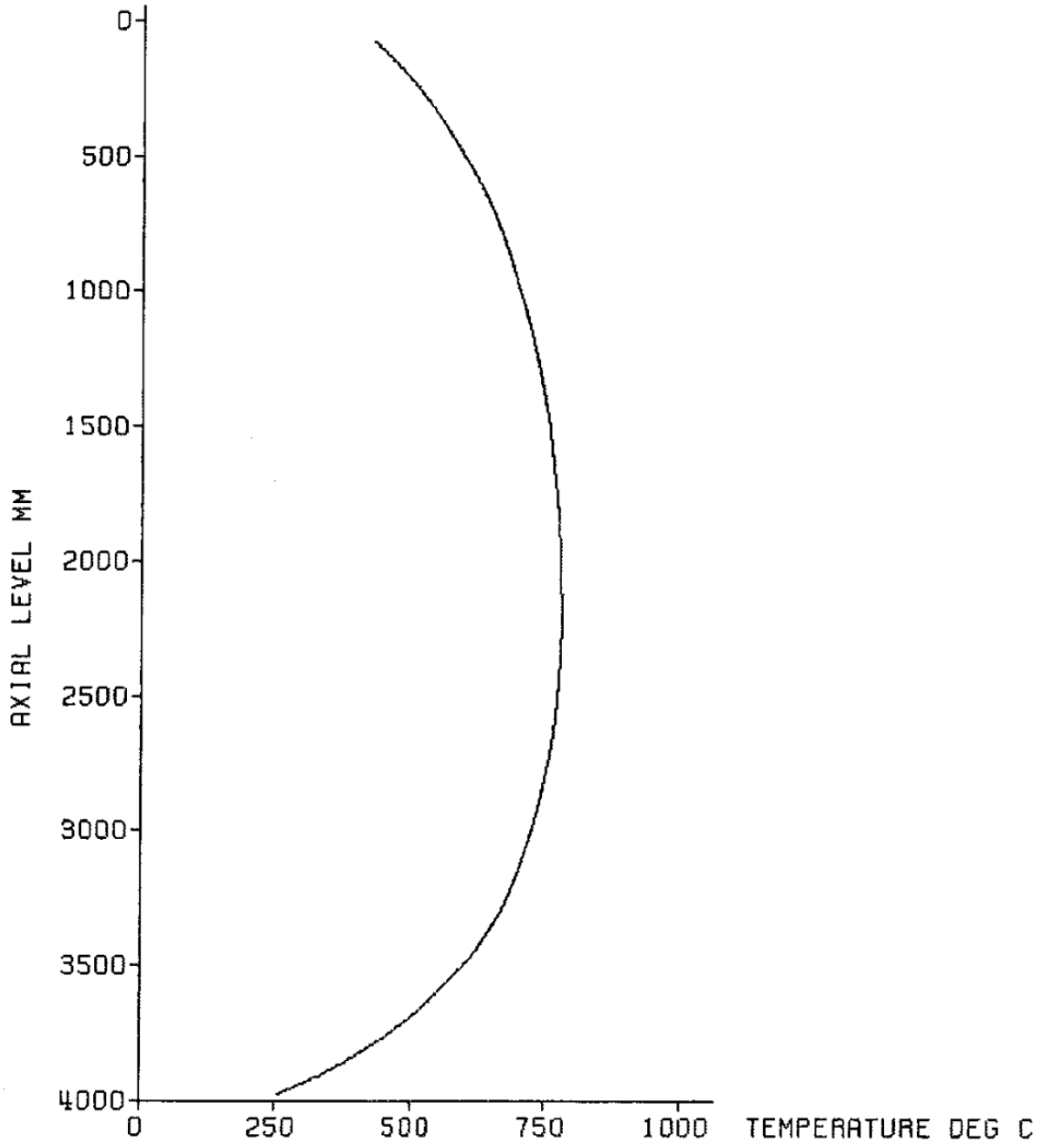

Figure *10*. Initial temperature distribution in the Case 229 pins.

The initial temperature distribution in the experimental housing was not provided in the FEBA documentation; however, the housing inside surface temperature was measured by the authors. To estimate the initial housing temperature, the shape of the pin initial temperature was scaled so that the initial measured value matched the initial temperature profile at that axial location. The resulting initial temperature distribution for the housing is shown in **Table** 5.

Table 5. Initial axial temperature profile in the experimental housing for Case 229

Axial location [mm]	Temperature [C]
0	258
145	258
187	305
270	375
353	431
452	486
552	533
651	573
783	611
903	638
1,077	664
1,262	690
1,461	706
1,642	719
1,840	721
2,042	724
2,191	722
2,347	715
2,566	710
2,751	696
2,974	676
3,250	641
3,381	621
3,538	591
3,706	548
3,813	513
3,912	478
3,969	452
4,035	427
4,196	427

The initial void in the facility is set to 100%. The initial mass flow rate is set to 0.0 kg/s. The initial enthalpy is set to 2750 kJ/kg to ensure a superheated vapor.

3.2.2 TRACE Model

The TRACE code is intended for TH modeling on an assembly scale or coarser, and the code is not intended for subchannel-scale modeling like CTF. Therefore, only a coarse-mesh model was created in TRACE for direct comparison to the coarse-mesh CTF model.

The TRACE model was built to be as consistent with the CTF model as possible. Because of this, the same fluid axial mesh and spacer grid locations and form losses were used. A single 1D flow channel was modeled for the entire FEBA assembly, with the same flow area and hydraulic diameter as used in the CTF coarse-mesh model. The same transient forcing functions were used for boundary conditions and bundle power, and initial conditions were also matched.

One important difference is that the fine mesh renodalization capability was used in the TRACE analyses, whereas this feature was not used in the CTF analyses. Fine mesh renodalization is a feature which subdivides the fuel rod axial nodes into finer nodes for the primary purpose of more accurately tracking the quench front propagation during LOCA events. The finer nodalization helps in resolving the sharp temperature gradients in the vicinity of the quench front as the front moves upwards along the fuel rod. In TRACE, this renodalization is achieved by first subdividing each coarse axial node into multiple permanent fine mesh nodes (by default, there are three permanent fine mesh nodes per coarse node). These nodes are then automatically subdivided further in the presence of large temperature gradients and are recombined when the gradients are smaller (e.g., after the quench front has passed).

The TRACE manual recommends using the fine mesh renodalization feature in all LOCA calculations, which was the rationale for enabling it in the TRACE model. The goal of using TRACE in this study was to provide the most accurate LOCA results possible, consistent with best practices and intended code usage for this application. This is why the fine mesh renodalization feature was employed in TRACE, even though CTF did not use this feature (because of known issues which would need to be addressed in this model prior to its use).

3.3 Parameter Sensitivity Study

3.3.1 CTF Evaluation

3.3.1.1 Sensitivity Study

CTF includes many models for LOCA analysis that needed to be assessed prior to being used for validation or benchmarking with TRACE. To make this process as efficient as possible, the models with the most significant impact on prediction of peak clad temperature and quench time were determined. A sensitivity analysis was developed using the FEBA lumped model of Case 229. The lumped model was used instead of the pin-resolved model because thousands of simulations are required to complete the sensitivity analysis, which requires a fast-running model. This means the crossflow models cannot be assessed during this analysis.

The focus of this sensitivity analysis was to test as many of the models as possible that were shown in **Figure** 1. To accomplish this, the CTF model multiplier feature, which allows a user to supply multipliers for specific models in CTF via input, was expanded to cover all relevant closure models for LOCA reflood applications. Ultimately, 44 model multipliers were tested during the sensitivity analysis. A high-level summary of the multipliers is shown in **Table** 6. This table shows the number of model multipliers tested in each major category of LOCA models, as well as their range of values. The range of the multipliers were set so that the effect of each model is cut in half or doubled in the most extreme cases.

The range of the heat transfer model multipliers was smaller because it is assumed that the uncertainty of these models will be less than the others. A full list of the multipliers is given in **Table** 7.

Table 6. Summary of multipliers tested in sensitivity analysis

Multiplier group	Multiplier range	Number of multipliers
Interfacial drag	0.5—2.0	8
Entrainment	0.5—2.0	7
Interfacial area	0.5—2.0	11
Interfacial heat transfer	0.5—2.0	8
Rod heat transfer	0.8—1.2	10

The only models that were not tested as part of this sensitivity analysis are ones related to spacer grid quenching, which includes heat transfer between the spacer grid and vapor or droplets, grid film growth and heat transfer to the vapor. The grid heat transfer enhancement and spacer grid droplet breakup models were enabled.

Table 7. Summary of perturbation parameters used in the CTF LOCA reflood sensitivity analysis

Multiplier name	Description
K_xk_sb	Multiplier on the interfacial drag between vapor and liquid in the small bubble flow regime
K_xk_slg	Multiplier on the interfacial drag between vapor and liquid in the slug flow regime
K_xk_anrflm	Multiplier on the interfacial drag between vapor and liquid film in the annular-mist flow regime
K_xk_anrdrp	Multiplier on the interfacial drag between vapor and liquid droplets in the annular-mist flow regime
K_xk_dispersed	Multiplier on the interfacial drag between vapor and droplets in the post-CHF dispersed flow regime
K_xk_bottom_reflood	Multiplier on the interfacial drag between vapor and liquid in the post-CHF bottom reflood flow regime
K_xk_top_reflood	Multiplier on the interfacial drag between vapor and liquid in the post-CHF top reflood flow regime
K_xk_deluge	Multiplier on the interfacial drag between vapor and liquid in the post-CHF deluge flow regime
K_entrainment_quench_front	Multiplier on the entrainment rate caused by quenching
K_entrainment_sputtering	Multiplier on the entrainment rate caused by sputtering caused by quenching of the falling film
K_entrainment_falling_film	Multiplier on the entrainment rate caused by breakup of large pools of liquid in a falling film
K_entrainment_annular	Multiplier on the entrainment rate from the film in the annular-mist flow regime
K_deentrainment_hot_film	Multiplier on the de-entrainment rate into films above in post-CHF flow regimes
K_deentrainment_into_bubbly	Multiplier on the de-entrainment rate into high-liquid content flow regimes
K_deentrainment_annular	Multiplier on the de-entrainment rate into the liquid film in the annular-mist flow regime
K_drop_diam_dispersed	Multiplier on the droplet diameter in the post-CHF dispersed droplet flow regime (diameter calculated from Sauter-mean calculation)

K_drop_diam_dsaut	Multiplier on the droplet diameter calculated in the post-CHF dispersed droplet flow regime (note that this droplet diameter and the previous one are used for different calculations in CTF)
K_drop_diam_annular	Multiplier on the droplet diameter calculation in the annular-mist flow regime
K_int_ht_scv_liq	Multiplier on the interfacial heat transfer coefficient between continuous liquid and vapor when vapor is subcooled
K_int_ht_scv_drp	Multiplier on the interfacial heat transfer coefficient between droplets and vapor when vapor is subcooled
K_int_ht_scl_liq	Multiplier on the interfacial heat transfer coefficient between continuous liquid and vapor when liquid is subcooled
K_int_ht_scl_drp	Multiplier on the interfacial heat transfer coefficient between droplets and vapor when liquid is subcooled
K_int_ht_shl_liq	Multiplier on the interfacial heat transfer coefficient between continuous liquid and vapor when liquid is superheated
K_int_ht_shl_drp	Multiplier on the interfacial heat transfer coefficient between droplets and vapor when liquid is superheated
K_int_ht_shv_liq	Multiplier on the interfacial heat transfer coefficient between continuous liquid and vapor when vapor is superheated
K_int_ht_shv_drp	Multiplier on the interfacial heat transfer coefficient between droplets and vapor when vapor is superheated
K_int_area_sb	Multiplier on the interfacial area between liquid and vapor in the small bubble flow regime
K_int_area_slug	Multiplier on the interfacial area between liquid and vapor in the slug flow regime
K_int_area_annular_film	Multiplier on the interfacial area between the liquid film and vapor in the annular-mist flow regime
K_int_area_annular_drop	Multiplier on the interfacial area between the droplets and vapor in the annular-mist flow regime
K_int_area_dispersed	Multiplier on the interfacial area between the droplets and vapor in the post-CHF dispersed droplet flow regime
K_int_area_bottom_reflood	Multiplier on the interfacial area between continuous liquid and vapor in the post-CHF bottom-reflood flow regime
K_int_area_top_reflood	Multiplier on the interfacial area between continuous liquid and vapor in the post-CHF top-reflood flow regime
K_int_area_deluge	Multiplier on the interfacial area between continuous liquid and vapor in the post-CHF deluge flow regime
K_qchf	Multiplier on the critical heat flux
Ka_T_min_film_boiling	Adder on the minimum film boiling temperature (ranged between +/- 50 F)
K_ht_vapor_convection	Multiplier on the vapor convective heat transfer coefficient
K_grid_ht_enhancement	Multiplier on the grid-spacer heat transfer enhancement effect
K_ht_droplet_enhancement	Multiplier on the droplet heat transfer enhancement effect
K_ht_drop_deposition	Multiplier on the droplet deposition heat transfer effect
K_ht_hotwall_radiative	Multiplier on the radiative heat transfer effect between pin and film/droplets/vapor in post-CHF heat transfer regimes
K_ht_iafb	Multiplier on the inverted annular film boiling heat transfer coefficient
K_bjornard_f_factor	Multiplier on the F-factor calculated by the Bjornard-Griffith model, which is used to determine the split between CHF and minimum film boiling (MFB) heat transfer for the transition boiling heat transfer regime
K_hnb	Multiplier on the subcooled/saturated nucleate boiling heat transfer coefficient

The four output parameters that would be observed included: total bundle pressure drop, peak cladding temperature at the 19g2 thermocouple location, quench time at the 19g2 thermocouple location (defined as the time when temperature drops below 200 C), and droplet carryover at the bundle exit. Dakota (Dalbey, 2022) was used to drive the sensitivity analysis. A Latin hypercube sampling method was used to generate the combinations of input parameters. Three studies were performed using 5,000, 10,000, and 25,000 samples. It was found that results of the sensitivity analysis did not change significantly between the 10,000 and 25,000 sample cases, indicating that the analysis is suitably converged after 10,000 simulations. Moving from 10,000 to 25,000 samples did not change the ordering of the most important parameters.

For the 10,000-simulation case, only 2 CTF cases failed to converge. Dakota was used to generate the rank correlation coefficients for the four output datasets compared to the 44 model inputs. **Figure** 11— through **Figure** 14 show the partial rank correlation coefficient generated by Dakota between each input and output parameter of interest.

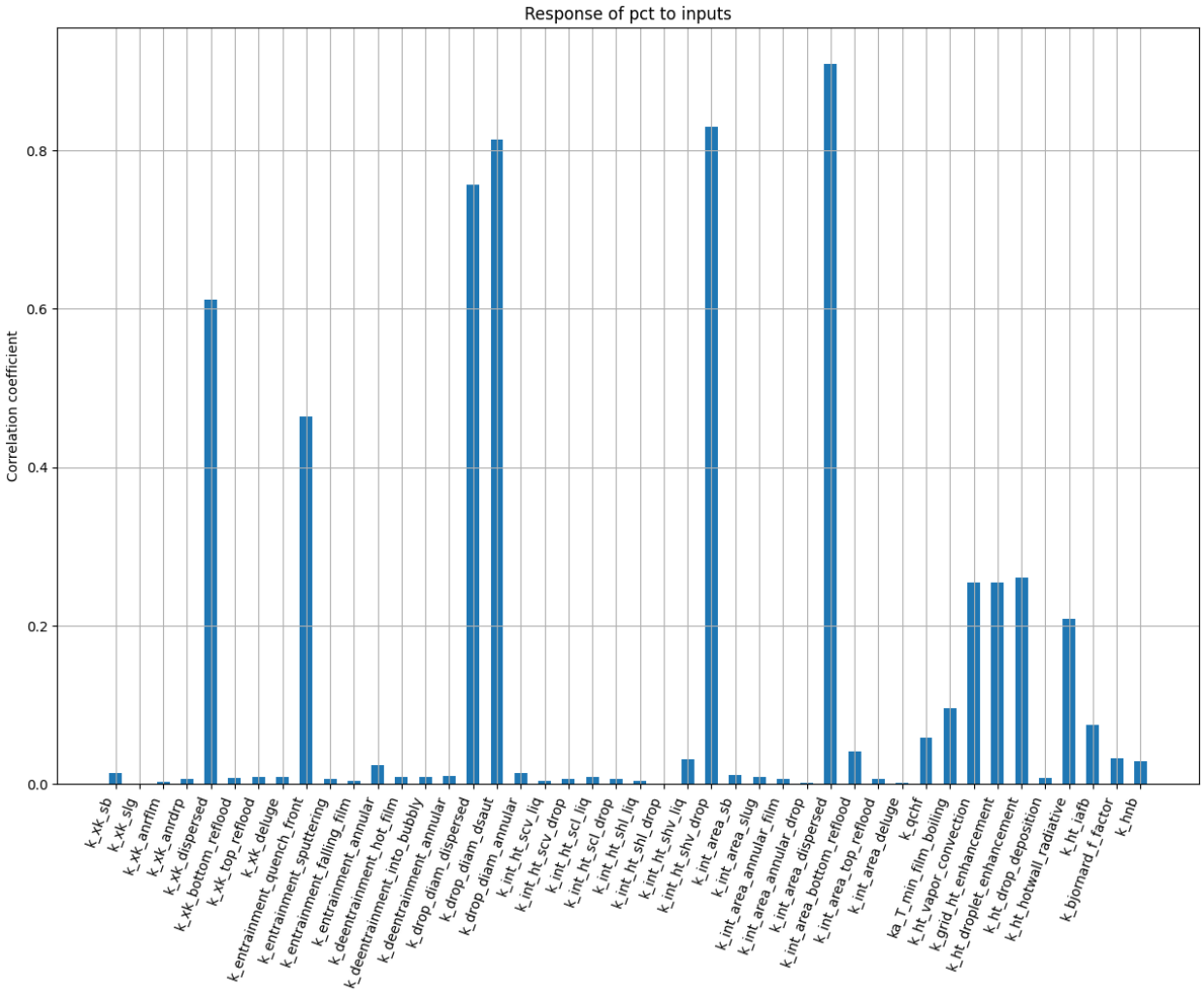

Figure *11*. Rank correlation coefficients for peak cladding temperature.

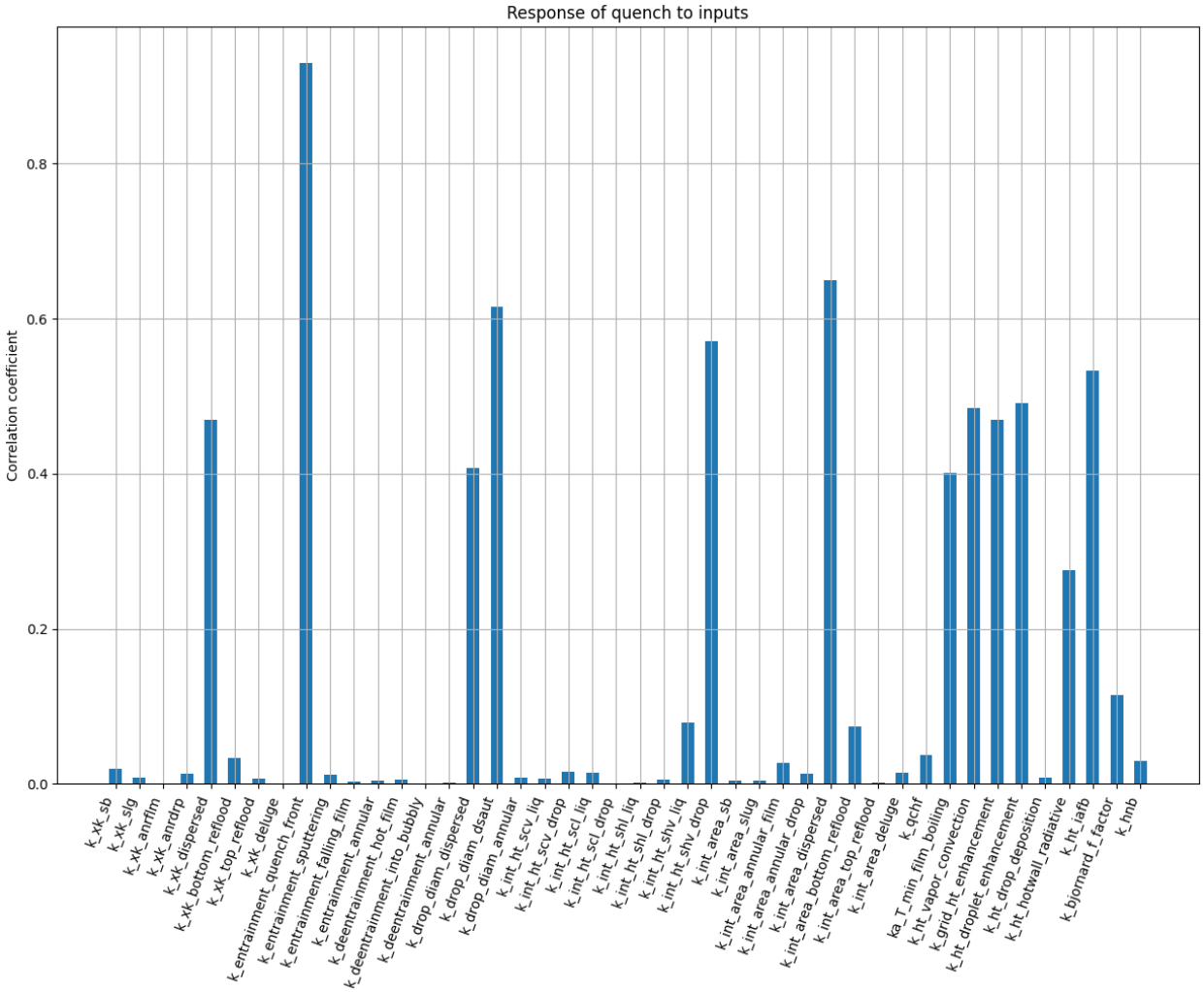

Figure *12*. Rank correlation coefficients for quench time.

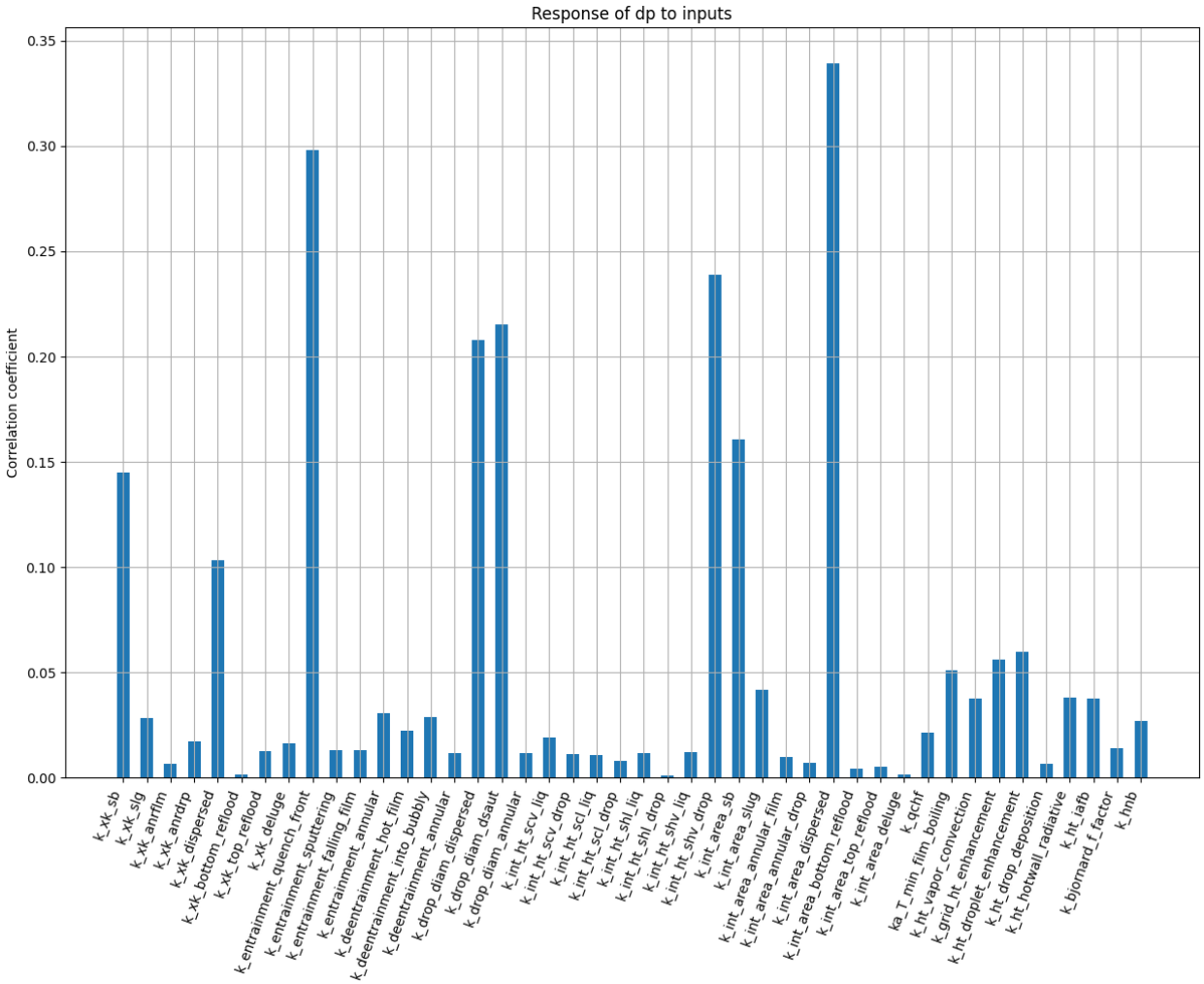

Figure *13*. Rank correlation coefficients for bundle pressure drop.

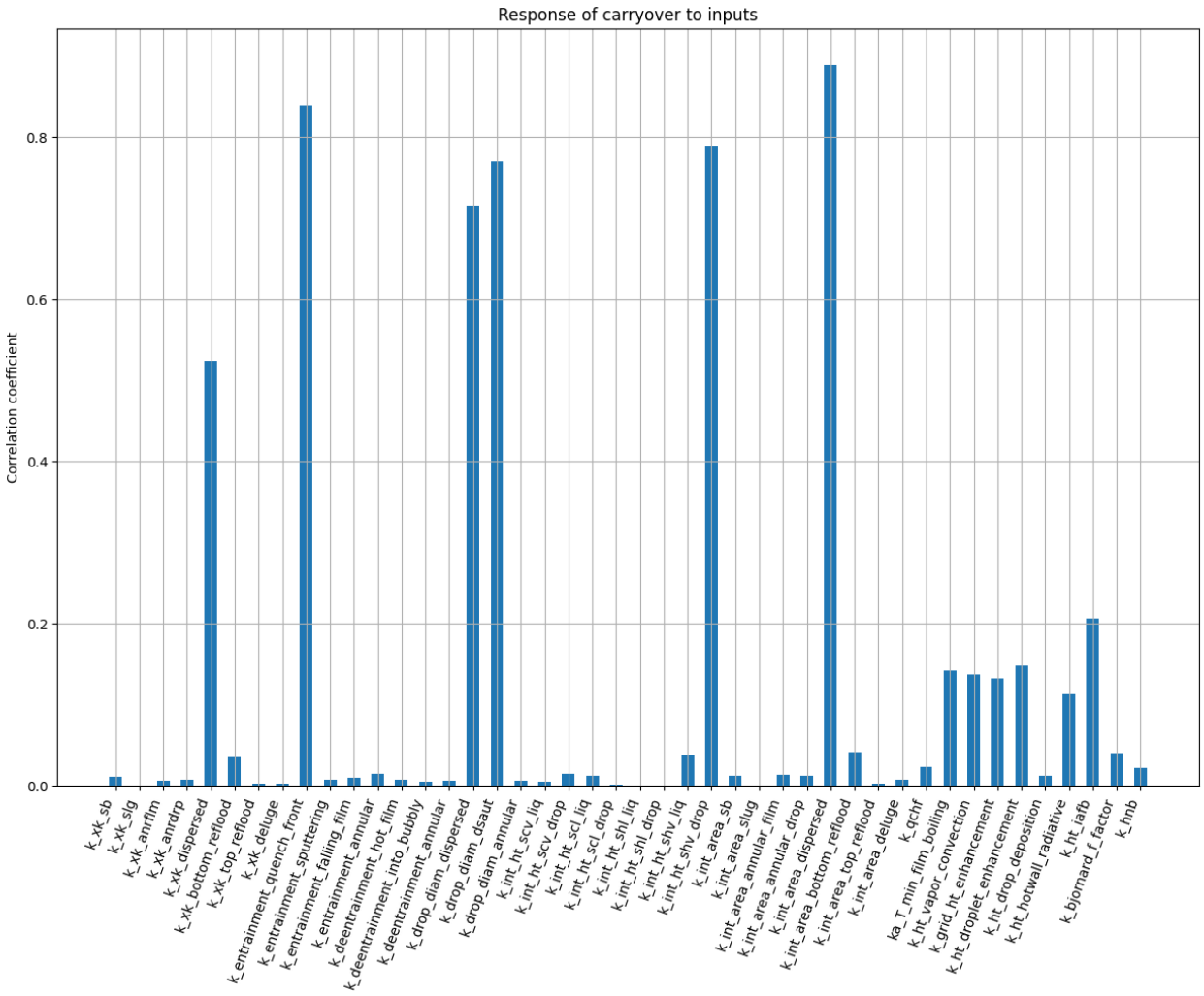

Figure *14*. Rank correlation coefficients for droplet carryover.

A summary of the input parameters with the five most significant rank correlation coefficient (RCC) values are shown in **Table** 8. The parameters are ranked from most significant (closest to 1 or -1) to least significant. These results show the importance of the droplet behavior in LOCA reflood cases. The entrainment rate, interfacial drag, interfacial heat transfer, interfacial area, and diameter of the droplets comprise almost this entire list. Even the wall heat transfer effects show up lower in the list when they show up at all. It is also noted that the pressure drop is weakly correlated to all selected inputs, with the highest RCC less than 0.4.

Table *8*. Ordering of RCC values from most significant to least significant for each figure of merit (top 5 shown)

	PCT	Quench time	Pressure drop	Carryover
1	K_int_area_dispersed	K_entrainment_quench_front	K_int_area_dispersed	K_int_area_dispersed
2	K_int_ht_shv_drop	K_int_area_dispersed	K_entrainment_quench_front	K_entrainment_quench_front
3	K_drop_diam_dsaut	K_drop_diam_dsaut	K_int_ht_shv_drop	K_int_ht_shv_drop

4	K_drop_diam_dispersed	K_int_ht_shv_drop	K_drop_diam_dsaut	K_drop_diam_dsaut
5	K_xk_dispersed	K_ht_iafb	K_drop_diam_dispersed	K_drop_diam_dispersed

3.3.1.2 Model Improvements

The results of the sensitivity analysis are discussed in Section 3.3.1.1 and are used to guide efforts in reviewing the CTF LOCA models. Several issues or areas for potential improvement were discovered in CTF during the assessment of LOCA models. All issues were documented in detail on the ORNL VERA Gitlab site. All changes made to CTF during this project were reviewed and merged into the development version of the code that is managed according to the VERA software quality assurance plan. Changes will be available in a future release of CTF. A summary of the changes made as part of this work are shown in **Table** 9. In addition to the corrections and improvements summarized in the table, work continues to investigate making several equation source terms more implicit (entrainment, turbulent mixing, interfacial shear, and wall shear) to further improve the numerical stability and allow CTF to take larger timesteps.

Table *9*. Summary of CTF changes required for modeling of LOCA reflood

Gitlab ticket number	Gitlab ticket number
5205	The transition boiling model was corrected so that heat transfer is interpolated between minimum film boiling and critical heat flux points of the boiling curve, which is consistent with the Bjornard and Griffith model.
5206	Quenching behavior was corrected so that CTF continues to use hot-wall closure models until surface temperature are within 10 F of the saturation temperature, rather than switching to pre-CHF models immediately upon temperature dropping below the CHF value.
5207	Remove the 1.5 multiplier on the Kataoka, Ishii, and Mishima model for quench front entrainment.
5208	Correct the Weber-based correlation for calculation of droplet diameter in the dispersed flow regime so that it is consistent with COBRA-TRAC.
5209	Fix errors in the implementation of the droplet-induced turbulence heat transfer enhancement model.
5210	Fix errors in the implementation of the Forslund-Rohsenow model, which is used for calculation of interfacial heat transfer between vapor and droplets in the dispersed droplet flow regime.
5219	Fix errors in the identification of the falling film flow regime and the flow regime ID that is written to the CTF output file.
5261	Fix calculation of the CHF temperature when using the Gorenflo boiling heat transfer model
5224	Make fluid property limits used for numerical controls more consistent with fluid property table boundaries for improved numerical stability for post-CHF conditions.
5228	Enable mass and momentum mixing in the droplet field.
2086	Make improvements to the numerical controls, including detection of the solution going out of fluid property bounds and optimizing numerical controls for LOCA conditions.
5226	Fix the construction of mass and energy equation residuals by including the inertial term, which is important when the outer iteration loop is enabled.
5204	Add new edits to the CTF output file important for LOCA analysis.

3.3.2 TRACE Evaluation

A sensitivity analysis was performed on the TRACE FEBA model, which similar to the sensitivity analysis performed for the CTF model. A total of 43 physical modeling parameters can be exposed as "UQ variables" in the TRACE input deck. The parameters and their descriptions are given in **Table** 10. Sensitivity coefficients were applied as multipliers on each of these parameters which were uniformly distributed across the ranges specified in **Table *11***. Note that these ranges are consistent with those used in the CTF sensitivity analysis, including separate ranges for quantities related only to the fluid and quantities related to rod heat transfer.

Table *10*. Summary of perturbation parameters used in the TRACE LOCA reflood sensitivity analysis

Multiplier name	Description
bubSlugLiqIntHTC	Liquid to interface bubbly slug heat transfer. Applies to hydraulic components only.
annMistLiqIntHTC	Liquid to interface annular-mist heat transfer coefficient. Applies to hydraulic components only.
transLiqIntHTC	Liquid to interface transition heat transfer coefficient. Applies to hydraulic components only.
stratLiqIntHTC	Liquid to interface stratified heat transfer coefficient. Applies to hydraulic components only.
bubSlugVapIntHTC	Vapor to interface bubbly slug heat transfer coefficient. Applies to hydraulic components only.
annMistVapIntHTC	Vapor to interface annular-mist heat transfer coefficient. Applies to hydraulic components only.
transVapIntHTC	Vapor to interface transition heat transfer coefficient. Applies to hydraulic components only.
stratVapIntHTC	Vapor to interface stratified heat transfer coefficient. Applies to hydraulic components only.
singlePhaseLiqWallHTC	Single phase liquid to wall heat transfer coefficient. Applies to heat structure components only.
singlePhaseVapWallHTC	Single phase vapor to wall heat transfer coefficient. Applies to heat structure components only.
filmTransBoilTMin	Film to transition boiling Tmin criterion temperature. Applies to heat structure components only.
dispFlowFilmBoilHTC	Dispersed flow film boiling heat transfer coefficient. Applies to heat structure components only.
subBoilHTC	Subcooled boiling heat transfer coefficient. Applies to heat structure components only.
nucBoilHTC	Nucleate boiling heat transfer coefficient. Applies to heat structure components only.
DNB_CHF	Departure from nucleate boiling / critical heat flux. Applies to heat structure components only.
transBoilHTC	Transition boiling heat transfer coefficient. Applies to heat structure components only.
gapConductance	Gap conductance coefficient. Applies to heat structure components only.
fuelThermalCond	Fuel thermal conductivity. Applies to heat structure components only.
cladMWRX	Cladding metal-water reaction rate coefficient. Applies to heat structure components only.
fuelRodIntPress	Rod internal pressure coefficient. Applies to heat structure components only.
burstTemp	Burst temperature coefficient. Applies to heat structure components only.
burstStrain	Burst strain coefficient. Applies to heat structure components only.
wallDrag	Wall drag coefficient. Applies to hydraulic components only.

formLoss	Form loss coefficient. Applies to hydraulic components only.
bubblyIntDrag	Interfacial drag (bubbly) coefficient. Applies to hydraulic components only.
dropletIntDrag	Interfacial drag (droplet) coefficient. Applies to hydraulic components only.
bubSlugIntDragBundle	Interfacial drag (bubbly/slug Rod Bundle - Bestion) coefficient. Applies to hydraulic components only.
bubSlugIntDragVessel	Interfacial drag (bubbly/slug Vessel) coefficient. Applies to hydraulic components only.
annMistIntDragVessel	Interfacial drag (annular/mist Vessel) coefficient. Applies to hydraulic components only.
dffbIntDrag	Interfacial drag (dispersed flow film boiling) coefficient. Applies to hydraulic components only.
invSlugIntDrag	Interfacial drag (inverted slug flow) coefficient. Applies to hydraulic components only.
invAnnIntDrag	Interfacial drag (inverted annular flow) coefficient. Applies to hydraulic components only.
cladThermCnd	Cladding thermal conductivity coefficient. Applies to heat structure components only.
cladSpecHeat	Cladding specific heat coefficient. Applies to heat structure components only.
invAnnVapWallHTC	Vapor to wall inverted annular heat transfer coefficient. Applies to heat structure components only.
invAnnLiqWallHTC	Liquid to wall inverted annular heat transfer coefficient. Applies to heat structure components only.
fuelSpecHeat	Fuel specific heat coefficient. Applies to heat structure components only.
criticalQualBiasi	Critical Quality (Biasi) Applies to heat structure components only.
criticalQualCiseGE	Critical Quality (CiseGE) Applies to heat structure components only.
subcooledNusseltSZ	Sub-cooled Boiling Nusselt Number (Saha-Zuber correlation). Applies to heat structure components only.
subcooledStatonSZ	Sub-cooled Boiling Stanton Number (Saha-Zuber correlation). Applies to heat structure components only.
bubSlugLiqIntHTC	Liquid to interface bubbly slug heat transfer. Applies to hydraulic components only.
annMistLiqIntHTC	Liquid to interface annular-mist heat transfer coefficient. Applies to hydraulic components only.

Table 11: Summary of multipliers tested in the TRACE sensitivity analysis

Multiplier group	Multiplier range	Number of multipliers
Fluid quantities	0.5—2.0	20
Rod heat transfer	0.8—1.2	23

Only the PCT figure of merit was employed for this TRACE study. Different sample sizes were attempted, including 90, 459, 1,000, and 2,000 samples. The rank coefficient results appeared to be reasonably well converged at 1,000 samples and especially at 2,000 samples. For example, the top five highest ranked parameters did not change between 459 and 2,000 samples, even if the rank coefficient values changed slightly. Therefore, 2,000 samples were considered sufficient for the purposes of identifying the most important parameters.

Figure 15 shows the rank correlation coefficient results for the 459-sample case, with the most highly ranked parameters listed in **Table** 12. The dispersed flow film boiling interfacial drag, dispersed flow film boiling heat transfer coefficient, and single-phase vapor wall heat transfer parameters were the three most

important parameters affecting the PCT. The first two parameters impact the relative velocity between the liquid and vapor phases and the wall to fluid heat transfer, respectively, in the dispersed flow film boiling regime. The single-phase vapor heat transfer parameter is relevant for very high void fraction conditions beyond that of the dispersed flow film boiling regime, which can also occur during LOCA.

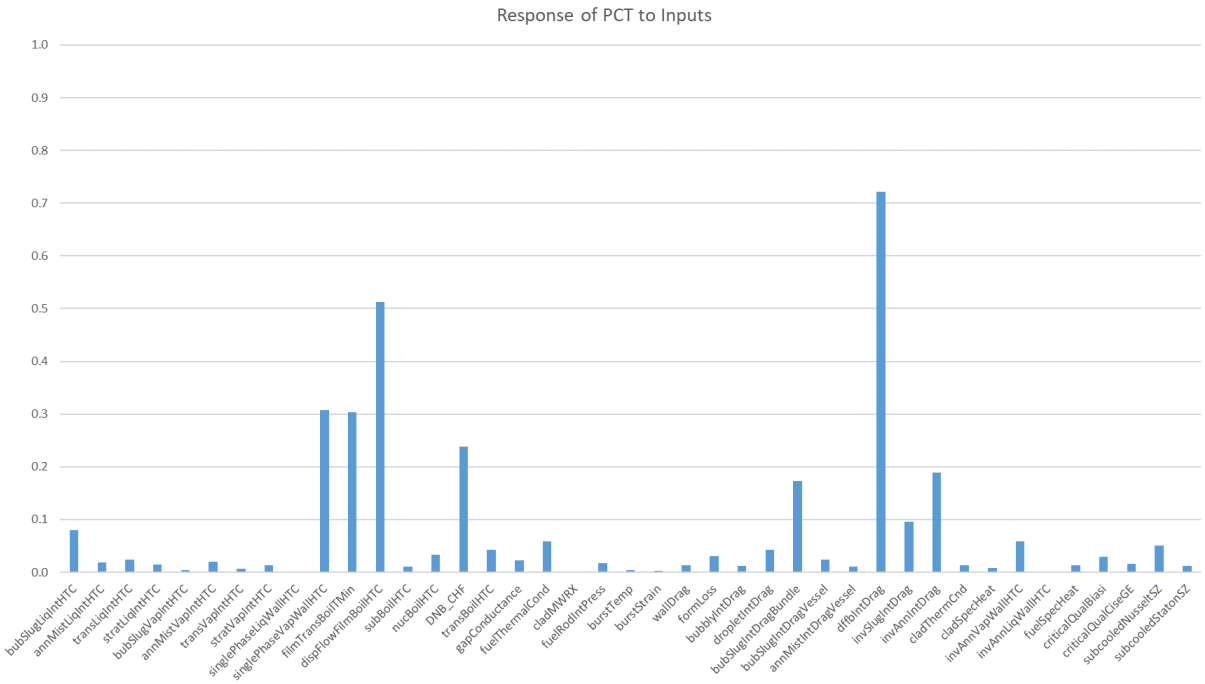

Figure *15*. Rank correlation coefficients for TRACE peak cladding temperature.

Table *12*. Order of TRACE RCC values from most significant to least significant for PCT (top 5 shown)

	Parameter	Rank correlation coefficient
1	dffbIntDrag	0.721
2	dispFlowFilmBoilHTC	0.513
3	singlePhaseVapWallHTC	0.307
4	filmTransBoilTMin	0.303
5	DNB_CHF	0.239

This is a particularly useful finding because post-CHF flow and heat transfer can exist in either the inverted annular film boiling, dispersed flow film boiling, transition boiling, or single-phase vapor regimes; the high ranking of the dispersed flow film boiling parameters indicates that this regime dominates the post-CHF behavior, at least for the conditions analyzed in this FEBA case. An examination of heat transfer regimes during the event confirms that this regime is the most prevalent, with transition and inverted annular film boiling regimes occurring less frequently and typically over a shorter length span of the rod. It is possible that the importance of each regime could change under different inlet flow conditions, inlet temperature conditions, and so on, but at least for this realistic LOCA scenario, the dispersed flow film boiling models impact PCT the most.

The CHF parameter dictates the transition from pre- to post-CHF heat transfer. The minimum film boiling temperature (T_{min}) parameter impacts the ability of the rod surface to return from post-CHF to pre-CHF conditions, a phenomenon also known as *quenching*. Because the transition boiling heat transfer

coefficient is interpolated between the heat transfer coefficients at T_{CHF} and T_{min}, these parameters also impact the transition boiling behavior. Since the CHF is exceeded rapidly after the break due to core depressurization, and will be exceeded for any reasonable value of T_{CHF}, the T_{CHF} sensitivity does not significantly impact the blowdown temperature behavior. However, T_{CHF} plays an important role in impacting the transition boiling heat transfer coefficient and return to pre-CHF conditions during the reflood phase.

It is relevant to note that there are similarities in the high-ranked CTF and TRACE parameters. Particularly, both codes predict a high importance of dispersed flow film boiling (DFFB) flow and heat transfer parameters. Many of the other high-ranked CTF parameters pertain to the droplet and entrainment models. Although TRACE does not solve conservation equations for the droplet field like CTF does, droplet and entrainment phenomena are indirectly incorporated into the flow and heat transfer regimes in TRACE, and these phenomena are especially relevant to the dispersed flow film boiling regime.

Therefore, these TRACE sensitivity findings reinforce the CTF findings regarding the importance of dispersed flow film boiling and droplet/entrainment modeling, with respect to the prediction of PCT during LOCA.

Another interesting finding of the TRACE study is in the overall impact of the sensitivity parameters on the final PCT figure of merit. Among the 2,000 samples, the mean PCT was 1,263 K, with a standard deviation of 32 K. This 32 K standard deviation is relatively small given the large number of varied input parameters (43) and the relatively large sensitivity range applied to each of them (**Table *11***). However, the FEBA experiment represents a relatively idealized LOCA scenario with carefully controlled inlet flow, inlet temperature, and outlet pressure conditions, as well as a reduced-scale bundle geometry. The predicted PCT sensitivity in a more detailed full system LBLOCA model may be larger because of the added radial complexity and the impact of vessel and plant dynamics. This would be especially true if sensitivities on plant parameters (e.g., operating conditions, break assumptions, safety system assumptions) were also considered.

Differences in power conditions may impact parameter sensitivities as well. For example, consider the differences in the axial power shape for the FEBA and full-core high-burnup studies (Section 5) shown in **Figure** 16. The centrally peaked FEBA power shape would be expected to produce peak cladding temperatures only slightly above the axial center of the rods, whereas the peak cladding temperature in the high-burnup core analyses occurs near the top of the rods due to the double-peaked axial profile. This means that the quench front must travel farther in the full core case before the PCT is affected, perhaps changing the relative importance of various flow and temperature effects, and perhaps increasing the overall impact of these phenomena on the PCT.

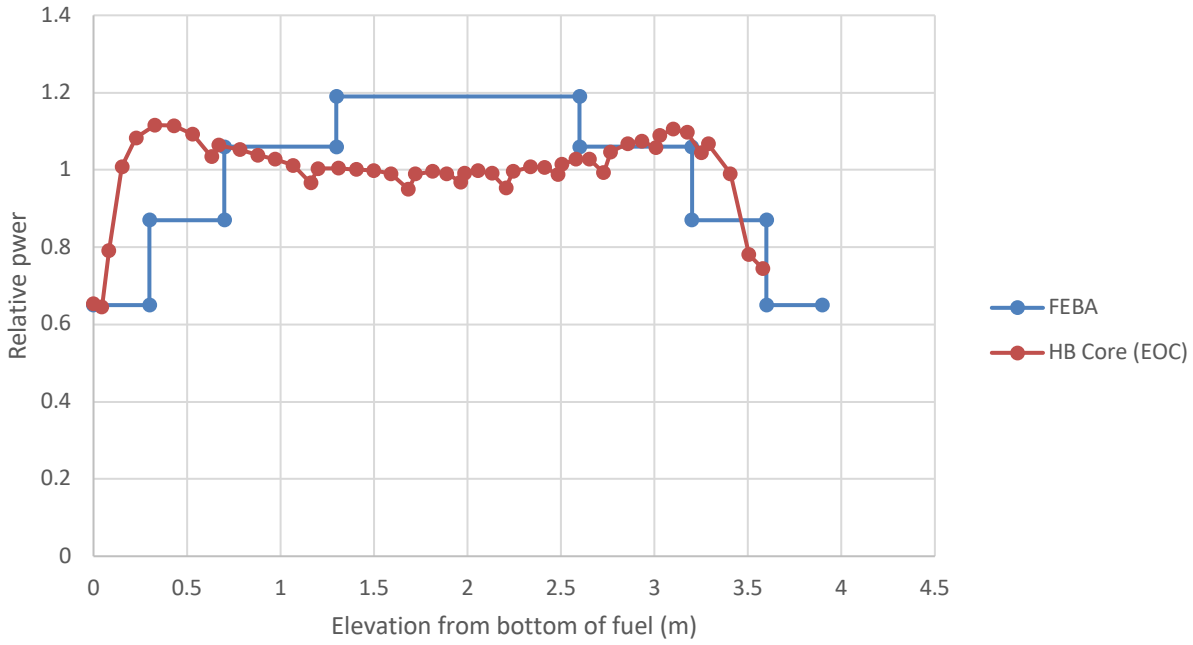

Figure *16*. Comparison of axial power shapes in the FEBA experiment and full core high burnup cycle study.

3.4 Validation and Code-to-Code Benchmark

3.4.1 CTF Timestep refinement study

CTF uses the material Courant-Friedrichs-Lewy (CFL) limit to limit the timestep size based on local fluid velocity. Other controls will also limit the timestep size based on the change of the solution between timesteps. A study was performed to investigate the impact of timestep size on the solution of transient pin cladding surface temperature at the 19g2 thermocouple location. Note that the CFL limit will always limit the timestep size based on local velocity, but the user can set a more restrictive limit via the input file. The maximum allowable timestep size was varied between 1e-2, 1e-3, and 1e-4 s for the lumped model of FEBA Case 229. The transient temperature behavior is shown in **Figure** 17 for all three timestep sizes. Note that the resulting timestep sizes for each simulation were checked to ensure that the smaller timestep sizes were getting smaller as opposed to all three cases being limited by the CFL limit. **Figure** 18 shows the same study for the pin-resolved case. The lumped model is well-converged for any of the chosen timestep sizes, but the resolved case continues to experience changes in the solution when moving from 1e-3 to 1e-4 s.

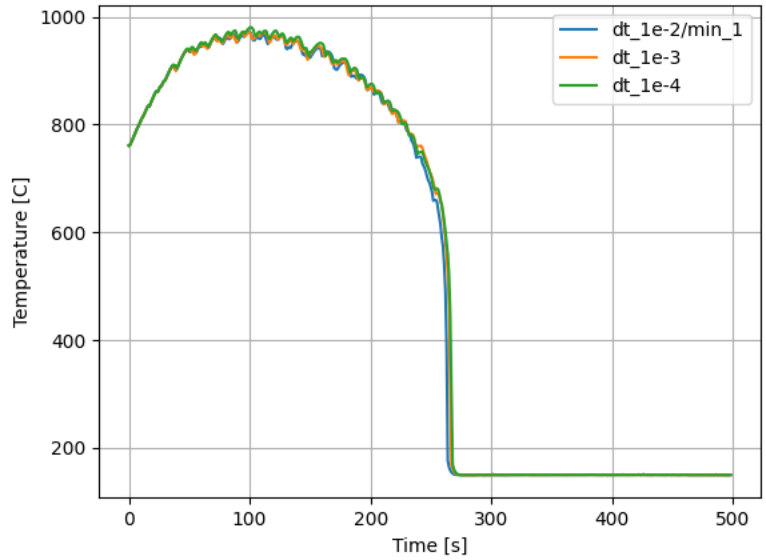

Figure *17*. **Impact of timestep size on the solution of pin temperature in the lumped CTF model.**

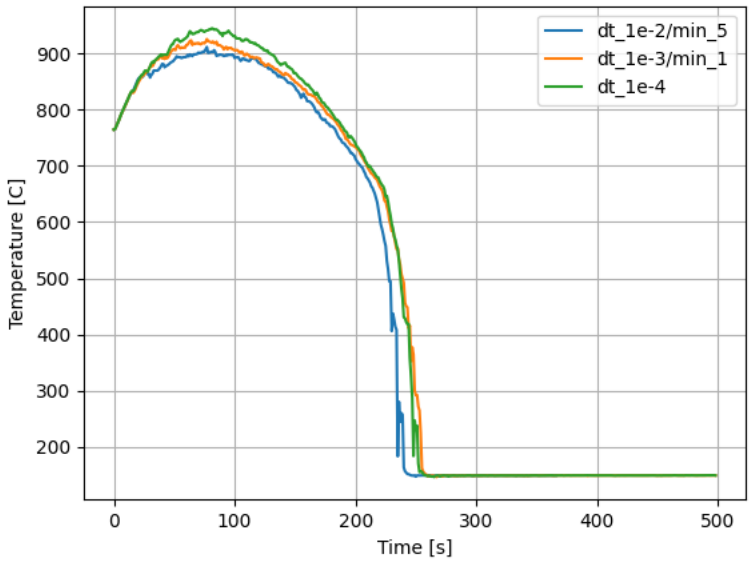

Figure *18*. **Impact of timestep size on the solution of pin temperature in the pin-resolved CTF model.**

3.4.2 Benchmark and Validation Results

The transient temperature solution results are compared to the experimental data at all thermocouple locations presented in **Table** 1. Results are shown moving from the bottom of the bundle to the top in **Figure** 19 through **Figure** 30. Each figure shows the experimental result, the TRACE prediction, and the CTF prediction using both lumped and resolved models. The CTF lumped model uses a 1e-2 maximum

timestep size, but the resolved model uses a 1e-4 s maximum timestep size based on results of the timestep refinement study.

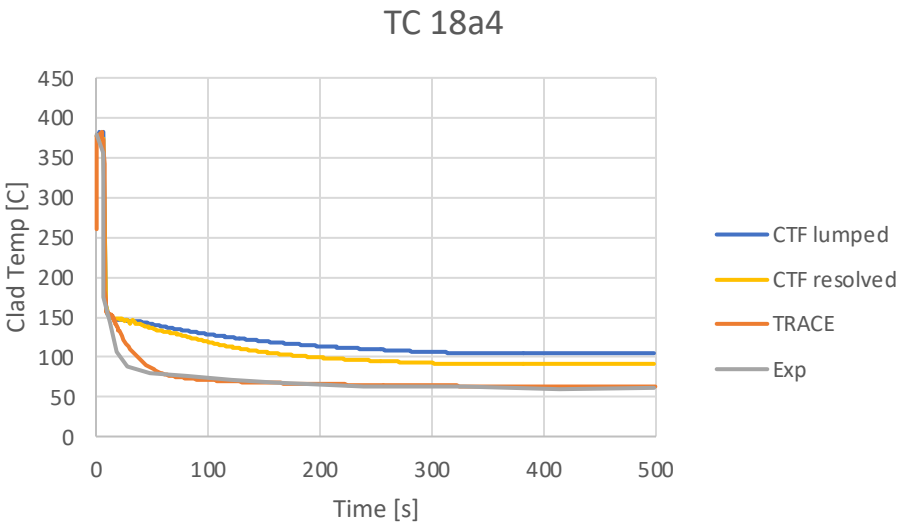

Figure *19*. Comparison of predicted and measured clad temperature at 18a4 (254 mm) location.

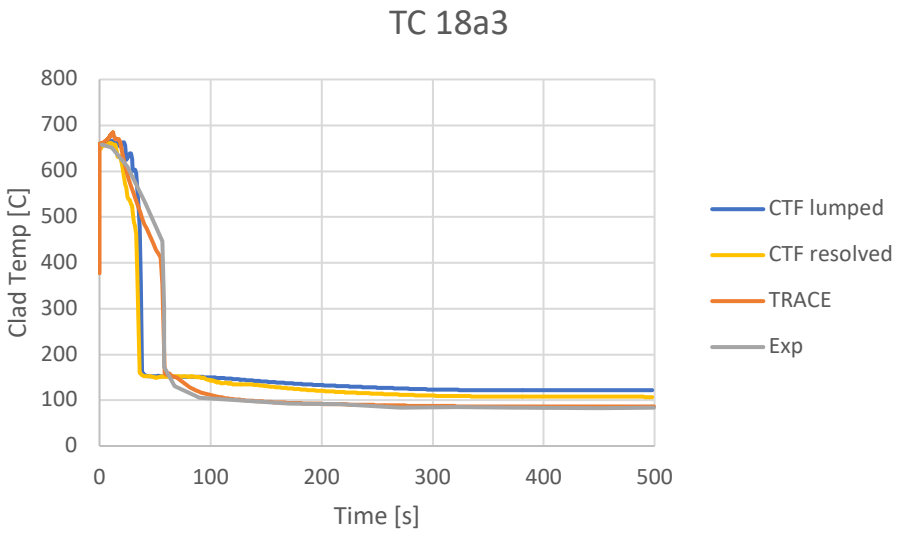

Figure *20*. Comparison of predicted and measured clad temperature at 18a3 (799 mm) location.

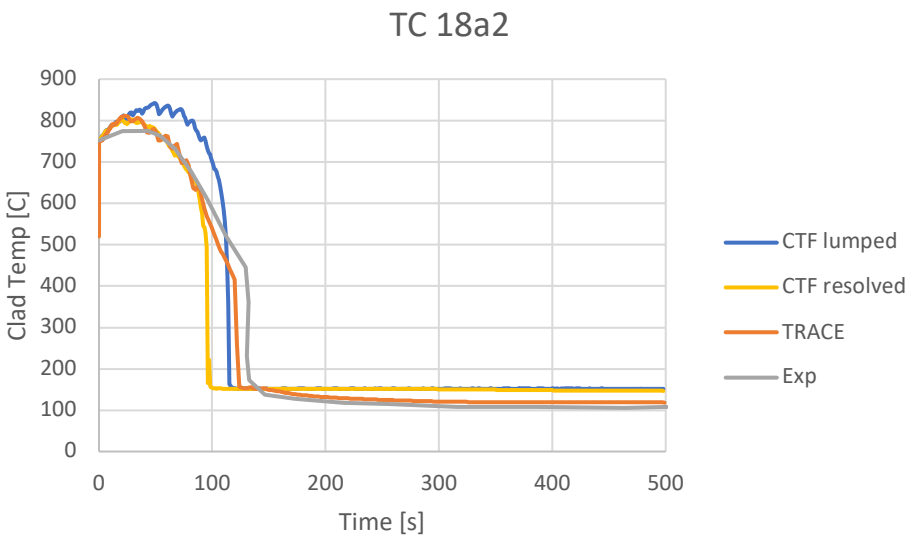

Figure *21*. Comparison of predicted and measured clad temperature at 18a2 (1,344 mm) location.

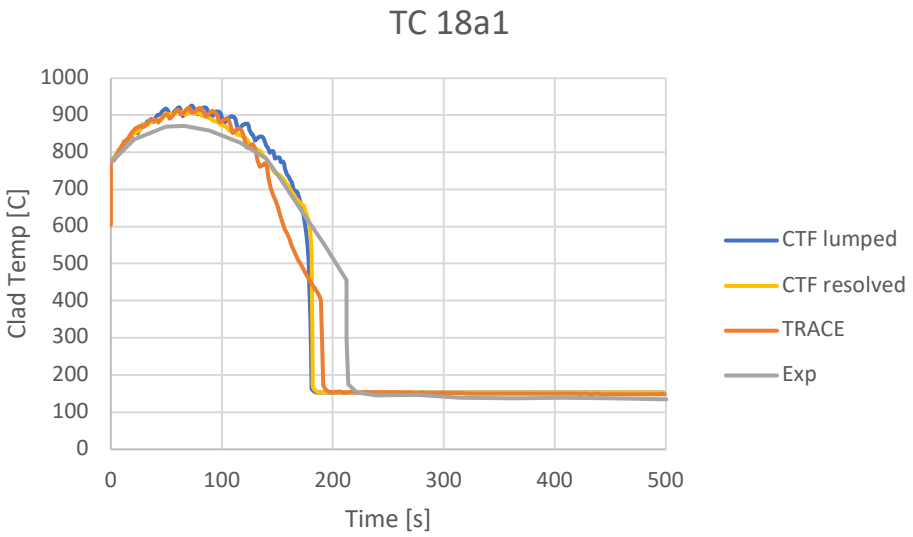

Figure *22*. Comparison of predicted and measured clad temperature at 18a1 (1,889 mm) location.

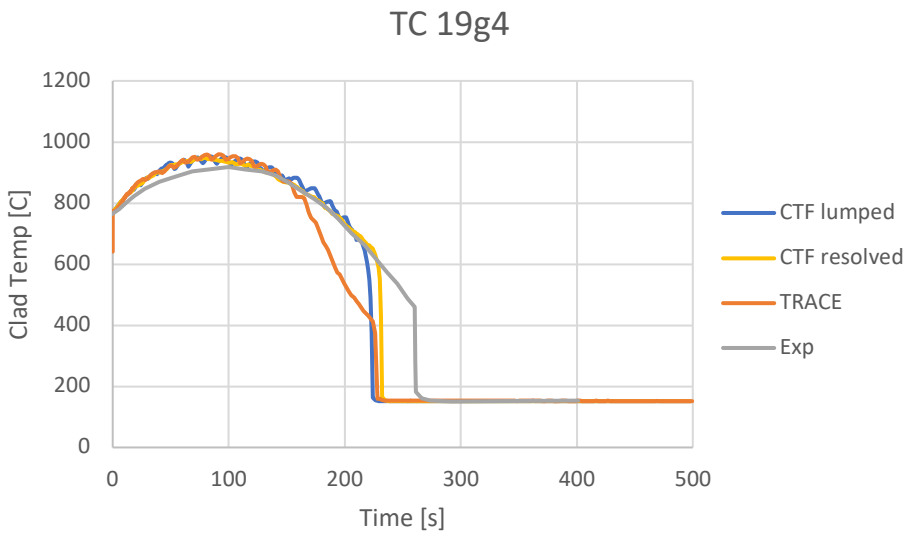

Figure *23*. Comparison of predicted and measured clad temperature at 19g4 (2,189 mm) location.

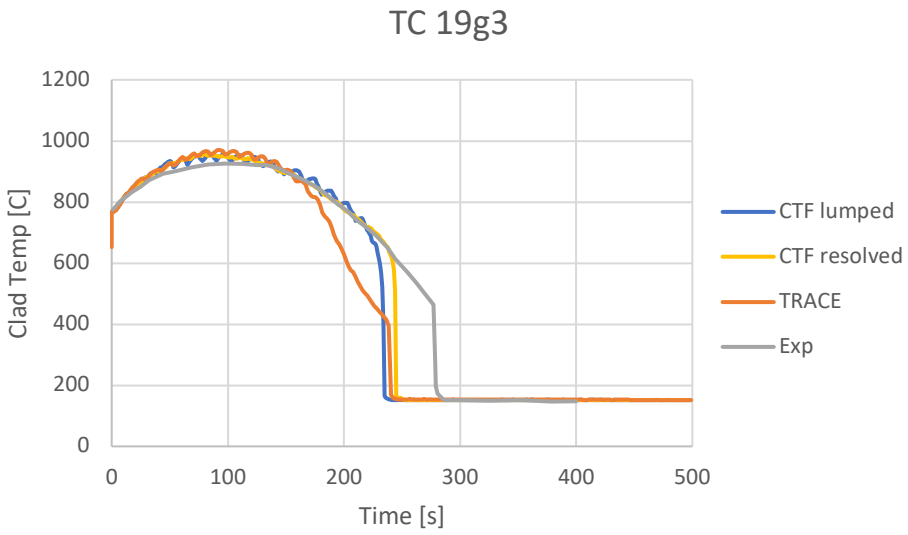

Figure *24*. Comparison of predicted and measured clad temperature at 19g3 (2,289 mm) location.

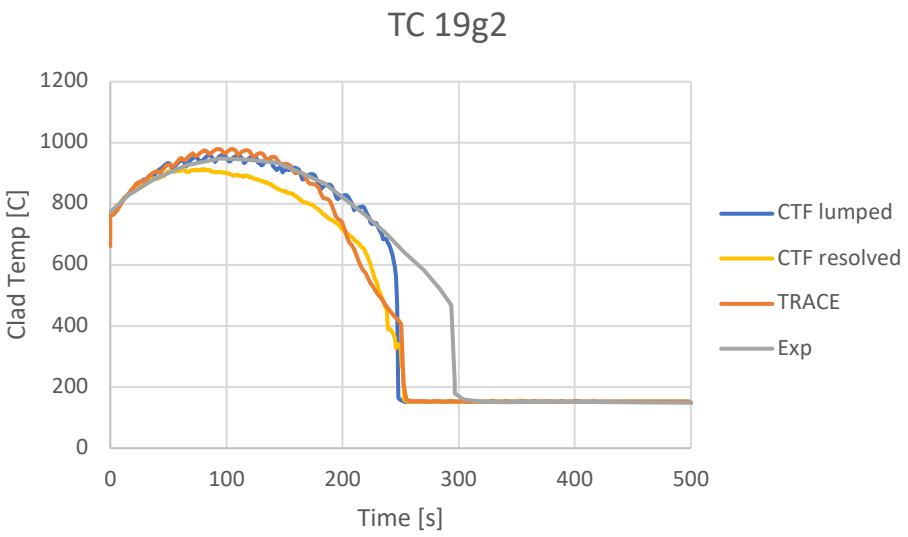

Figure *25*. Comparison of predicted and measured clad temperature at 19g2 (2,389 mm) location.

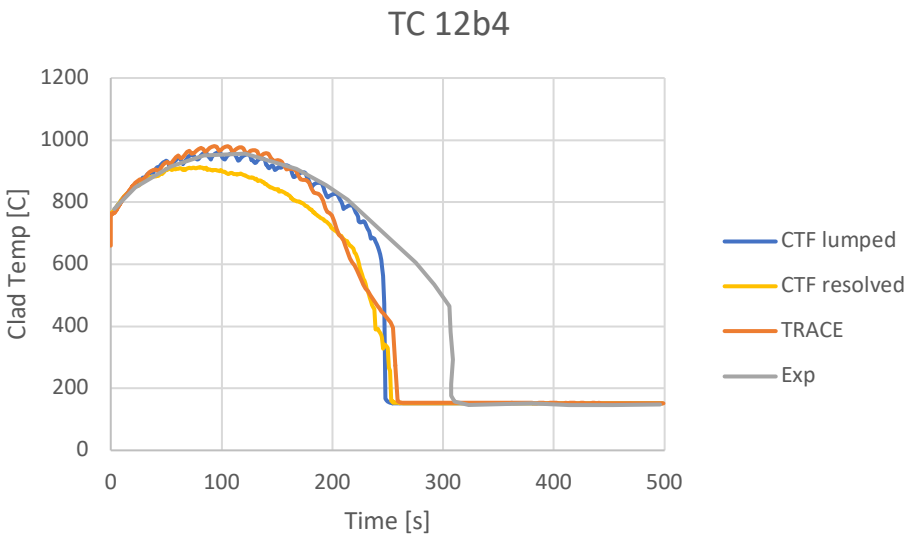

Figure *26*. Comparison of predicted and measured clad temperature at 12b4 (2,434 mm) location.

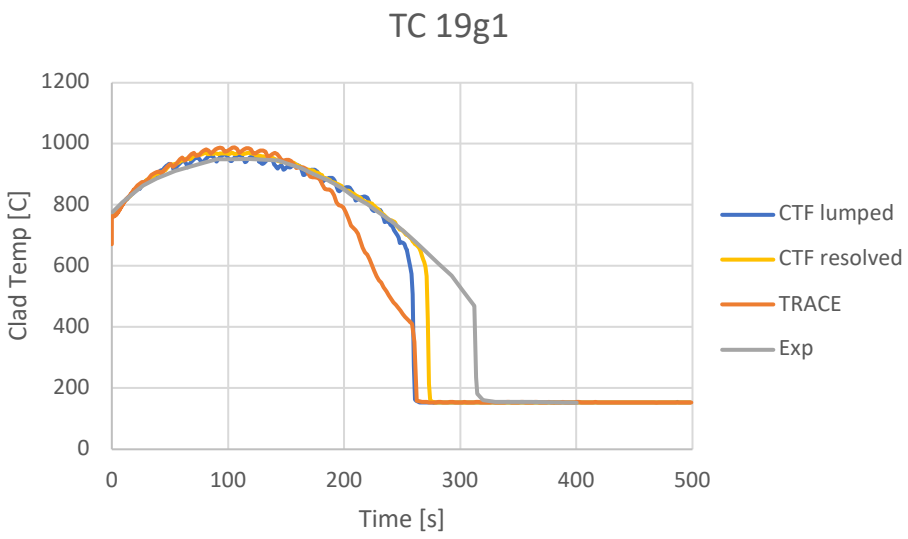

Figure *27*. Comparison of predicted and measured clad temperature at 19g1 (2,489 mm) location.

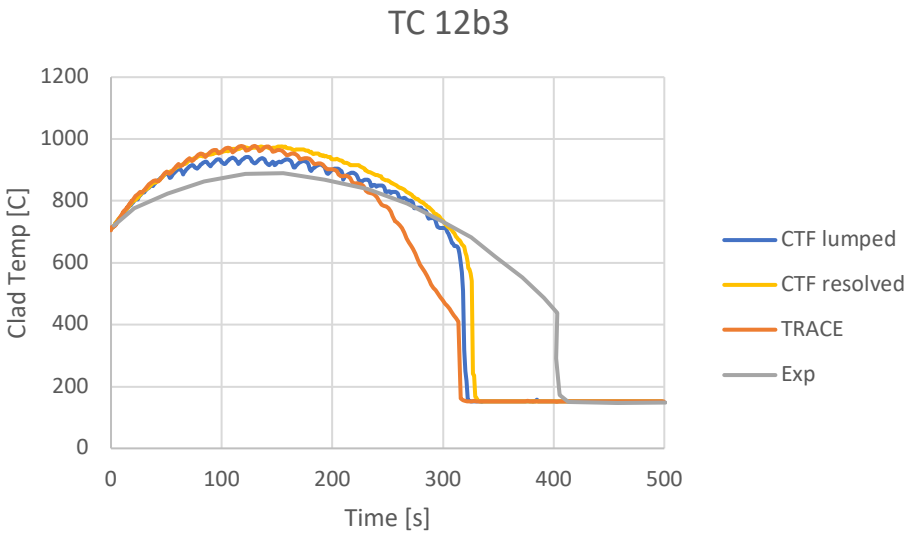

Figure *28*. Comparison of predicted and measured clad temperature at 12b3 (2,979 mm) location.

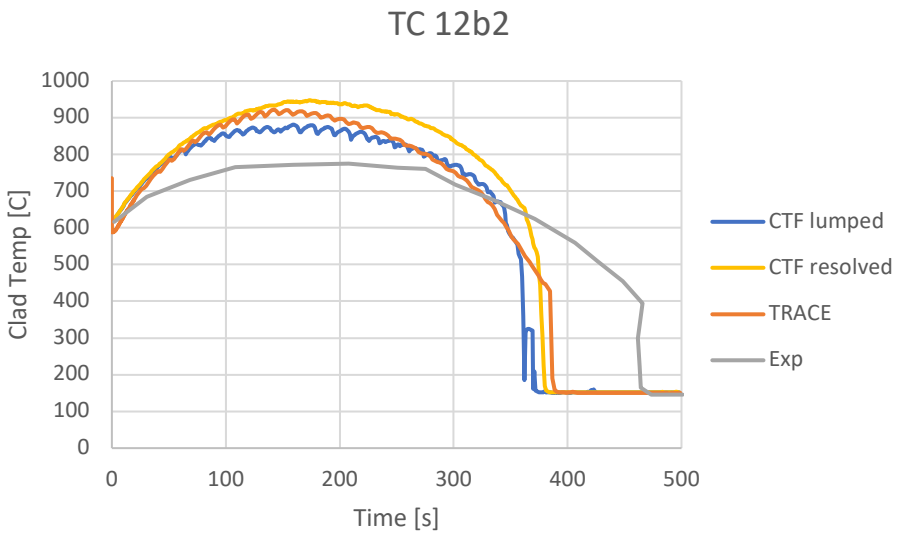

Figure *29*. Comparison of predicted and measured clad temperature at 12b2 (3524 mm) location.

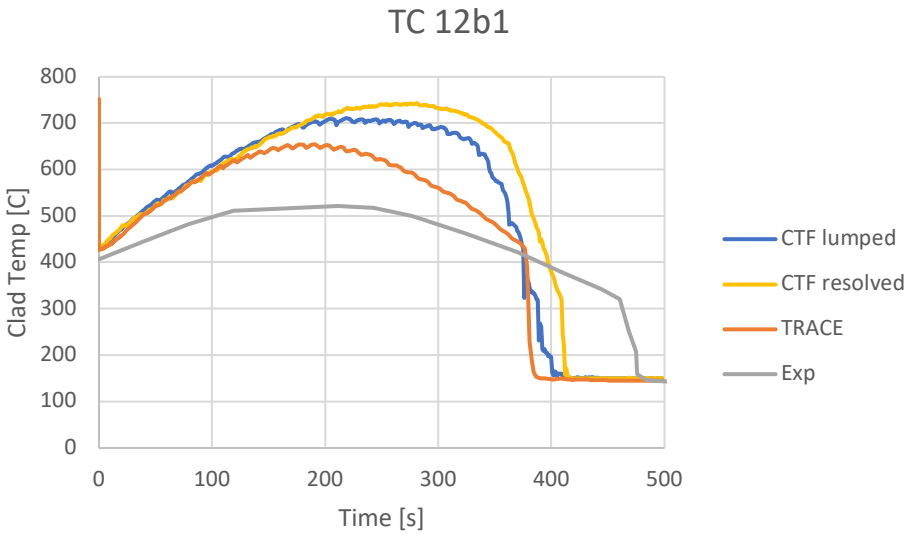

Figure *30*. Comparison of predicted and measured clad temperature at 12b1 (4069 mm) location.

In terms of quench time, CTF is quenching slightly faster than TRACE at the bottom of the bundle, but the lumped and TRACE models are quite agreeable moving up the bundle until the last thermocouple is reached, at which time TRACE is quenching faster than CTF. The pin-resolved model is always quenching faster than both the lumped CTF and TRACE models up until the top of the bundle. In comparison to experimental data, TRACE agrees with experimental data well for the first three locations, but then it starts to quench earlier than experimental data. CTF follows a similar trend of quenching too early.

In terms of PCT, the CTF-lumped model and the TRACE model are quite agreeable except for at locations 18a2 and 12b1. There is clearly a difference in heat transfer behavior prior to the quench, with

TRACE showing that the pins cool more rapidly than CTF prior to the quench. The agreement of these models with experimental data in terms of PCT is generally good for the lower parts of the bundle, but then the codes start to over predict the PCT near the top of the bundle. It is anticipated that the top of the bundle will be more difficult to predict because it is based on the cumulative behavior of what happens in the bottom of the bundle over the duration of the transient. For example, droplet entrainment and quench front velocity will impact the maximum temperatures seen in the top of the bundle. Furthermore, grid quenching effects at the top of the bundle, which are not being modeled by CTF, will also play a role in cooling the top of the bundle. The top thermocouple is the most poorly predicted. The CTF pin-resolved PCT is much lower than the lumped model PCT for thermocouples 19g2 and 12b4. It is agreeable with the lumped model for all other thermocouple locations until the top of the bundle. Note that thermocouples19g2 and 12b4 both face the center subchannel, whereas all other thermocouples face other subchannels, so there seems to be an issue with prediction of TH conditions in the center subchannel. A full symmetry resolved model was run to ensure that there is no issue with modeling the bundle in CTF using 1/8 symmetry; however, center pin thermocouple values were nearly identical to the results shown here. Further analysis of modeling impacts on clad temperature predictions follow after the remainder of experimental results are presented.

Figure 31 shows the behavior of the inner surface of the housing in both the lumped and resolved CTF models in comparison to experimental measurements. Recall that the initial temperature of the housing was modified so that the initial temperature agrees with experimental data. The lumped model may quench faster because the energy of the housing is more quickly dissipated into the interior of the bundle.

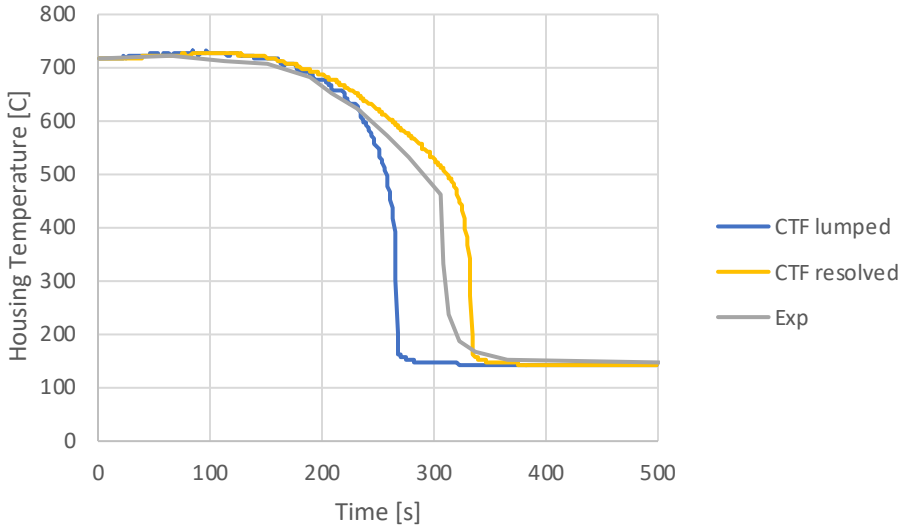

Figure *31*. **Housing temperature prediction compared to experiment (19g2 axial location).**

Bundle pressure drop was also measured in three different axial regions. **Figure** 32— through **Figure** 34 shows the bundle pressure drop in the lower, middle, and upper portions of the bundle, respectively. **Figure** 35 shows the total bundle pressure drop. The pressure drop will be primarily from gravitational head because of the low velocity of the quench front. Therefore, the pressure drop is mainly a measure of the void collapse as the bundle refills. TRACE is fairly consistent with experimental data in the lower portion of the core during the beginning of the transient, whereas CTF is overpredicting the liquid content at the same time. This is consistent with the faster quenching behavior predicted by CTF. Both codes are predicting faster void collapse in the middle portion of the bundle compared to experimental data. In the upper portion of the bundle, the experimental data shows a higher pressure drop starting at the beginning

of the transient. CTF eventually matches this pressure drop once the quench front starts to reach the top of the bundle, but TRACE continues to predict more void collapse until overpredicting pressure drop in the top of the bundle.

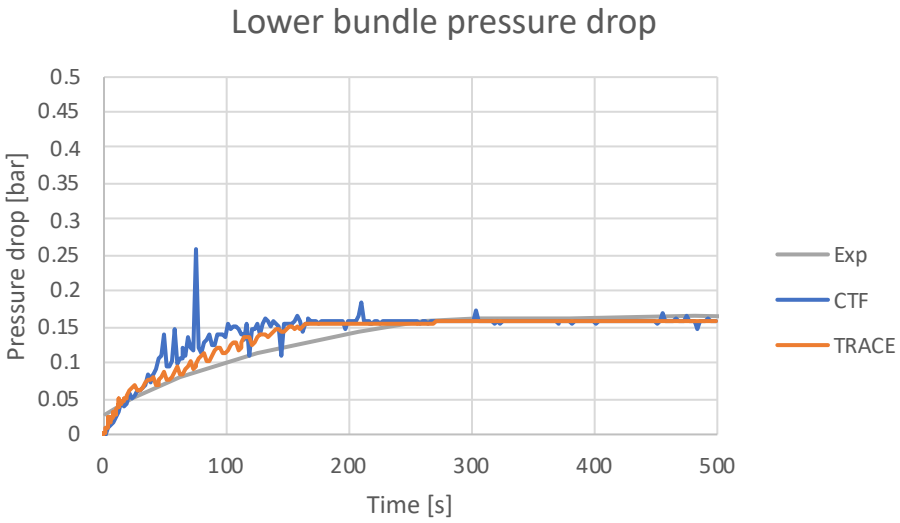

Figure *32*. Pressure drop predicted by TRACE and CTF in the lower axial region of the bundle.

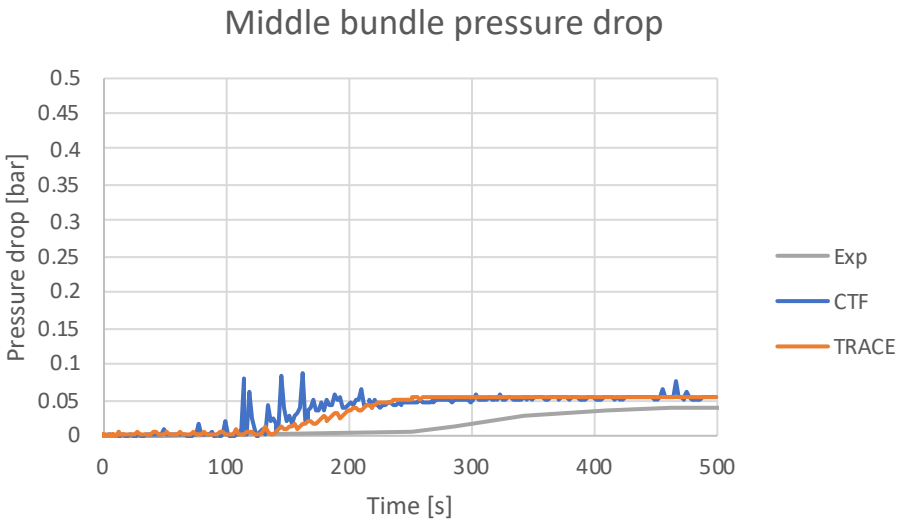

Figure *33*. Pressure drop predicted by TRACE and CTF in the middle axial region of the bundle.

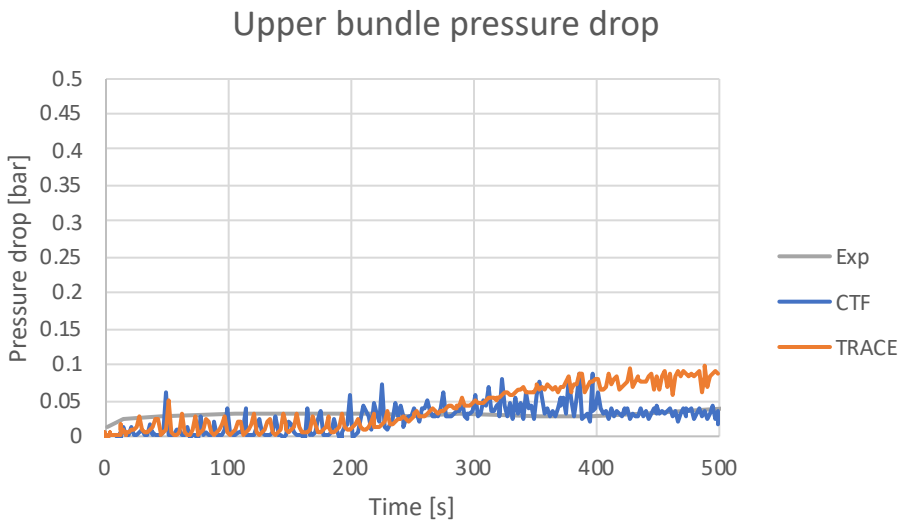

Figure *34*. Pressure drop predicted by TRACE and CTF in the upper axial region of the bundle.

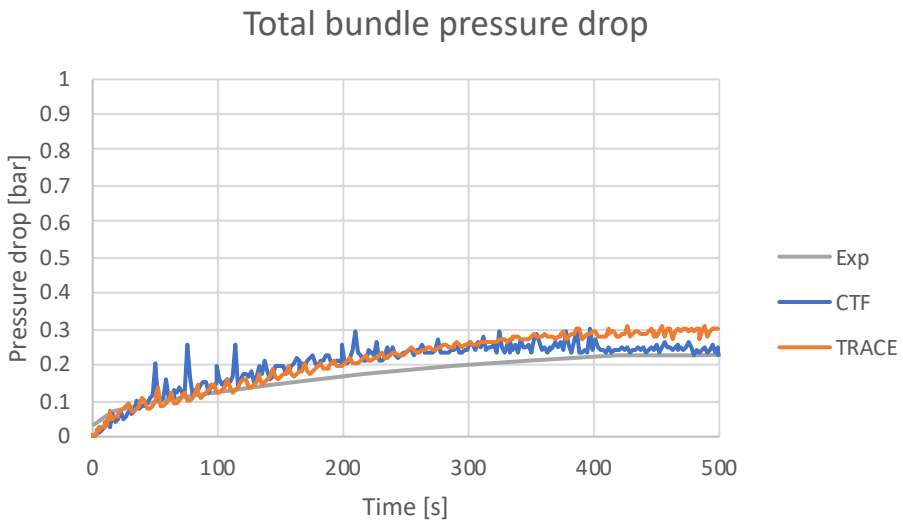

Figure *35*. Total bundle pressure drop predicted by TRACE and CTF.

Total droplet carryover over the duration of the transient is shown in **Figure** 36 for the CTF models (droplet carryover was not available in TRACE output). In the experiment, this was measured by separating droplets from the exiting flow and then collecting them in a tank. The tank completely fills at about 175 seconds, which is why the first 250 seconds of the transient are shown. The figure shows good agreement for the lumped case and experimental data and an under-prediction for the resolved case; however, it is important to recall that the experimental facility includes an orifice plate at the top of the bundle, which is not currently modeled in CTF. This plate will act to reduce carryover in the experiment, indicating that more entrainment may be needed in the CTF model to correctly capture total droplet carryover once that feature is added.

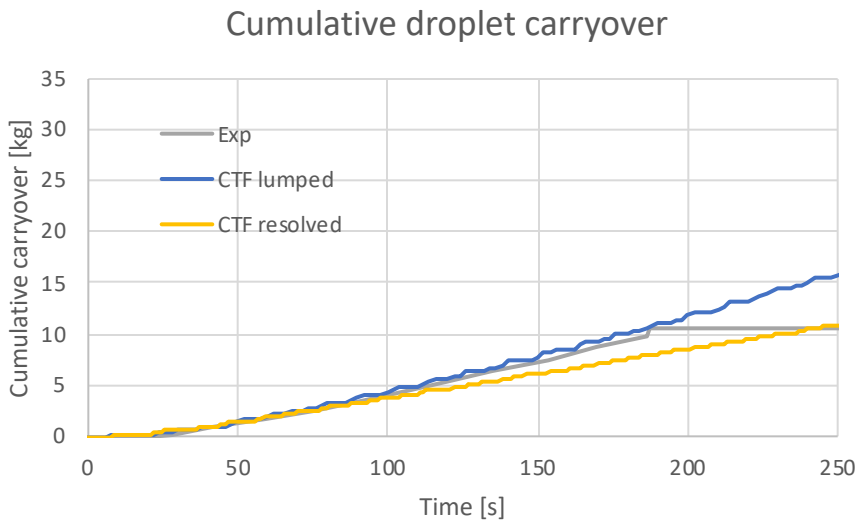

Figure *36*. Comparison of predicted and experimental cumulative droplet carryover.

Figure 37 shows the quench front location predicted by the different codes and models compared to experimental results. Note that CTF does not have a quench front tracking model, so the CTF quench front location is obtained by determining the time at which the surface temperature drops below 200 ºC. The TRACE results are obtained from its quench front tracking model. This clearly shows CTF overpredicting the quench speed throughout the transient. TRACE matches experimental results well in the first 120 seconds of the transient, as noted before, but then it begins to overpredict the quench velocity until it is consistent with CTF predictions. For the resolved case, the inner channel was selected for showing the quench behavior. As observed previously, the quench front velocity is slower for the perimeter channels near the housing. **Figure** 38 shows how the quench front location changes at different pin locations in the resolved model. In the legend, the "SE" acronym means "southeast pin quadrant" and "NE" means "northeast pin quadrant." Spacer grid locations are also marked to show their impact on the quenching profile. The pin quenches slightly earlier immediately downstream of the grid compared to the upstream location due to the impact of the grid cooling enhancement model. The fact that the housing is cooler at the top of the model is evident by observing how the boundary pin quadrant drops off quickly with the top of the pin quenching very early in the transient.

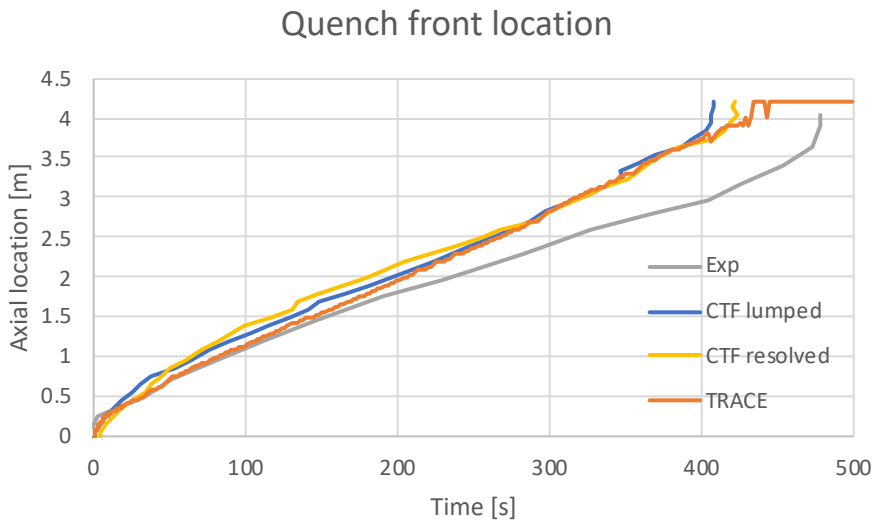

Figure *37*. Quench front location during the transient.

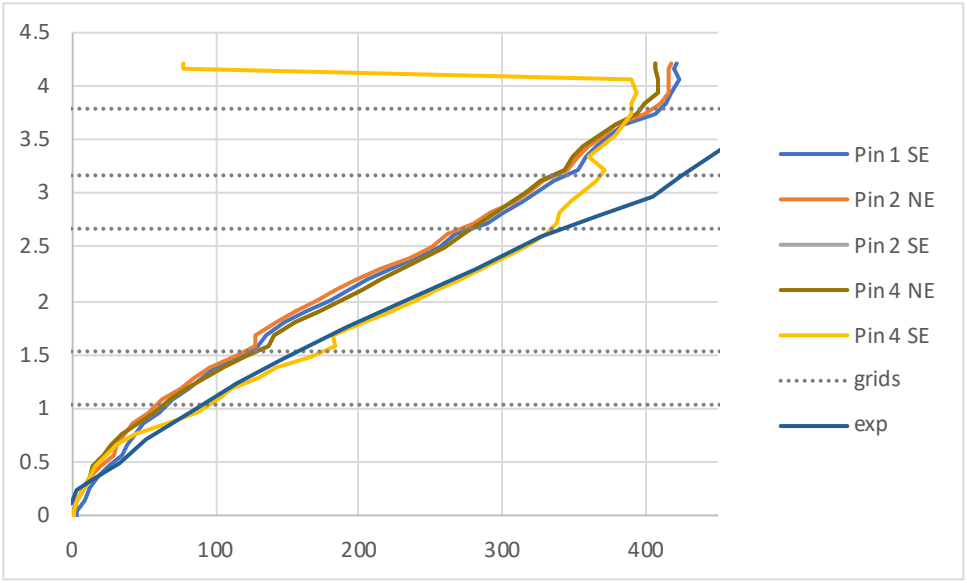

Figure *38*. Quench front location in individual pin locations.

3.4.3 CTF FEBA pin-resolved results assessment

To further investigate the impact of pin-resolved modeling, **Figure** 39 was generated to present the temperature behavior at the 19g2 level of the model. Note that the pin numbers in the model are from the pin-resolved model and the numbers correspond to the indices in **Figure** 7. Therefore, Pin 1 is the center pin, and Pin 4 is the one closest to the housing. For each pin, the southeast sector of each pin is shown. It is observed that the PCT is higher and the quench time is delayed in the channels closer to the housing. The housing is a significant mass which will be at the same temperature as the superheated vapor at the start of the transient, so it will have the effect of delaying quench in the boundary channels. The lumped model will be uniformly affected by the impact of the housing in the radial direction because there is only one flow channel that receives all the heat from the lumped pin and housing, which helps to explain why it quenches later than the center pin in the resolved model.

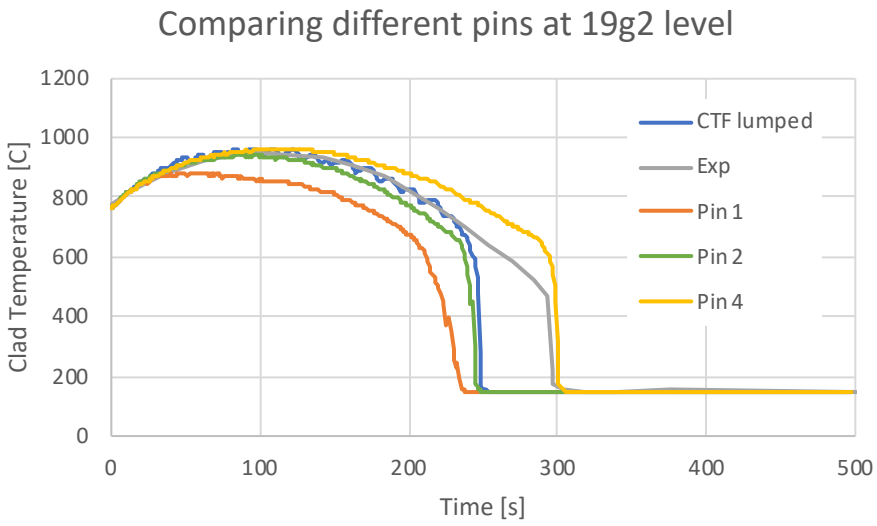

Figure *39*. Comparison of different radial locations in the bundle at the 19g2 level in CTF.

To further analyze the differences of different pins, **Figure** 40 shows the impact of shutting off the entrainment model. The dashed lines represent the behavior of the base model, and the solid lines show the behavior when entrainment is disabled. The interior pin sees a very strong impact of droplet entrainment on PCT. The presence of the droplets significantly reduces PCT in the interior channel, but to a lesser degree in channels closer to the housing. Quench time is largely unaffected in the interior channels, but it is faster in the periphery channel than it was with entrainment enabled.

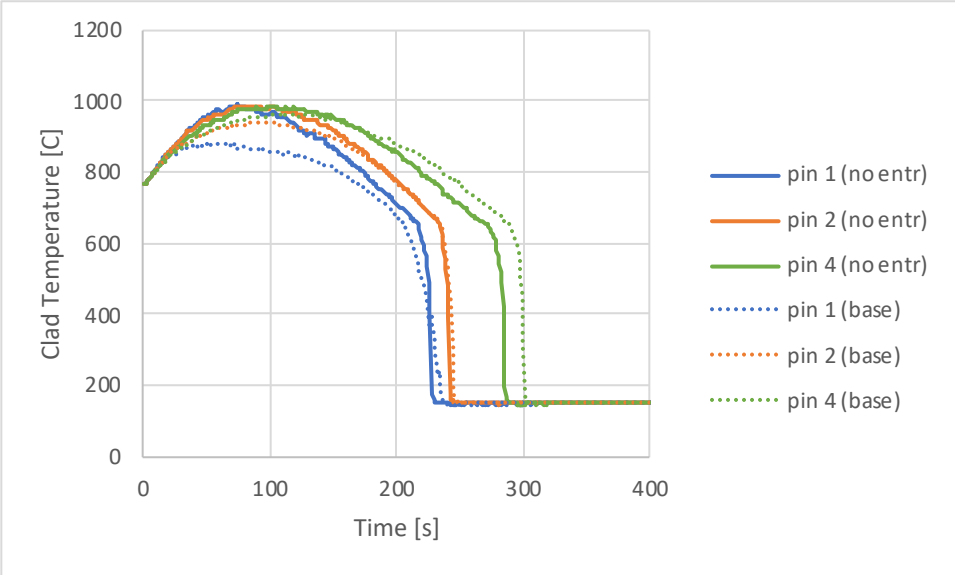

Figure *40*. Impact of entrainment on CTF resolved model results.

In **Figure** 41, the entrainment model is enabled, but cross-flow is disabled. In this case, the behavior in the interior channels is expected to be small because the channels are geometrically identical, and without cross flow, they should not experience an impact from the housing. The figure indicates there are some discrepancies between the interior channels, although they may be caused by the azimuthal conduction of

heat through the rods or numerical instability. Generally, the results agree well, and a marked difference is observed with the channel near the housing. This figure indicates that the interior pins never quench, but they continue to cool throughout the transient. **Figure** 42 shows the entrainment flow rate throughout the transient at the 19g2 level for this case in the inner and periphery channels. Note that a moving average covering a 20 s period was used to smooth the data enough for a trend to be seen. The results indicate that droplet mass flow rate increases in the inner channel until it is equal to the inlet mass flow rate, which helps to explain why the pins never quench. The droplets cool the pins down gradually, but the sharp quench is never observed. For the sake of comparison, **Figure** 43 shows the entrainment behavior in these channels when the cross-flow is enabled. In this case, the entrainment flow in the periphery is lower at the beginning of the transient and higher in the inner channel, perhaps indicating that the cross-flow is allowing droplets to migrate into the bundle center where they help to cool the rods, but it also delays the quench of the periphery channel. After the inner channels quench, there is a surge of droplet entrainment entering the periphery of the channel until the channel quenches. These figures illustrate the importance of the droplet entrainment behavior and indicate that further assessment of these models may be necessary to more accurately predict PCT and quench time.

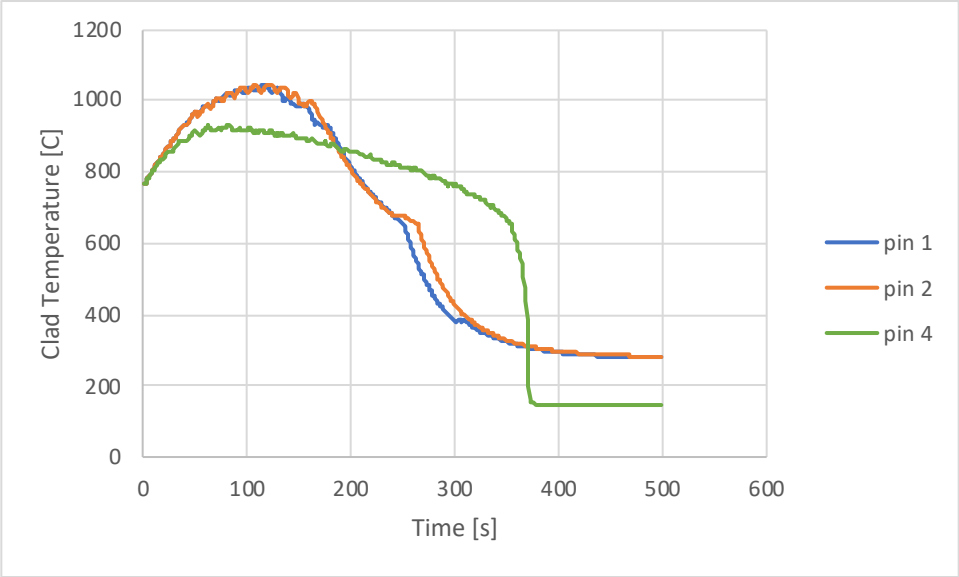

Figure *41*. Impact of disabling cross-flow in the CTF pin-resolved model.

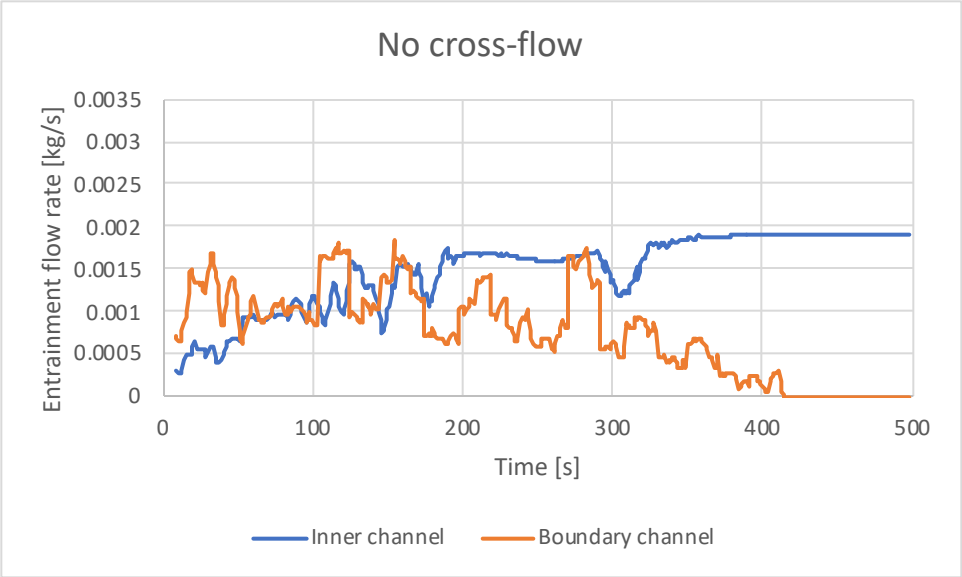

Figure *42*. Entrainment flow rate behavior in inner and periphery channels when cross-flow is disabled.

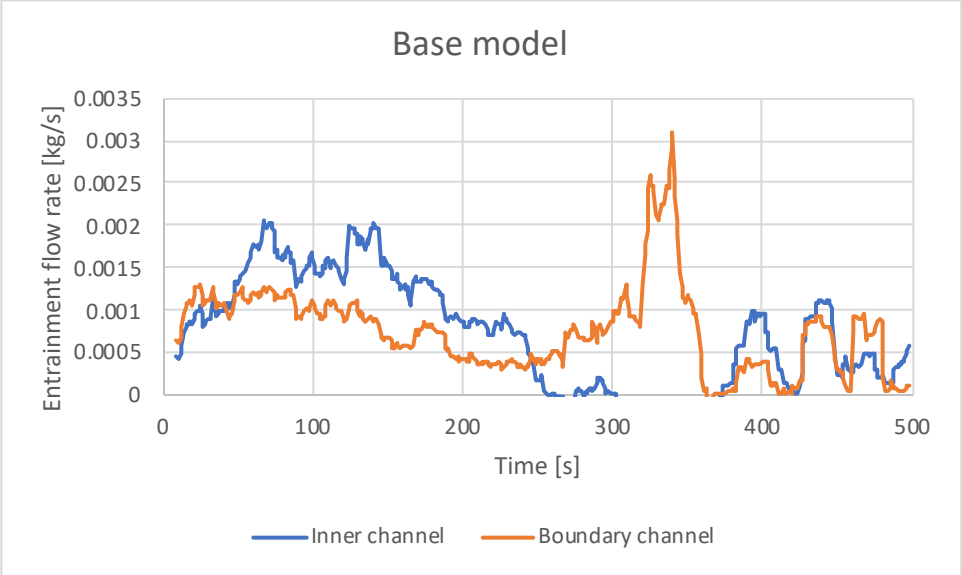

Figure *43*. Entrainment mass flow rate behavior in inner and periphery channels in the base model with cross-flow enabled.

3.4.4 Assessment of CTF advanced spacer grid models

Two models were not included in the analysis presented above: the spacer grid quenching model and the grid droplet breakup model. These models were not included because only limited information on the spacer grids was available to properly set up the models; however, it is important to at least assess their impact on the solution using reasonable estimates of spacer grid geometry, which were discussed in Section 3.2.1. **Figure** 44 through **Figure** 47 show the impact of the droplet breakup model, which captures the impact of droplets shattering into smaller droplets when they impact into the spacer grids. These results were generated using the lumped model version of FEBA Case 229. This will result in a larger interfacial area and enhanced heat removal from the vapor phase. Only the middle to upper thermocouple

results are shown because there is relatively no impact on the lower locations. The results tend to agree with expectations, with PCT values being lower because of enhanced heat transfer. In some cases, results agree more closely with experimental values. Because the shattered droplets will evaporate more easily, the carryover is reduced compared to the base model.

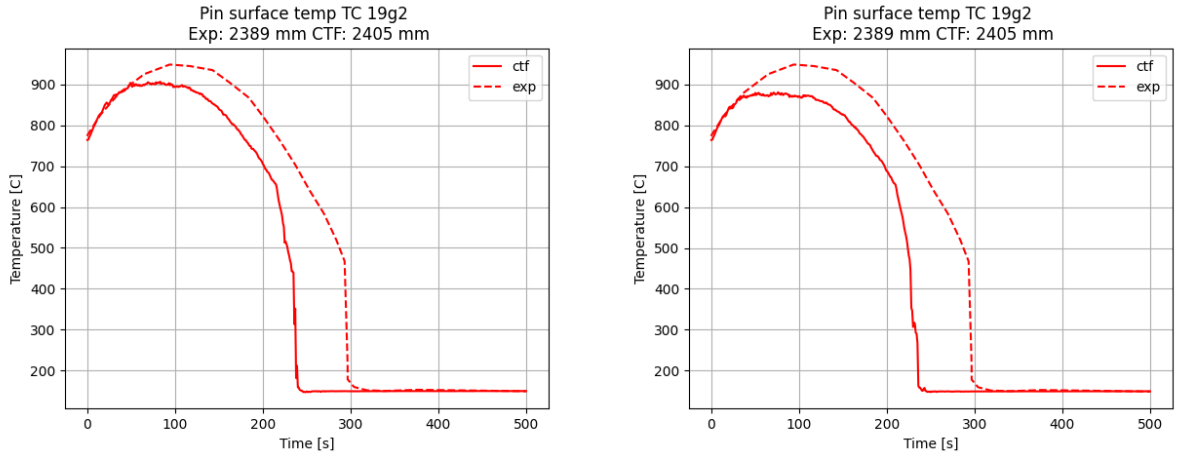

Figure *44*. Impact of the droplet breakup model (right) compared to base model (left) for the lumped case at the 19g2 level.

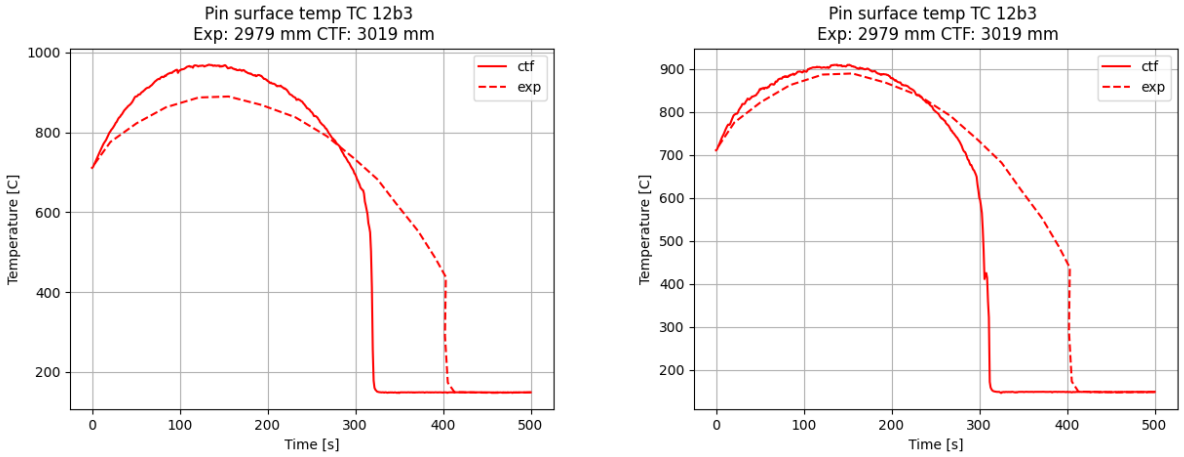

Figure *45*. Impact of the droplet breakup model (right) compared to base model (left) for the lumped case at the 12b3 level.

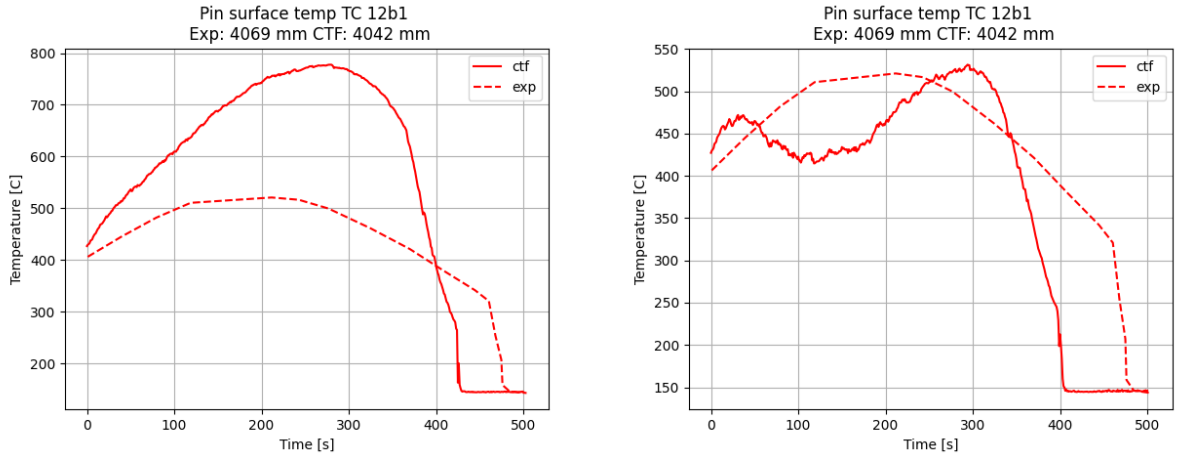

Figure *46*. Impact of the droplet breakup model (right) compared to base model (left) for the lumped case at the 12b1 level.

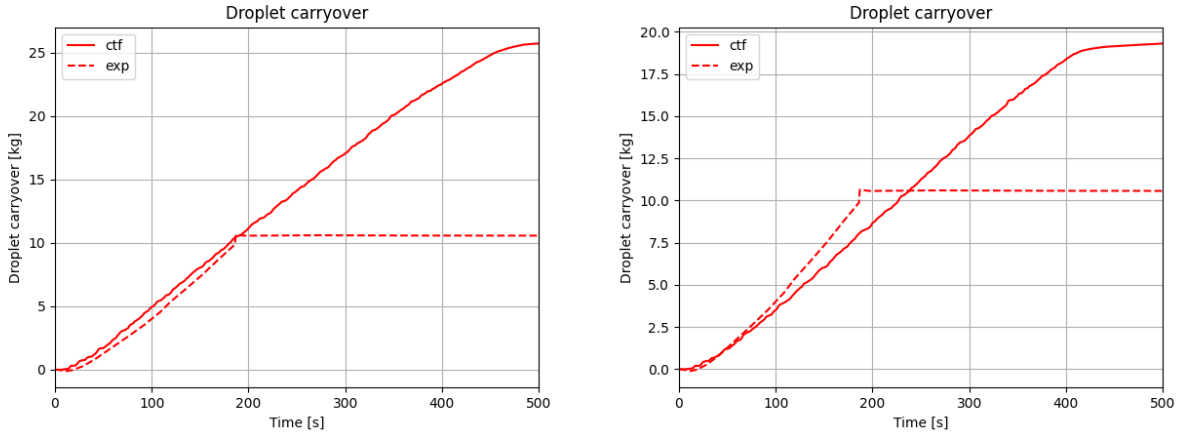

Figure *47*. Impact of the droplet breakup model (right) compared to base model (left) on droplet carryover for the lumped case.

In **Figure** 48 through **Figure** 50 the spacer grid quenching model is enabled and the droplet breakup model is disabled. At the 19g2 level, there is essentially no impact on temperature behavior resulting from the absence of the middle spacer grid. At the higher levels, the quenching of the spacer grids leads to cooling of the vapor and lower PCT. The droplet carryover is slightly reduced because of droplets de-entraining on the spacer grids rather than exiting the top of the model as shown in **Figure** 51. **Figure** 52 and **Figure** 53 show the fraction of the spacer grid that is quenched as the transient progresses. The bottom grid quickly becomes fully quenched, whereas the top grid takes hundreds of seconds to quench and oscillates between partially and fully quenched until near the end of the transient.

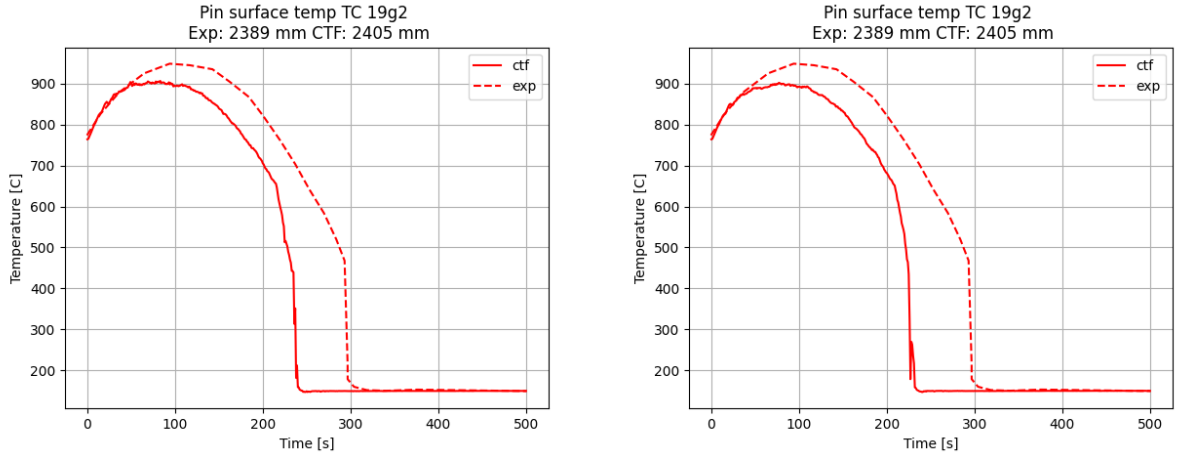

Figure *48*. Impact of the spacer grid quenching model (right) compared to base model (left) on clad temperature at level 19g2.

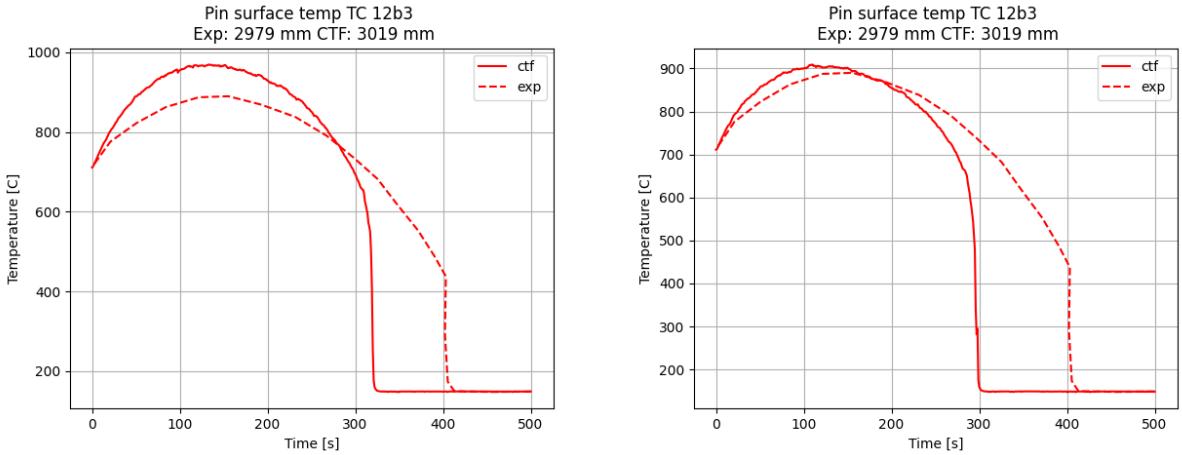

Figure *49*. Impact of the spacer grid quenching model (right) compared to base model (left) on clad temperature at level 12b3.

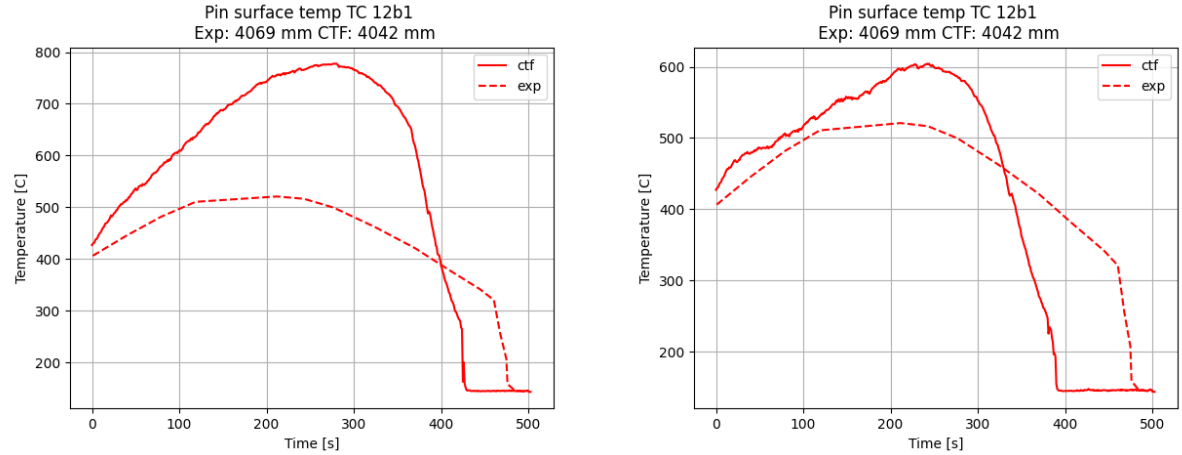

Figure *50*. Impact of the spacer grid quenching model (right) compared to base model (left) on clad temperature at level 12b1.

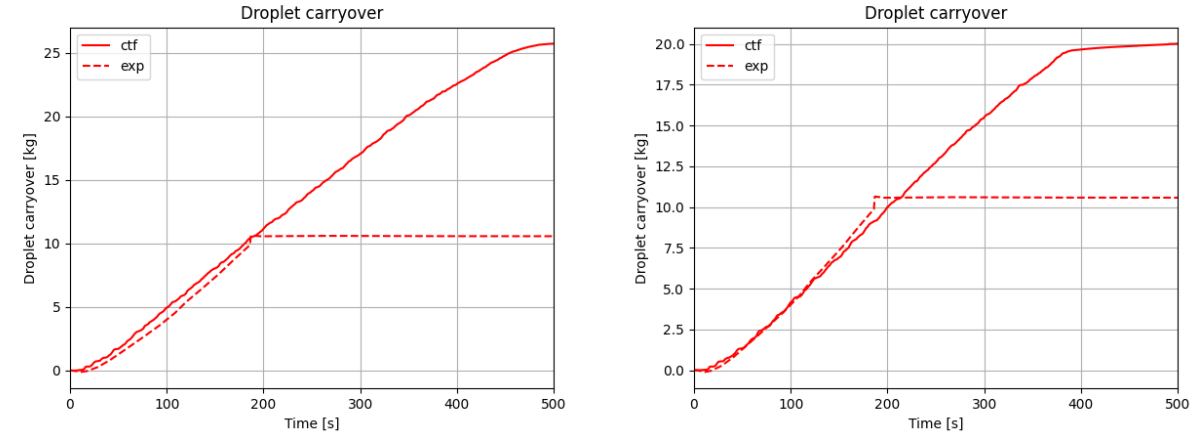

Figure *51*. Impact of the spacer grid quenching model (right) compared to base model (left) on droplet carryover.

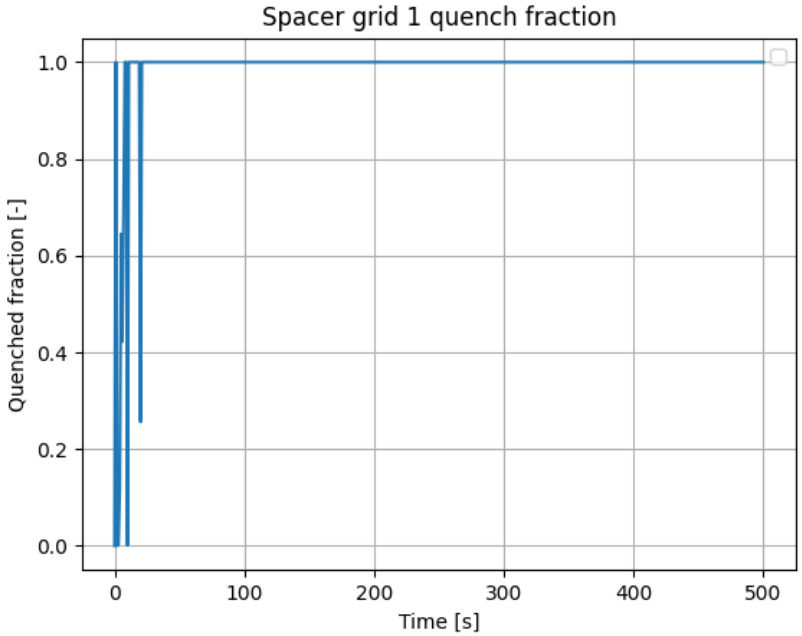

Figure *52*. Fraction of the bottom spacer grid that is quenched (covered in liquid film) throughout the transient.

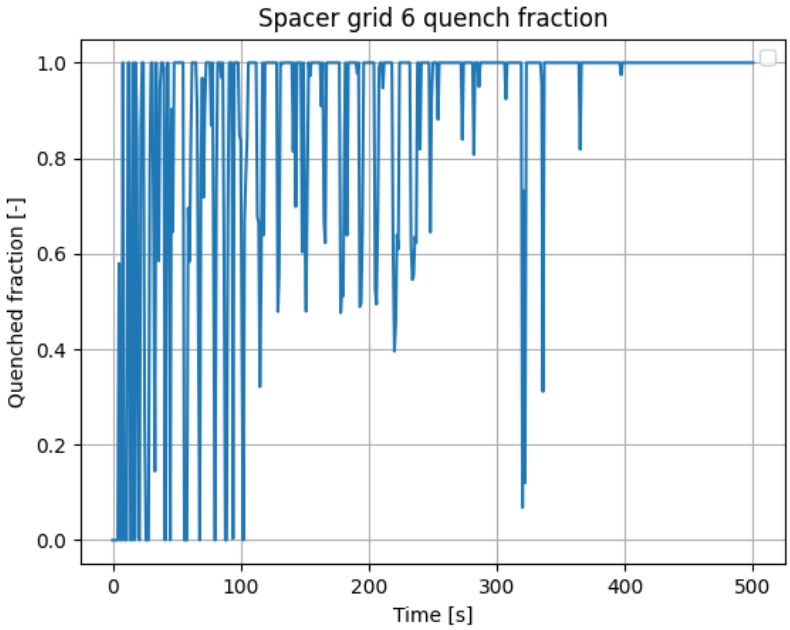

Figure *53*. Fraction of the top spacer grid that is quenched throughout the transient.

3.4.5 Assessment of impact of flooding rate

The impact of flooding rate was assessed by modeling FEBA test case 228, which uses the same outlet pressure as Case 229 but raises the flooding velocity from 3.8 cm/s to 5.7 cm/s. The feedwater temperature is essentially the same between the two tests (38 C for Case 229 vs. 37 C for Case 228). Lumped versions of the FEBA facility were used for both cases to do the comparison. The initial axial temperature profile, transient temperature forcing function, and inlet mass flow rate were adjusted in Case 228 case to match the values given in the FEBA specification. **Figure** 54 through **Figure** 60 show the transient clad temperature behavior during the transients. Like in previous figures, the solid red lines show CTF results, and the dashed red lines show experimental results. In addition to these results, the CTF-predicted heat transfer mode is also shown by the blue line. The value of the heat transfer mode is given by the secondary (right) y-axis. The meanings of each of these integer values are provided in **Table** 13. In each figure, the subfigure on the left shows the Case 228 result, and the subfigure on the right shows the Case 229 result.

Table *13*. Description of CTF heat transfer mode integer values

Heat Transfer Mode ID	Heat Transfer Mode
1	Single-phase liquid convection
2	n/a
3	n/a
4	Subcooled-nucleate boiling
5	Saturated-nucleate boiling
6	Transition boiling
7	Inverted annular film boiling (IAFB)
8	Transition between IAFB and dispersed flow film boiling (DFFB)
9	DFFB
10	Single-phase vapor convection

The results show that the PCT is lower and the pins quench faster for all axial levels. CTF agrees with this trend. However, at both flooding rates, CTF is always predicting an earlier quench. In terms of PCT, CTF over-predicts PCT more often for the low-flooding rate case. The PCT of the high flooding-rate case is generally better predicted than the low-flooding rate case. It is observed that pure IAFB is rarely encountered, which requires local void dropping below 0.6. The transition region between IAFB and DFFB is encountered slightly more frequently in the high-flooding case, which is the expected behavior because a higher flooding rate allows the subcooled liquid to penetrate further into the hot region of the core. As soon as transition boiling is encountered, the pin quenches very quickly, and the heat transfer mode transitions to subcooled or saturated boiling. Because CTF predicts the pins cooling too quickly, leading to an early quench, further review of the DFFB and IAFB heat transfer models and transition criteria may be needed.

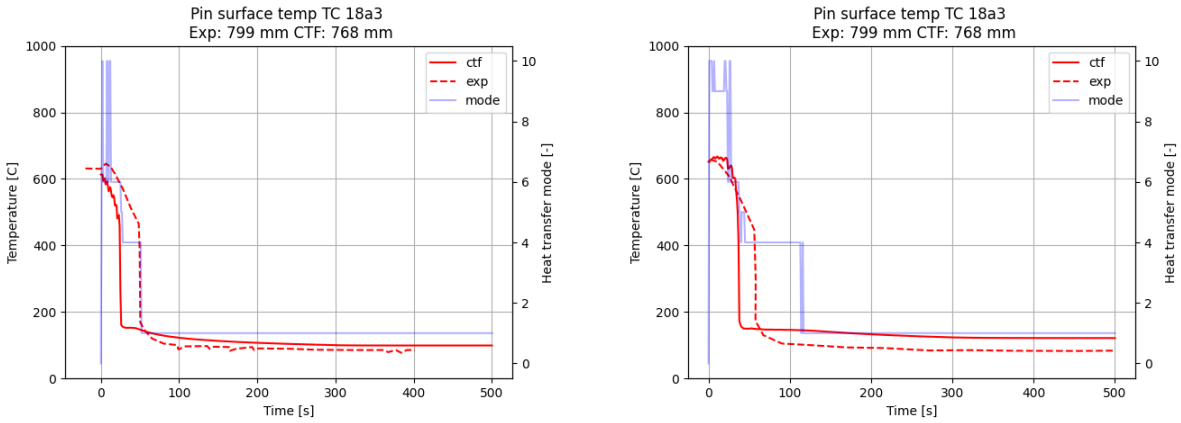

Figure *54*. Comparison of clad temperature behavior at 18a3 level for Case 228 (left) and Case 229 (right).

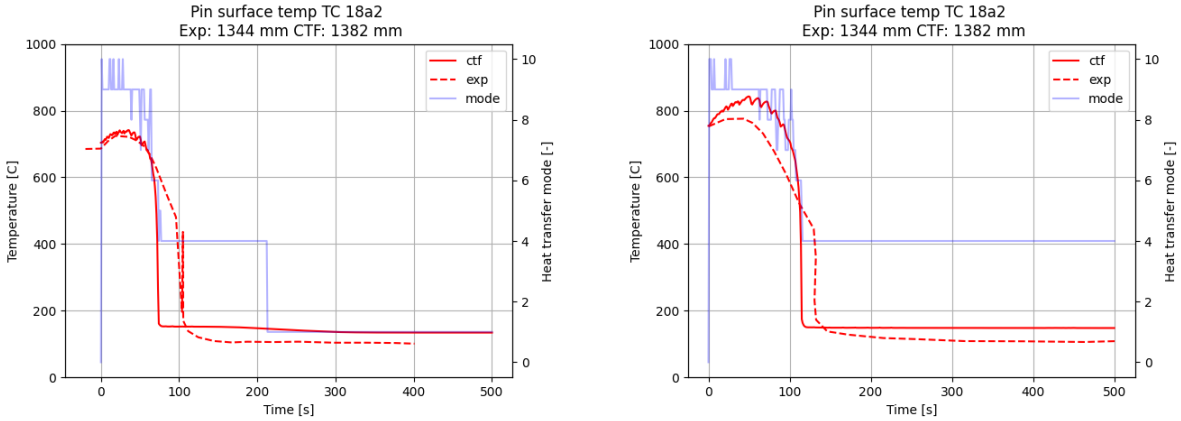

Figure *55*. Comparison of clad temperature behavior at 18a2 level for Case 228 (left) and Case 229 (right).

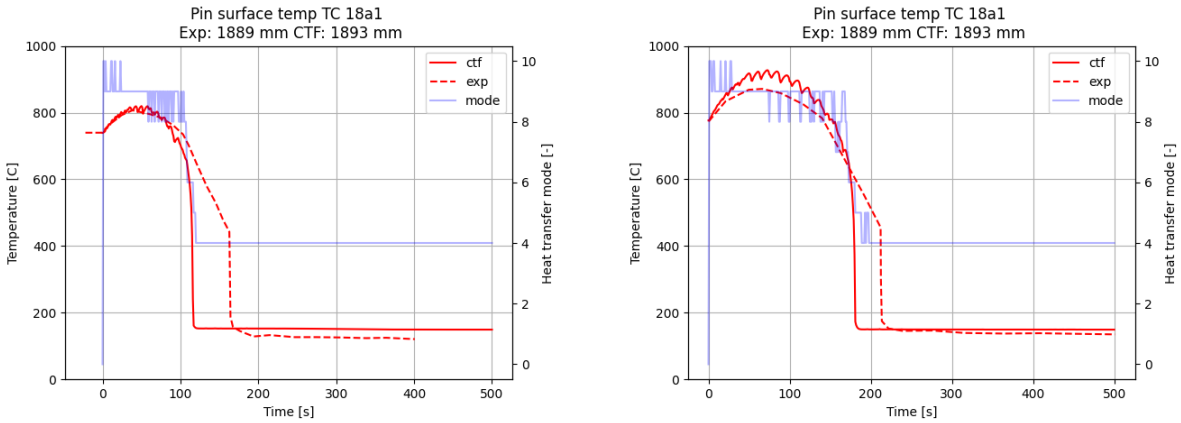

Figure *56*. Comparison of clad temperature behavior at 18a1 level for Case 228 (left) and Case 229 (right).

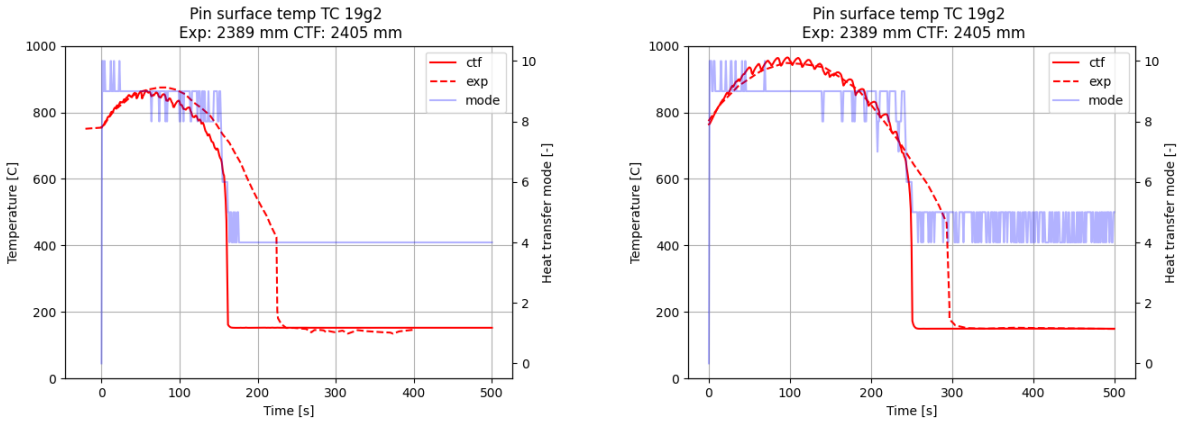

Figure *57*. Comparison of clad temperature behavior at 19g2 level for Case 228 (left) and Case 229 (right).

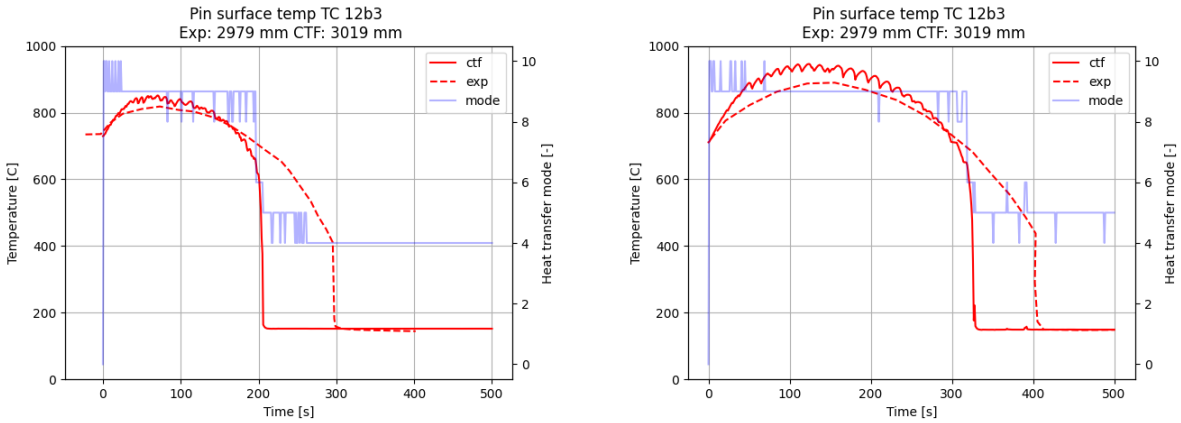

Figure *58*. Comparison of clad temperature behavior at 12b3 level for Case 228 (left) and Case 229 (right).

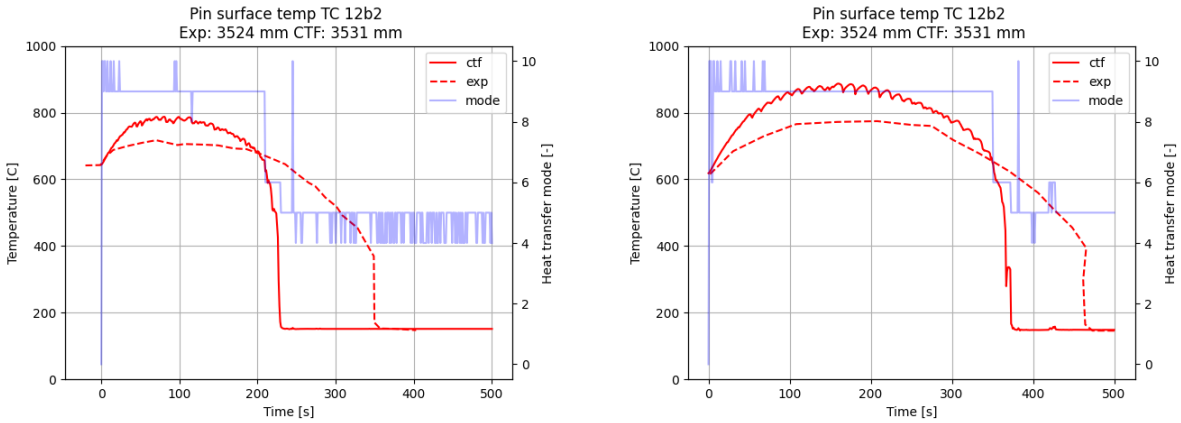

Figure *59*. Comparison of clad temperature behavior at 12b2 level for Case 228 (left) and Case 229 (right).

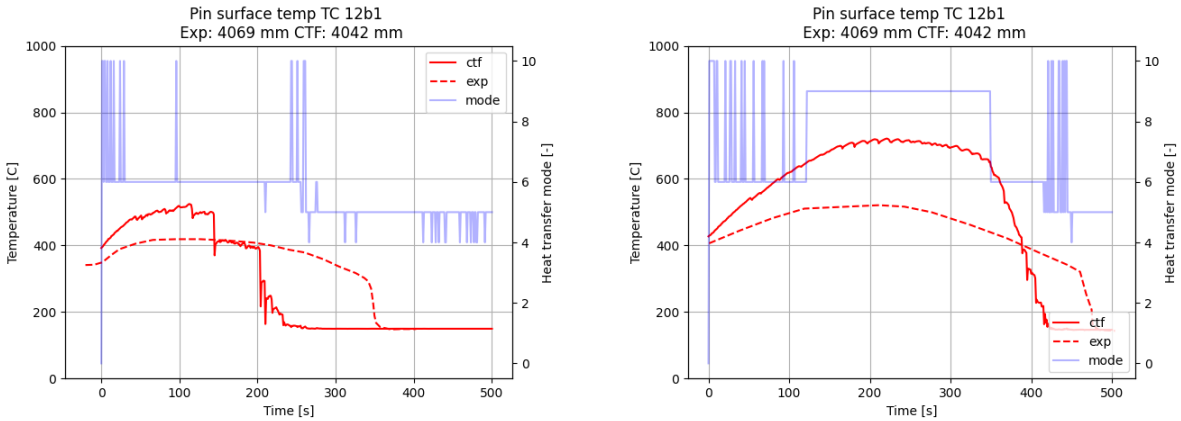

Figure *60*. Comparison of clad temperature behavior at 12b1 level for Case 228 (left) and Case 229 (right).

Figure 61 shows the droplet carryover for both cases. There is a delay of about 25 seconds before carryover begins in the high flooding rate case, which CTF does not capture. It is not clear why this is the behavior in the experiment, but it is noted that the inlet flow was very chaotic in the first 30 seconds of the transient, as shown in Figure 165 of the FEBA specification (Ihle & Rust, FEBA---Flooding Experiments with Blocked Arrays Data Report 1, Test Series I through IV, 1984). Transient forcing functions were used in the CTF model to capture both the inlet flow and inlet temperature transient behavior, but because the functions were digitized from the figure, there may be inaccuracies. CTF does capture the time at which the collection tank fills (125 seconds into the transient), though because carryover starts sooner in CTF, the CTF time would likely be closer to 150 seconds if the 25 second delay were added. Either way, this is considerably sooner than for Case 229, which doesn't fill until 200 seconds due to the lower flooding rate. CTF is able to capture the behavior of carryover being higher for a higher flooding rate, as seen in the experiments.

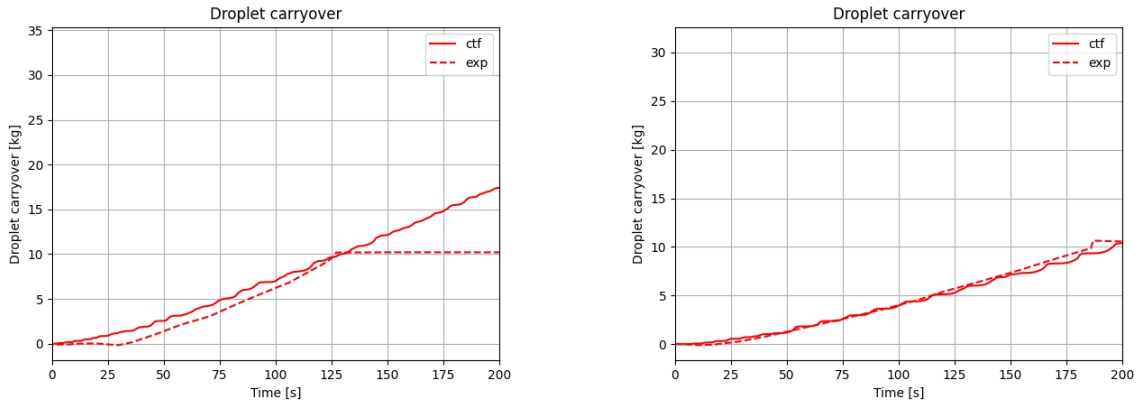

Figure *61*. Comparison of droplet carryover behavior for Case 228 (left) and Case 229 (right).

Figure 62 shows the bundle pressure drop behavior for the two cases. Like in the lower flooding rate case, the void is collapsing faster than the experiment in the middle of the bundle due to faster quenching. While CTF predicts too little void in the low flooding rate case, it predicts too much void in the upper part of the bundle in the high flooding rate case. At around 250 s, the void solution becomes fairly stable, whereas it continues to reduce in the experiment, indicating potentially insufficient interfacial heat transfer for the high flooding rate case.

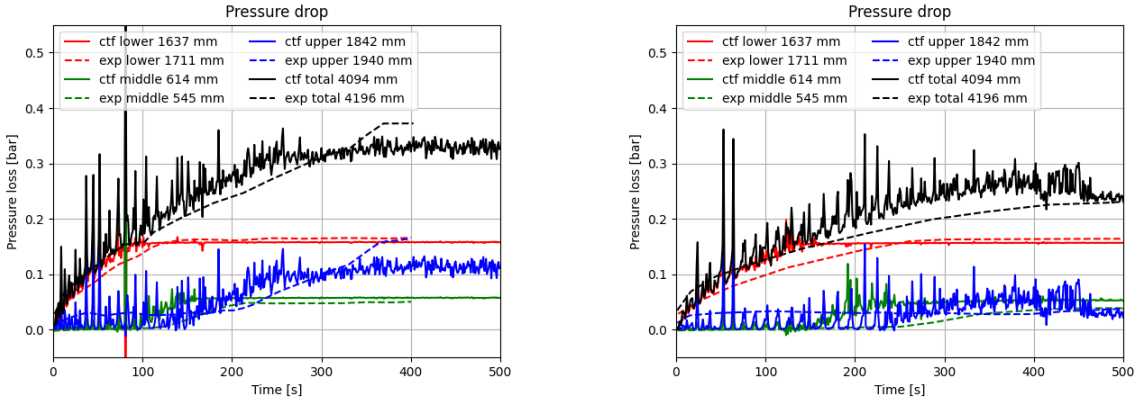

Figure *62*. Comparison of bundle pressure drop behavior for Case 228 (left) and Case 229 (right).

3.4.6 Assessment of impact of inlet enthalpy

The FEBA tests do not significantly vary feedwater temperature. Feedwater is between 35 and 50 °C during each transient. A code-to-code benchmark was performed using TRACE to investigate the impact of increasing feedwater temperature. A lumped version of FEBA Case 229 was used as a basis. The flooding velocity, initial temperature, and LHR were set to match FEBA test conditions, and the FEBA pin geometry was used. However, the axial power shape was obtained by averaging the axial power shape of all pins in a high burnup assembly (see E-10 in **Figure** 69) to give the model a more realistic power shape. The forcing function on inlet temperature was removed so that it was constant throughout the transient. Three versions of each model were run, with the only change between models being the inlet enthalpy. The cases had inlet enthalpies of 150, 300, and 450 kJ/kg.

Figure 63 through **Figure** 67 show the predicted PCT from both CTF and TRACE at selected axial levels. The blue line is for the 150 kJ/kg inlet enthalpy, orange is for 300 kJ/kg, and green is for 450 kJ/kg. CTF predicts a reasonable behavior for the mid-bundle 1.4 m location. The PCT is lower for the high inlet enthalpy compared to the lower inlet enthalpy cases. This is expected because a higher inlet enthalpy leads to more vapor generation, higher vapor velocity, and thus higher vapor convective heat transfer rates in the DFFB heat transfer regime. Furthermore, the 450 kJ/kg case quenches later than the lower inlet enthalpy cases, which has also been observed in experiments. However, this behavior does not persist when moving up the bundle. The PCT continues to be lower for the 450 kJ/kg case, but it also starts to quench before the lower inlet enthalpy cases. CTF heat transfer regimes at two locations are shown in **Figure** 68. On the left, the value at the correctly predicted 1.4 m location is shown, and on the right, the value at the higher incorrectly predicted 2.9 m location is shown. At both locations, the lower inlet enthalpy cases are experiencing more IAFB heat transfer, whereas the higher inlet enthalpy case stays in DFFB until the pin quenches. This is likely the correct behavior, so this may indicate that the heat transfer being predicted by the CTF DFFB model is too high, which causes faster cooling of the pin in the 450 kJ/kg case when compared to the lower enthalpy cases that experience more IAFB, which should lead to a faster quench of those pins.

As for the TRACE results, the PCT is largely unchanged for different inlet subcooling values, and the relationship between inlet enthalpy and quench time looks correct.

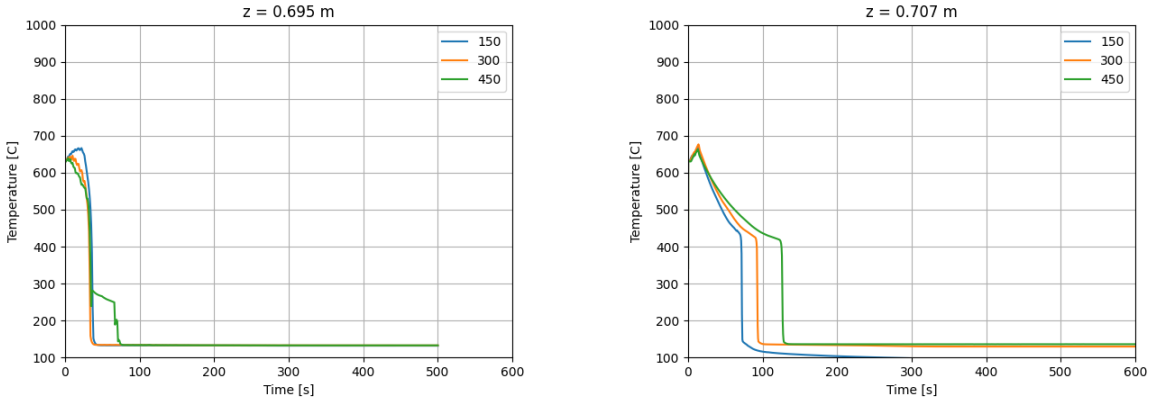

Figure *63*. CTF (left) and TRACE (right) PCT behavior for inlet enthalpy values of 150, 300, and 450 kJ/kg at ~0.7 m.

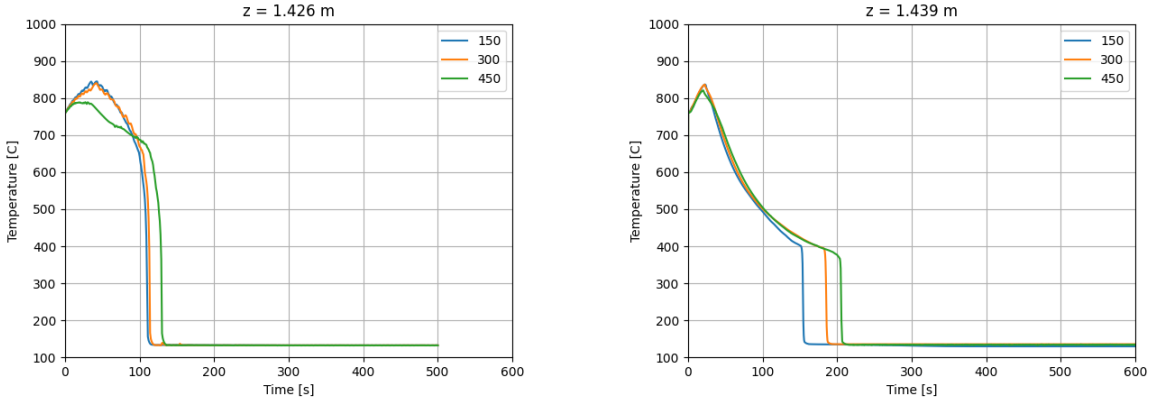

Figure *64*. CTF (left) and TRACE (right) PCT behavior for inlet enthalpy values of 150, 300, and 450 kJ/kg at ~1.4 m.

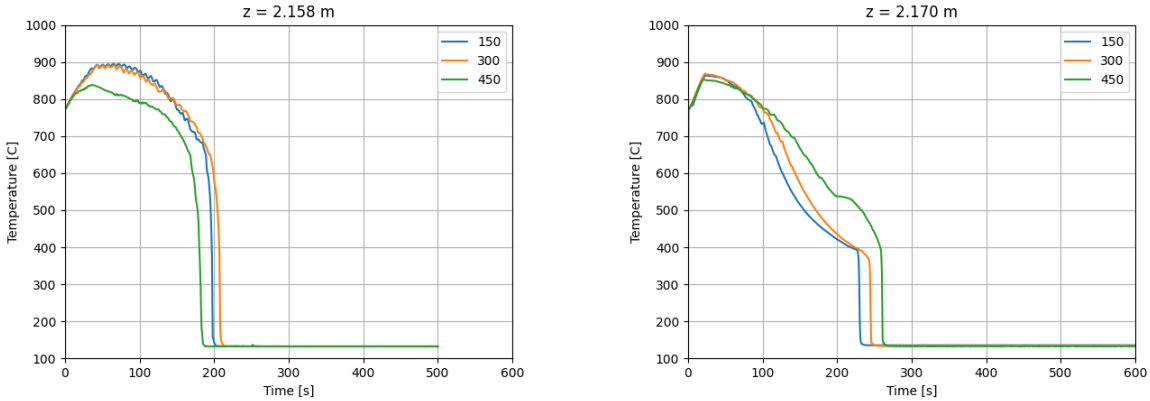

Figure *65*. CTF (left) and TRACE (right) PCT behavior for inlet enthalpy values of 150, 300, and 450 kJ/kg at ~2.1 m.

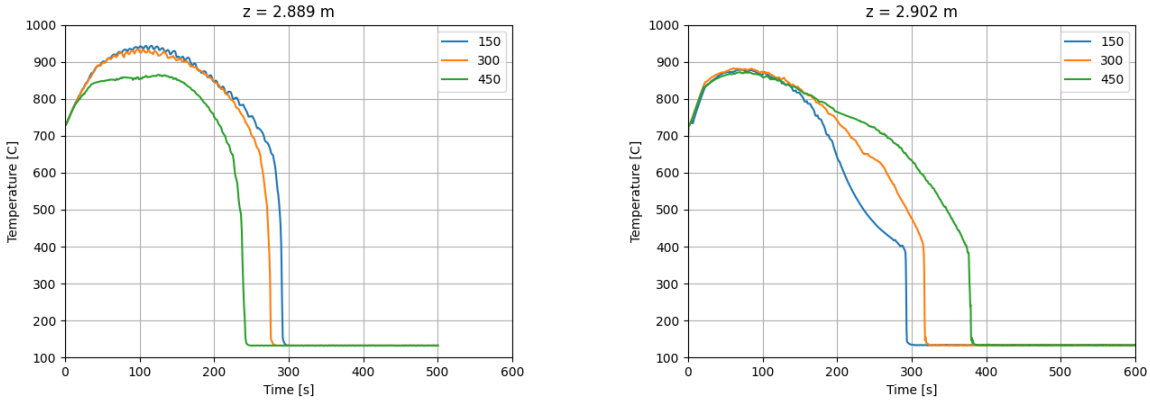

Figure *66*. CTF (left) and TRACE (right) PCT behavior for inlet enthalpy values of 150, 300, and 450 kJ/kg at ~2.9 m.

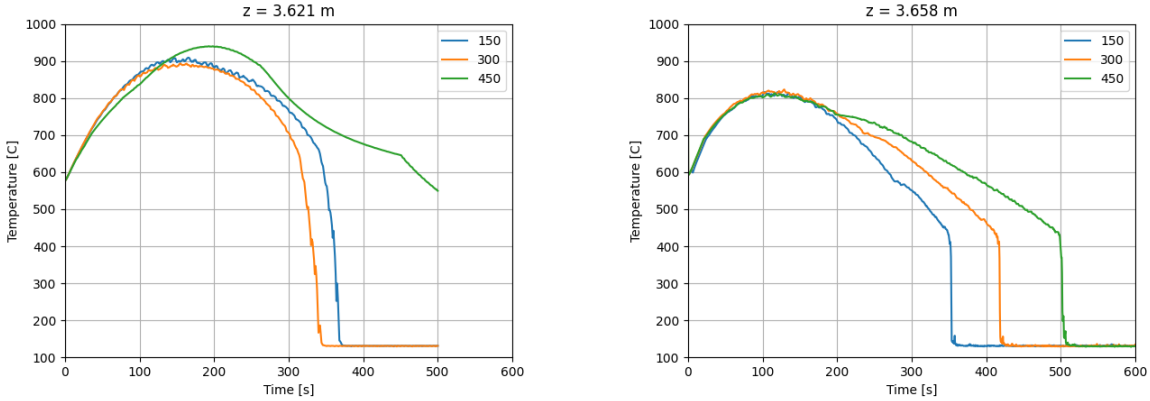

Figure *67*. CTF (left) and TRACE (right) PCT behavior for inlet enthalpy values of 150, 300, and 450 kJ/kg at ~3.6 m.

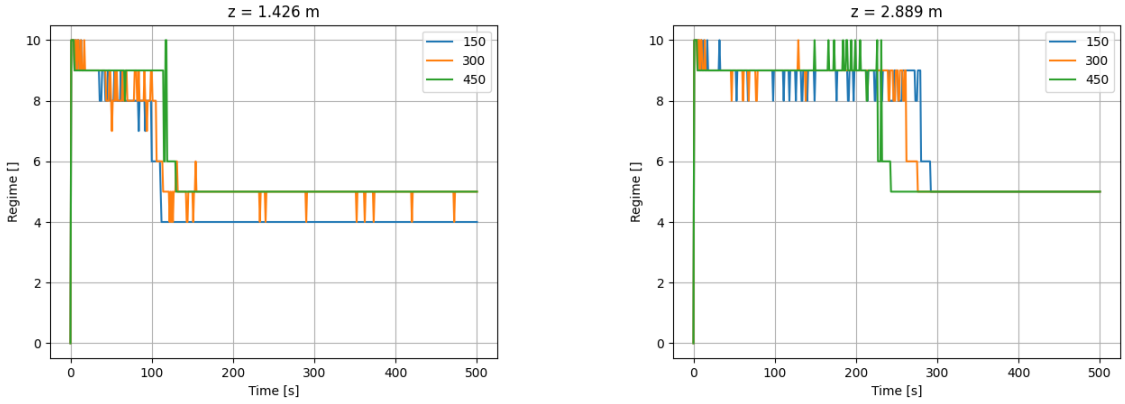

Figure *68*. CTF heat transfer regime behavior at mid- (left) and upper- (right) bundle locations.

4. High Burnup Use Case

4.1 High Burnup Core Demonstration

To investigate the impact of using pin-resolved modeling for a high-burnup core, a VERA model was constructed for a 4-loop PWR and depleted to end-of-cycle. A 24-month cycle was run with previously burned assemblies shuffled to create the high-burnup core seen in **Figure** 69. Because running a LOCA reflood transient for the entire core is computationally expensive, a subregion of the core around the high-burnup assembly located at the E-10 location (shown with the black box in **Figure** 69) was selected. A full-core, pin-resolved calculation should not take much more walltime than the subregion case because the parallelization decomposes the problem into similar size sub-problems, but it will require more processors, which will reduce the turnaround time of results compared to the subregion case. Note that the high-burnup assembly is surrounded by low-burnup assemblies on three of its sides. The radial power distribution for this subregion is shown in **Figure** 70. Two versions of the model were generated in CTF: one model used full pin resolution (2,601 pins in the model) with all lateral connections, and a second model used one channel per assembly for consistency with the TRACE model and to allow for benchmarking.

Because the neutronics plays very little part in the solution during the actual LOCA transient, the case was run by standalone TRACE and standalone CTF. The 3D power distribution was extracted from the VERA results and used to set the peaking factor distribution in the code models. The linear power and transient power forcing function were set to match the FEBA power behavior during the reflood transient. Only the reflood portion of the transient is modeled. The inlet temperature of the model was set to 38 °C, with the FEBA inlet temperature forcing function used for Case 229 applied. The initial pin temperature used in the FEBA Case 229 was used for the initial axial pin temperature distribution for all pins in the core. A flooding rate of 3.8 cm/s was targeted, and the outlet pressure was set to 2.5 bar. The model was totally voided at the beginning of the transient. These boundary and initial conditions were identical between the TRACE and CTF models. The geometry of the 17×17 fuel bundles and nuclear fuel pin geometry were used for constructing the TH models, which included fuel pins with 9.5 mm in diameter with the dynamic gap conductance model enabled. The axial discretization was set to 25 axial levels. Modeling options (e.g., turbulent mixing, CHF, boiling heat transfer) that were used for FEBA assessment with CTF were used for the subregion case, as well.

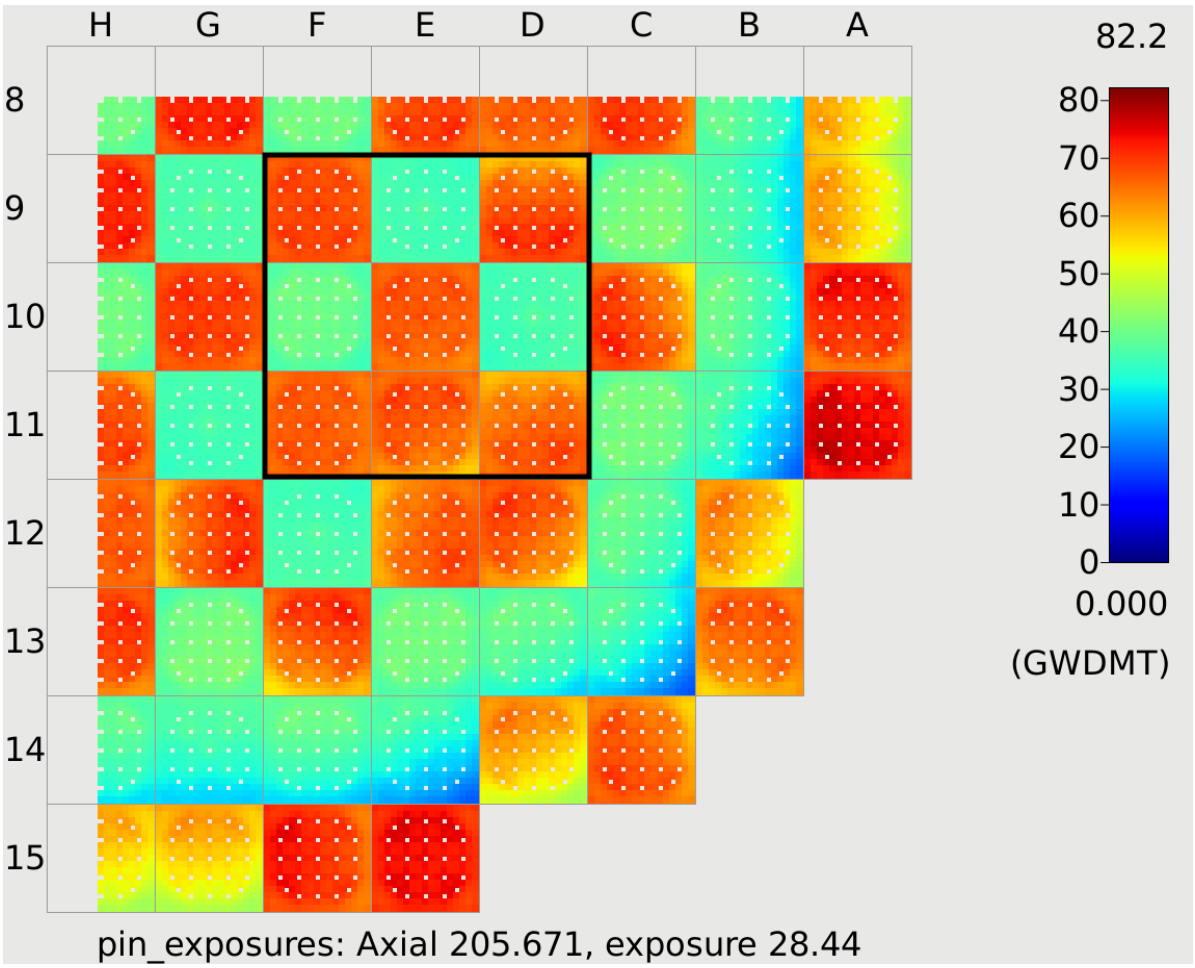

Figure *69*. Radial burnup distribution at end-of-cycle in a high-burnup 4-loop PWR core.

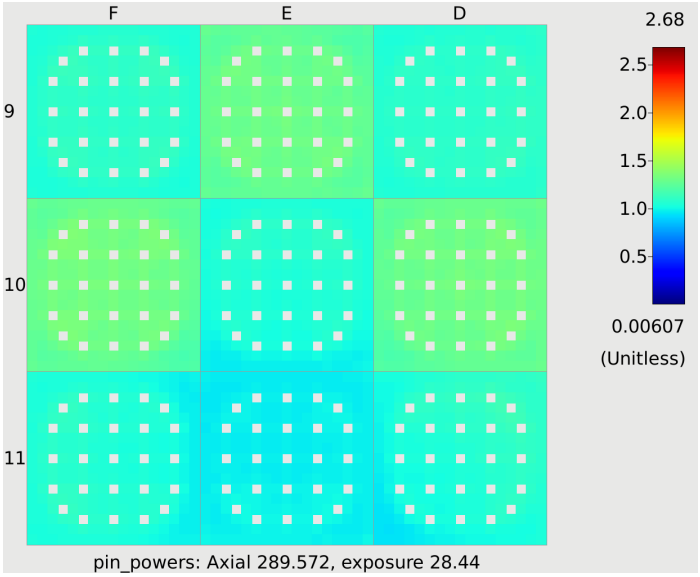

Figure *70*. Radial power distribution in the high-burnup core subregion at end-of-cycle.

For the benchmark with TRACE, both the CTF and TRACE models used one flow channel per assembly (9 in total). For each assembly, three pins were modeled: one pin to represent the highest power pin in the assembly, a second one to represent the rest of the fuel pins (a multiplier of 263 is used for the average pin), and a third pin to represent the guide tubes (a multiplier of 25 is used for the guide tube pin). The axial power distribution of the hot pin was taken directly from the VERA-predicted power distribution for the pin that has the highest integral power factor value. The remainder of the pins were averaged together for each level of the model to obtain one single average axial power factor distribution. Note that guide tubes were also modeled in the CTF and TRACE models. The flow channels were connected by lateral connections between all channels, which have a width equal to the assembly pitch of 21.5 cm. In the CTF model, the gap length was set to 12.6 mm. The pin-resolved model set the unique axial power factor distribution for every pin in the subregion and also included the guide tubes in the model.

Based on the results of the FEBA analysis, which indicate that a smaller timestep size was needed for resolved cases, a base maximum timestep size of 1e-4 s was used for the preliminary analysis. However, to further test the impact of timestep size, the maximum allowable timestep size was cut to 5e-5 s for an additional run. Furthermore, to test the impact of computer system, the cases were run on two high-performance computing systems: the Idaho National Laboratory (INL) Sawtooth cluster, and the INL Lemhi cluster. **Figure** 71 shows the summary of these simulations using box plots. There are 9 plots in the figure, one for each assembly, and the plots are organized as the assemblies appeared in **Figure** 70. Each plot shows four boxes: one for the 1e-4 s timestep case on Sawtooth (light orange), one for the 5e-5 s timestep case on Sawtooth (dark orange), one for the 1e-4 s timestep case on Lemhi (light green), and one for the 5e-5 s timestep case on Lemhi (dark green). The spread of the colored box encapsulates 50% of the maximum PCT values, and the bottom and top bars denote 1.5 times this spread. Any points that appear outside of the bars represent the outlier pins that are a significant distance from the inner quartile data. A few observations can be made from this figure:

- The maximum PCT of the low-burnup assemblies (E-9, F-10, and D-10) are always higher than the high burnup ones, which operate at lower power
- Both the median and the spread of the data are fairly consistent whether the case was run on Sawtooth or Lemhi
- The maximum PCT of the refined timestep case is noticeably higher for both machines and all assemblies, indicating that a more refined timestep is needed

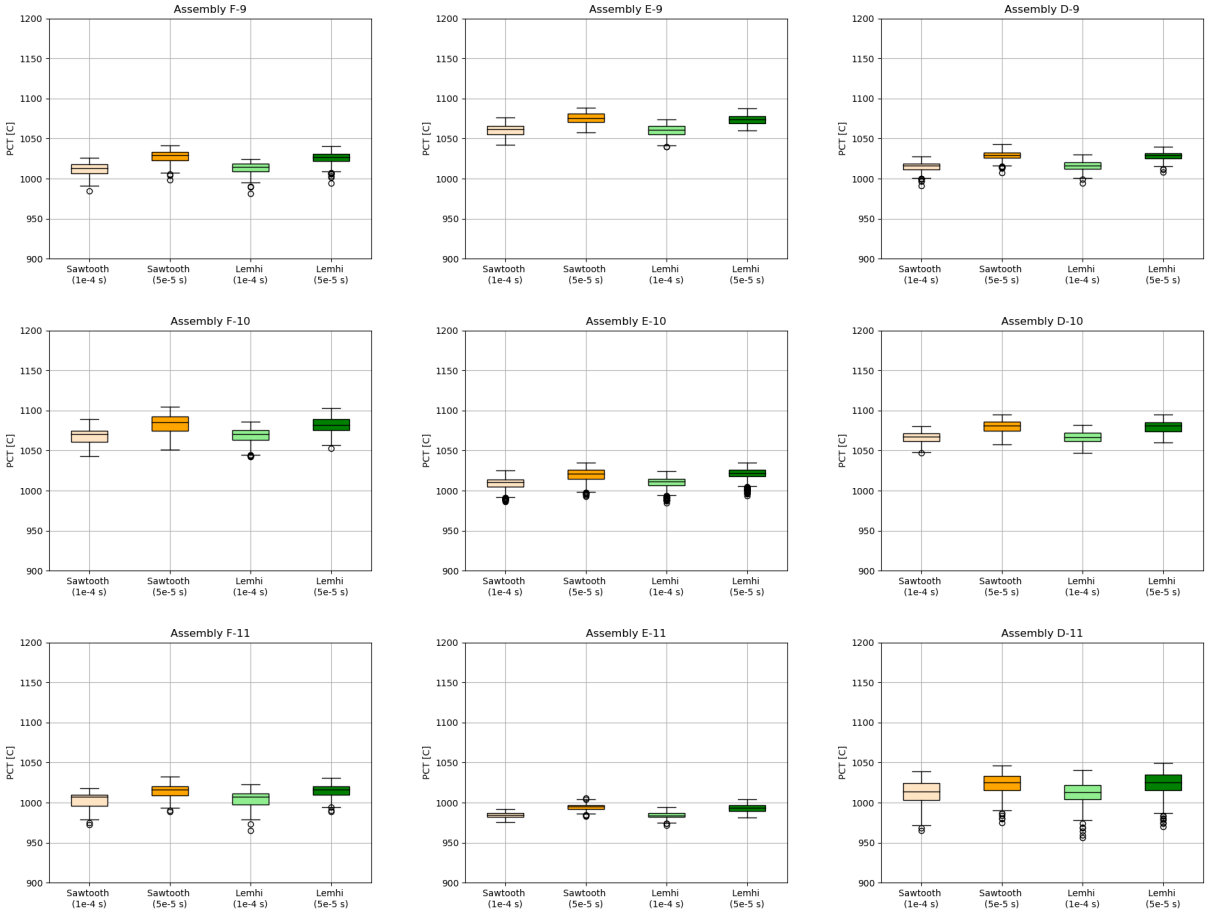

Figure *71*. Box plot indicating the spread of maximum PCT on Sawtooth vs. Lemhi and using a maximum timestep size of 1e-4 vs. 5e-5 s. One plot is shown for each assembly in the subregion.

The runtimes for the Sawtooth and Lemhi pin-resolved subregion cases are summarized in **Table** 14. The table gives the total walltime, in hours, to complete 200 seconds of the reflood transient. Note that these wall time values were extrapolated based on how far into the transient the job reached before being killed by the HPC walltime limit. Also, these jobs use 16 processors per assembly, or 144 processors in total for a single simulation. Modeling a full 193 assembly core at pin-cell resolution would require 3,088 processors, and it is anticipated that the runtimes would be some amount higher because of increased MPI overhead of the larger model. The maximum PCT for this transient occurs at about 105 s, and quench occurs at about 220 s. It has been observed in the FEBA tests that after all rods quench, the code tends to speed up significantly, indicating that it may be worthwhile profiling CTF for reflood conditions to check for performance bottlenecks in the post-CHF heat transfer modeling package. Furthermore, if the timestep requirement can be relaxed with numerical improvements, then the runtime of the code can be reduced further. Running with a 1e-4 s maximum timestep size takes about 30 h to run the first 200 s of the transient on Sawtooth.

Table *14*. CTF walltime requirement to run 200 s reflood transient in resolved subregion model on INL HPC systems using different maximum timestep sizes. Each model used 16 processors per assembly.

	dt=1e-4 s	dt=5e-5 s
Lemhi	69.2 hr	120.0 h
Sawtooth	30.2 hr	66.0 h

Figure 72 through

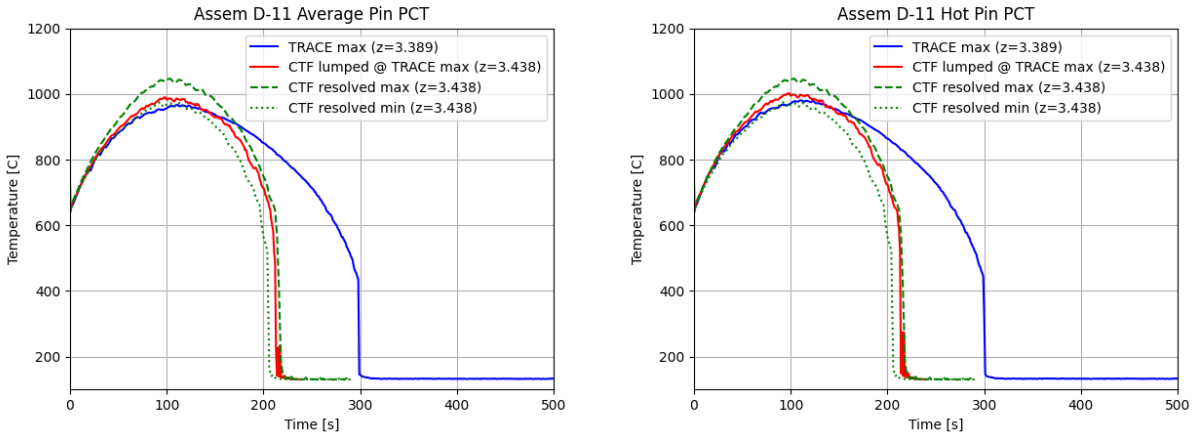

Figure ***80*** show the PCT behavior of the lumped and resolved CTF models, as well as the TRACE model. Note that because the previous results indicate that a 5e-5 s timestep size is needed, that is what was used for both the resolved and lumped CTF cases shown in these results. Each figure provides the average pin PCT behavior (left subfigure), the hot pin PCT behavior (right subfigure) for the lumped CTF model and the TRACE model for one of the assemblies in the subregion. The CTF lumped results are shown with the red line, and the TRACE model is shown with the blue line. The TRACE results are shown for the axial level where maximum PCT occurs, and the CTF lumped results are shown for the nearest axial location to the TRACE location, which is not necessarily the location of maximum PCT in the CTF model. Two dashed green lines are used to show the spread of the PCT behavior for all pins in each assembly, which are obtained from the pin-resolved CTF model. The long-dashed green line shows the behavior of the pin that achieves maximum PCT. The dotted line shows the behavior of the pin that achieves the minimum PCT for the same axial level where the maximum PCT was encountered. Note that the pin-resolved results are shown for the maximum PCT in the resolved model. This axial location happens to coincide with the axial level where PCT occurs in TRACE for every assembly. Also note that the resolved results do not change between the average and hot-pin subfigures.

The main takeaways from this collection of results are as follows

1. The maximum PCT of the CTF lumped models are generally consistent with the TRACE values.
2. Both the CTF lumped and pin-resolved models always have a faster quench time than TRACE, which sometimes occurs as much as 75 s earlier. **Figure** 66 shows that CTF and TRACE predicted very similar quench times for the 150 kJ/kg case for the top of the bundle. This case has an inlet enthalpy of 222 kJ/kg, so it was anticipated that the results would be closer than observed here; however, the case that was run for **Figure** 66 used the larger diameter FEBA rod geometry which also has no gap conductance model, so it is believed that the larger quenching discrepancy may partly be caused by the pin geometry difference. However, it was also shown during the FEBA validation exercise that CTF always quenches earlier than experimental results and that cause is likely the DFFB heat transfer model resulting in unrealistically high heat transfer behavior.
3. There is not a significant difference in the quenching behavior between the average and hot pins for a given assembly. Note that the difference in power is only about 20% between average and hot pins.
4. The quenching time of the lumped and resolved models are generally in good agreement, with the lumped model quench time usually falling between the minimum and maximum PCT quench

time in the resolved model. The bottom row of high-burnup assemblies shows the lumped model quenching slightly earlier than the lowest PCT pin in the resolved model.

5. The resolved model predicts a maximum PCT that is higher than the lumped CTF and TRACE results by as much as 50 °C indicating that there may be localized TH effects occurring in the subchannels near these pins that is significantly different than that of the average channel representing the assembly. This effect is addressed further below.

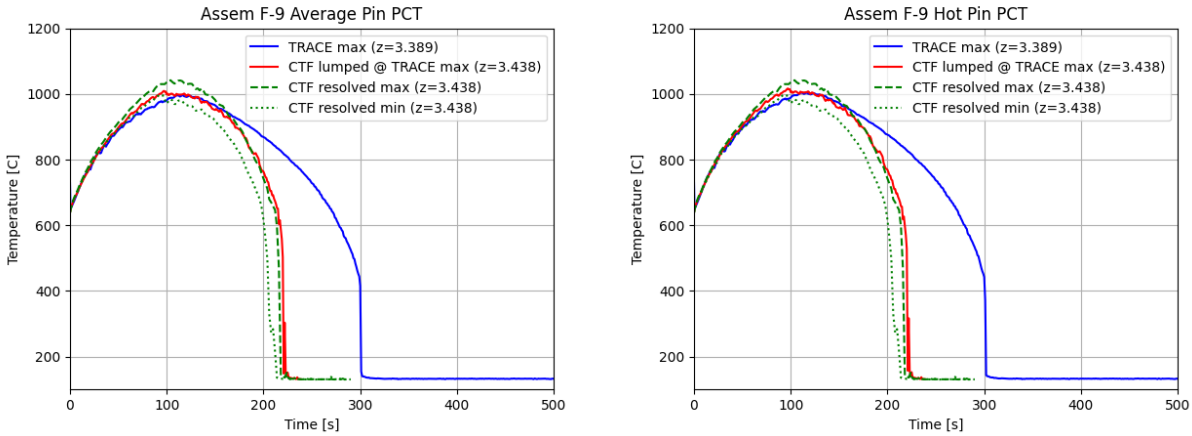

Figure *72*. Assembly F-9 (high burnup) average pin (left) and hot pin (right) PCT behavior.

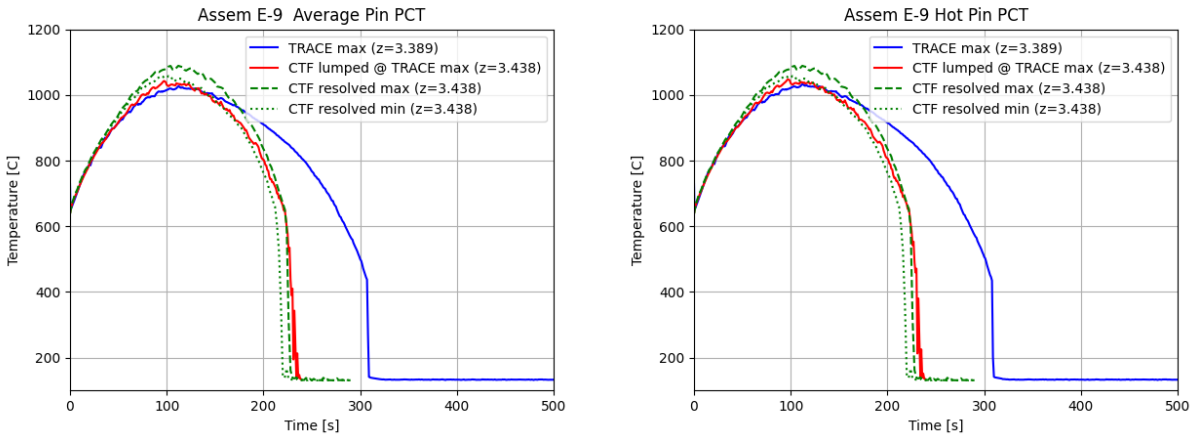

Figure *73*. Assembly E-9 (low burnup) average pin (left) and hot pin (right) PCT behavior.

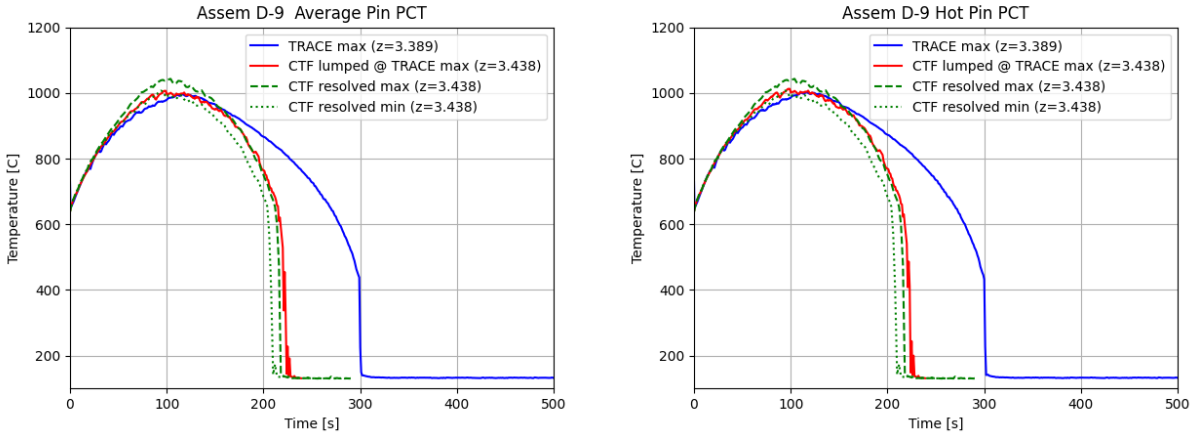

Figure *74*. Assembly D-9 (high burnup) average pin (left) and hot pin (right) PCT behavior.

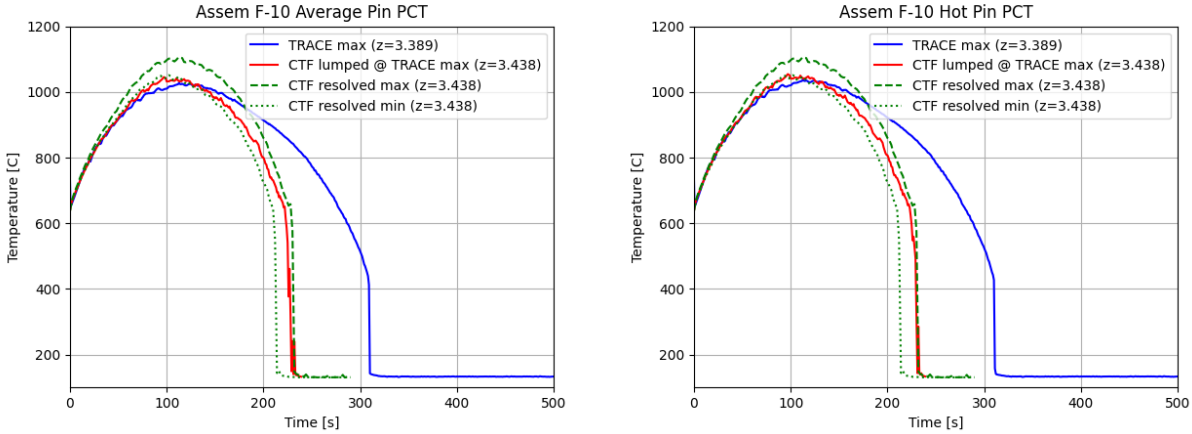

Figure *75*. Assembly F-10 (low burnup) average pin (left) and hot pin (right) PCT behavior.

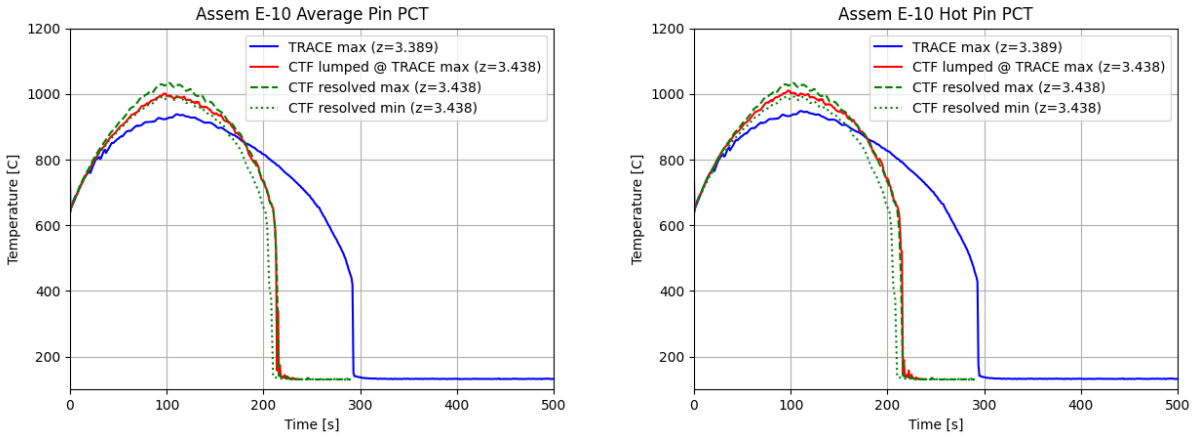

Figure *76*. Assembly E-10 (high burnup) average pin (left) and hot pin (right) PCT behavior.

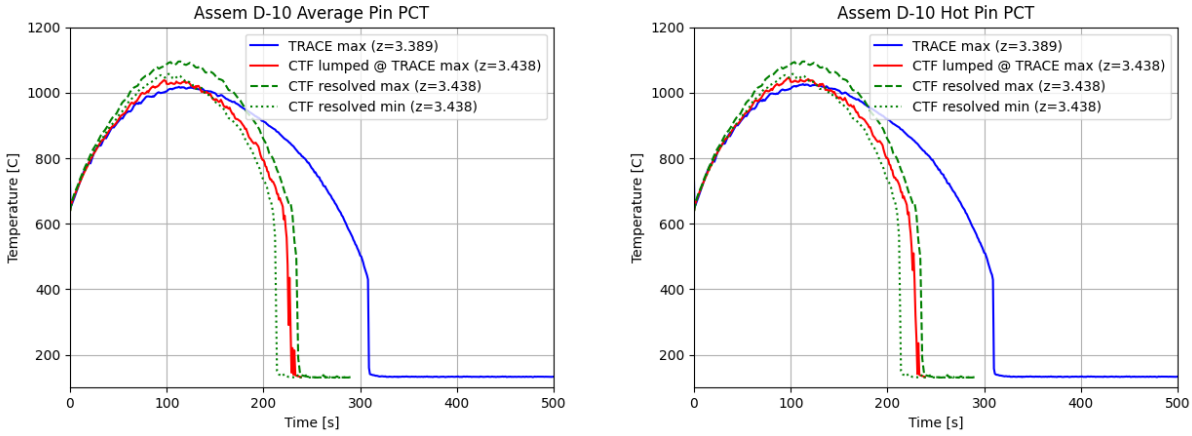

Figure 77. Assembly D-10 (low burnup) average pin (left) and hot pin (right) PCT behavior.

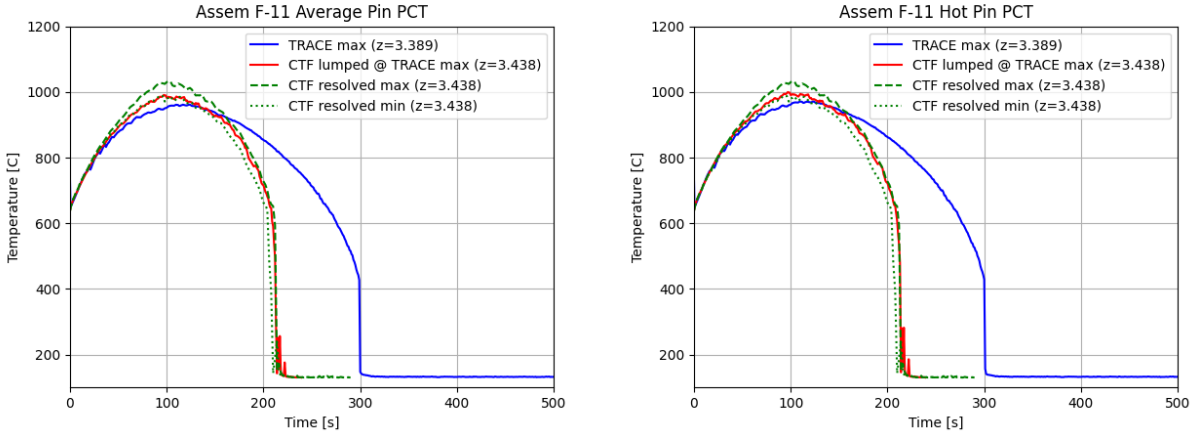

Figure 78. Assembly F-11 (high burnup) average pin (left) and hot pin (right) PCT behavior.

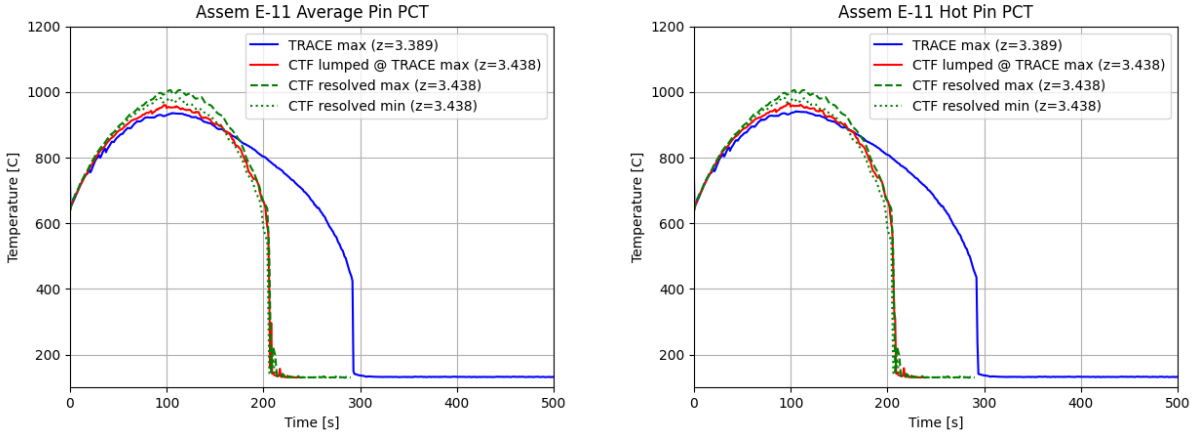

Figure 79. Assembly E-11 (high burnup) average pin (left) and hot pin (right) PCT behavior.

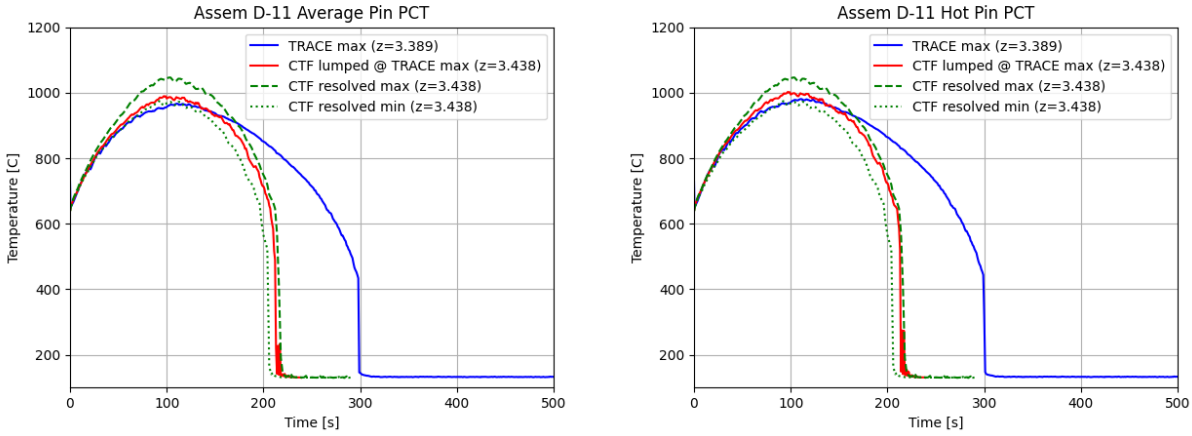

Figure *80*. Assembly D-11 (high burnup) average pin (left) and hot pin (right) PCT behavior.

Looking further into the differences between the CTF lumped and resolved cases, the maximum PCT of each pin is plotted in a histogram for each assembly in the model. This is shown in **Figure** 81, with the lumped CTF results shown as red and black vertical lines for the hot and average pins, respectively. For most of the assemblies, the lumped pin PCT values tend to the lower end of the range of PCTs encountered in the resolved case, which indicates a strong local TH effect on the results. There is a significant discrepancy for the high-burnup assembly in the E-11 location, which currently has no explanation.

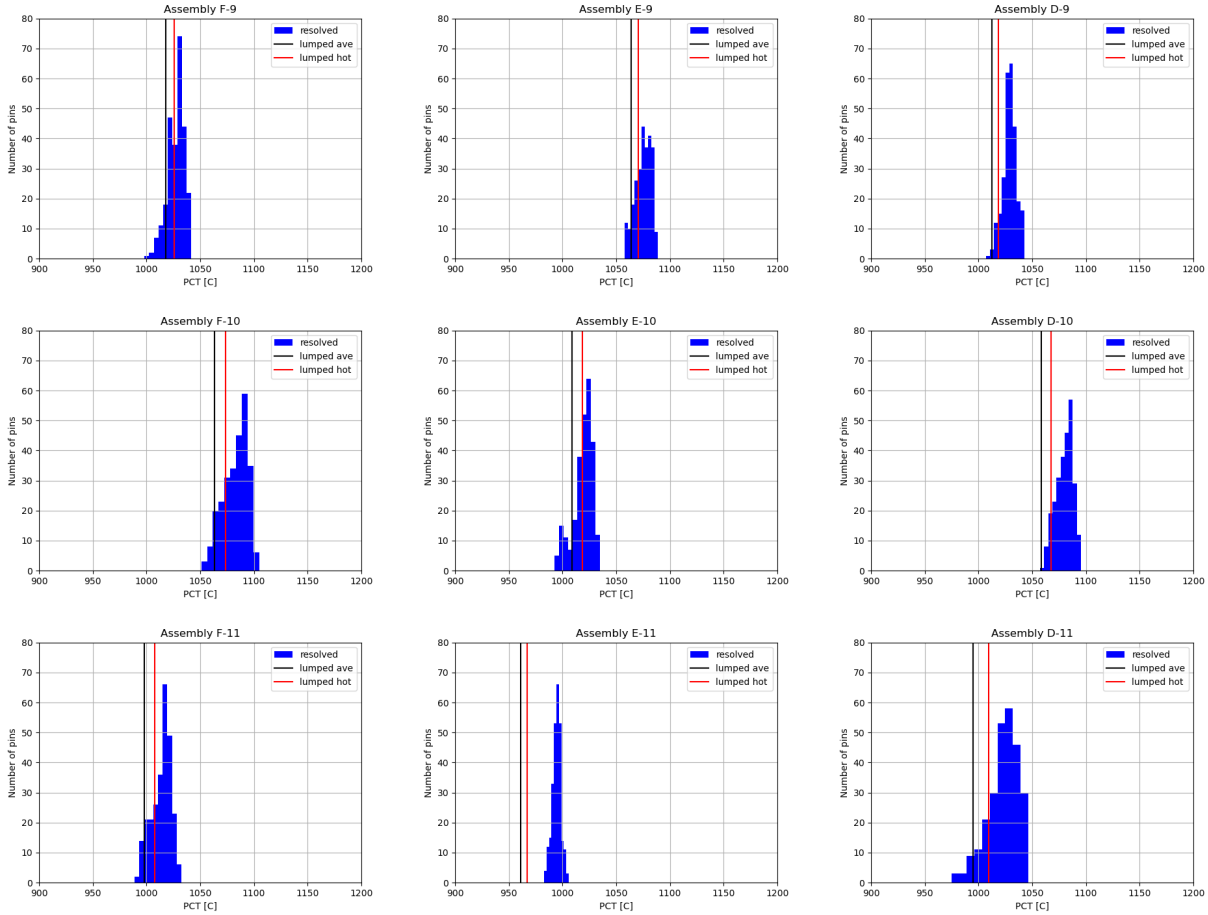

Figure *81*. Distribution of maximum PCT in each assembly in the subregion model (blue) compared to the lumped CTF model hot and average pin values.

To further investigate the behavior of the pin-resolved model, **Figure** 82 shows the cross section of the entire subregion at 343.8 mm axial location. This snapshot was taken at 106 s into the transient, which corresponds to the time when maximum PCT is encountered in the model. The figure shows the maximum PCT of each pin at that axial location and time. The temperature range has been scaled between 950 °C and 1050 °C to better illustrate the radial gradient at PCT. A few observations can be made from this figure:

1. The low-burnup assemblies have the highest power and therefore have much higher PCT at this point in the transient when compared to the high-burnup assemblies.
2. The high-burnup assembly PCT behavior generally follows the pin power distribution behavior (which will be shown later); however, it can also be seen that PCT is also higher at the boundaries of the assemblies which are adjacent to the higher power, hotter low-burnup assemblies.
3. The low-burnup assemblies begin to quench sooner in the regions adjacent to the cooler, high-burnup assemblies, indicating that mixing is causing the high enthalpy vapor to migrate into the adjacent assemblies and bring droplets in from the high-burnup assemblies.

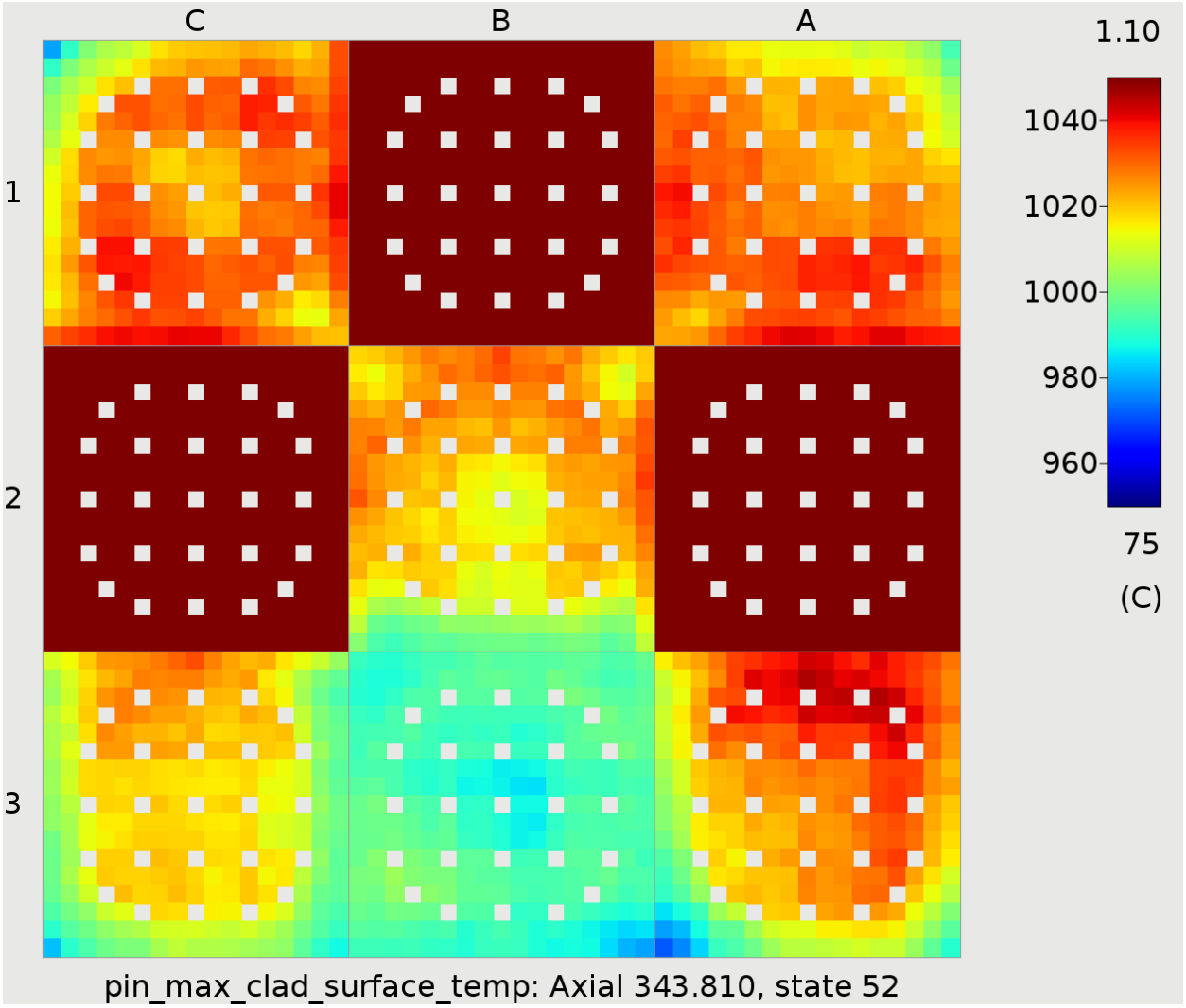

Figure *82*. Radial PCT distribution in pin-resolved subregion model at axial location where PCT occurs.

To further describe the behavior of the pin-resolved model, **Figure** 83 through **Figure** 88 show the PCT distribution (left subfigure) and radial power distribution (right subfigure) for each high-burnup assembly in the subregion. Note that the radial power distribution is shown for the level where peak power factor occurs and not necessarily the axial level where PCT occurs. The hot pin is identified in both subfigures. In the PCT plot, a dark green box surrounds the hot pin and in the power plot, and a red box surrounds the hot rod. In the PCT plot, a black box surrounds the maximum PCT in that assembly. The PCT location does not always coincide with the hot pin location. For some of the high-burnup assemblies, the PCT location occurs on the boundary of the assembly when that assembly is adjacent to a higher power low-burnup assembly. **Table** 15 provides a summary of the PCT in the high-power pin vs. the actual PCT in each assembly in the resolved subregion model. Assemblies E-10 and F-11 experience the largest difference of 6 K between high power pin and assembly PCT.

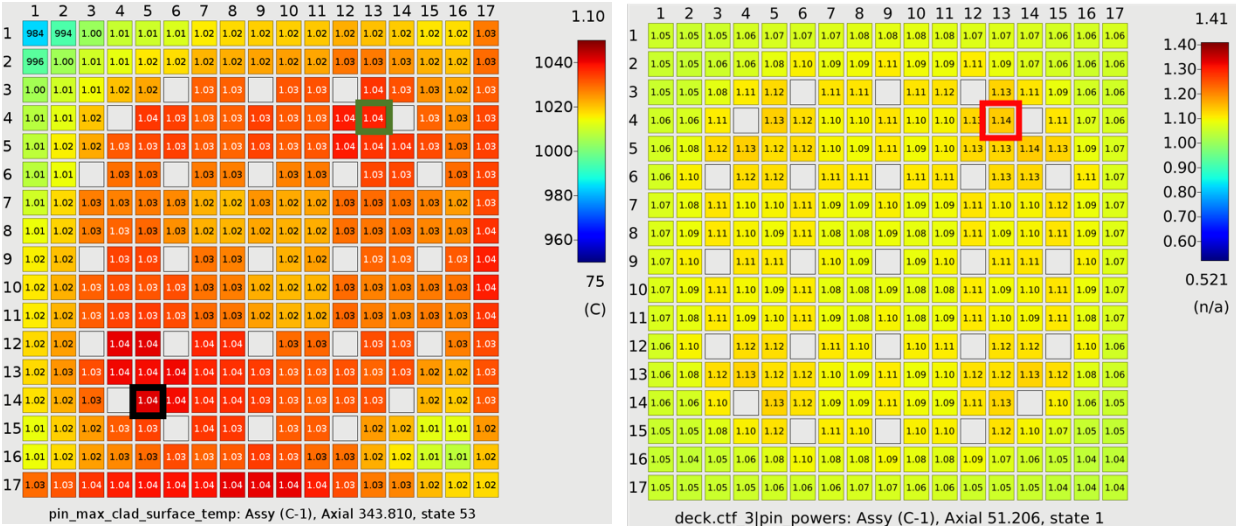

Figure *83*. Assembly F-9 radial PCT distribution in pin-resolved model at the axial location where PCT occurs (left) and radial power distribution with peak power factor highlighted (right). The red/green boxes indicate the peak power pin and the black box indicates the location of PCT.

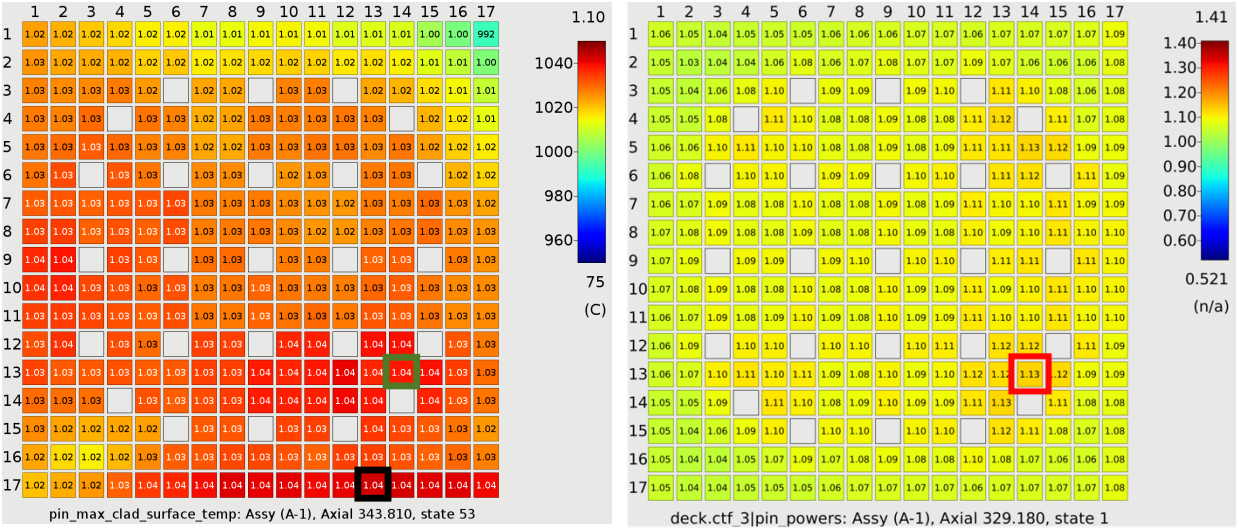

Figure *84*. Assembly D-9 radial PCT distribution in pin-resolved model at the axial location where PCT occurs (left) and radial power distribution (right). The red/green boxes indicate the peak power pin and the black box indicates the location of PCT.

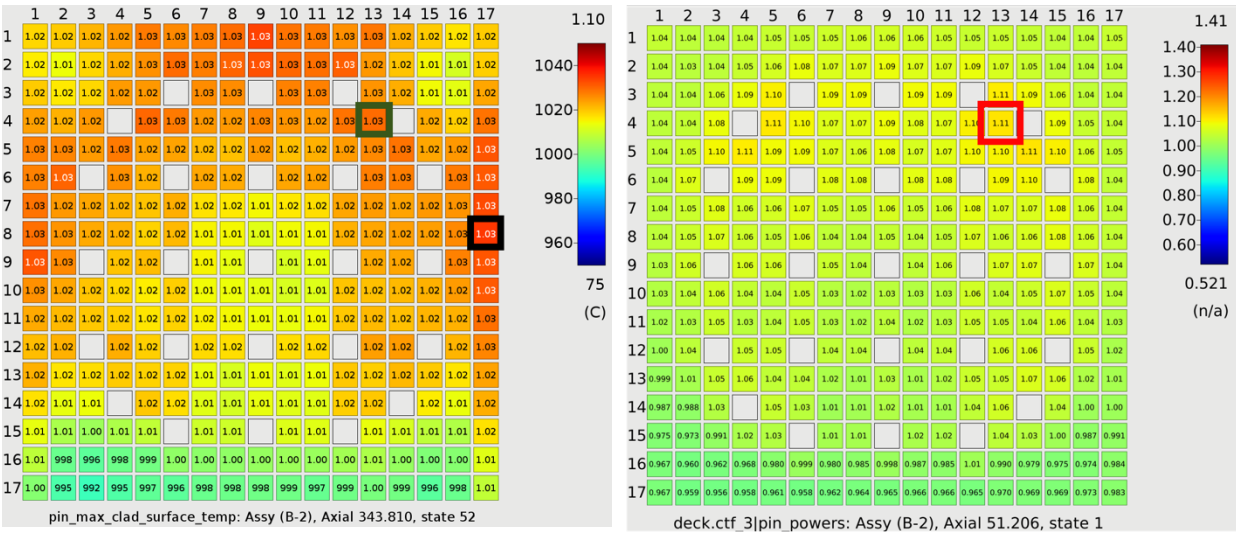

Figure *85*. Assembly E-10 radial PCT distribution in pin-resolved model at the axial location where PCT occurs (left) and radial power distribution (right). The red/green boxes indicate the peak power pin and the black box indicates the location of PCT.

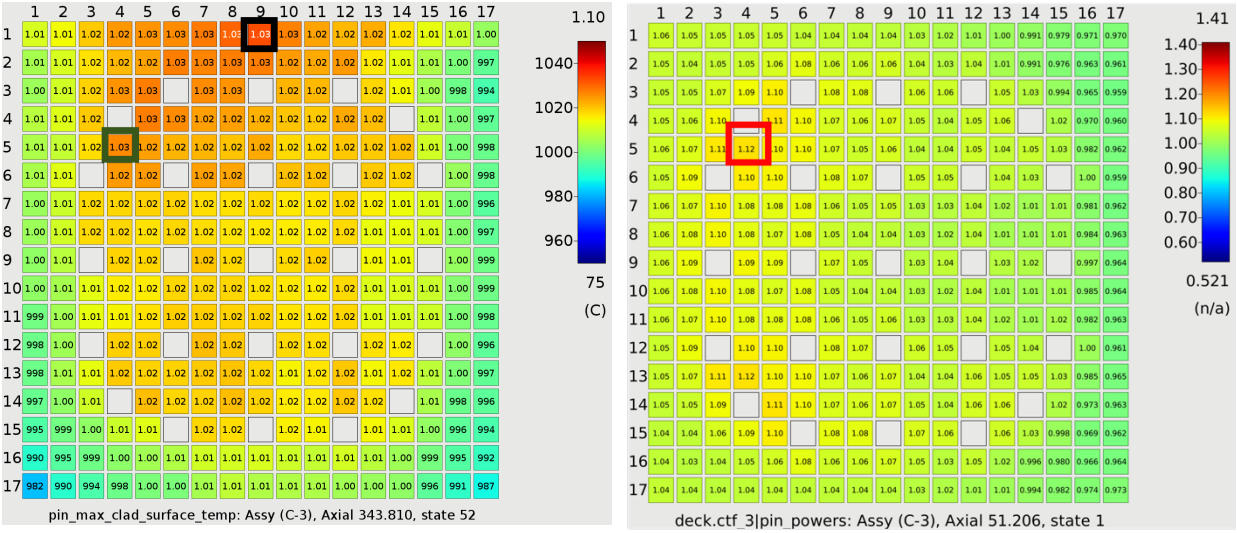

Figure *86*. Assembly F-11 radial PCT distribution in pin-resolved model at the axial location where PCT occurs (left) and radial power distribution (right). The red/green boxes indicate the peak power pin and the black box indicates the location of PCT.

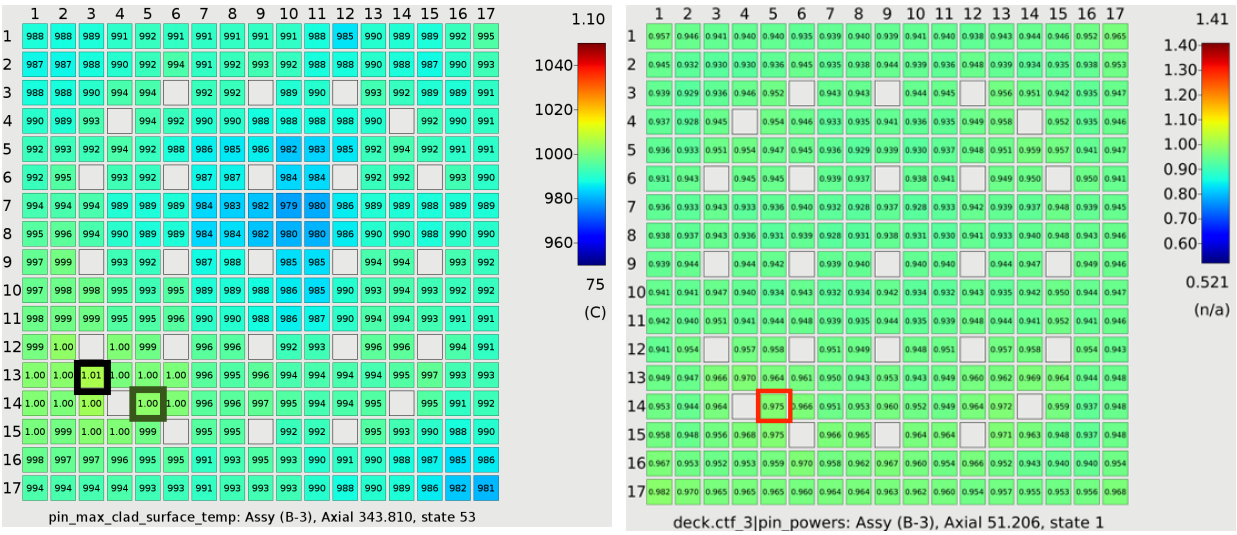

Figure *87*. Assembly E-11 radial PCT distribution in pin-resolved model at the axial location where PCT occurs (left) and radial power distribution (right). The red/green boxes indicate the peak power pin and the black box indicates the location of PCT.

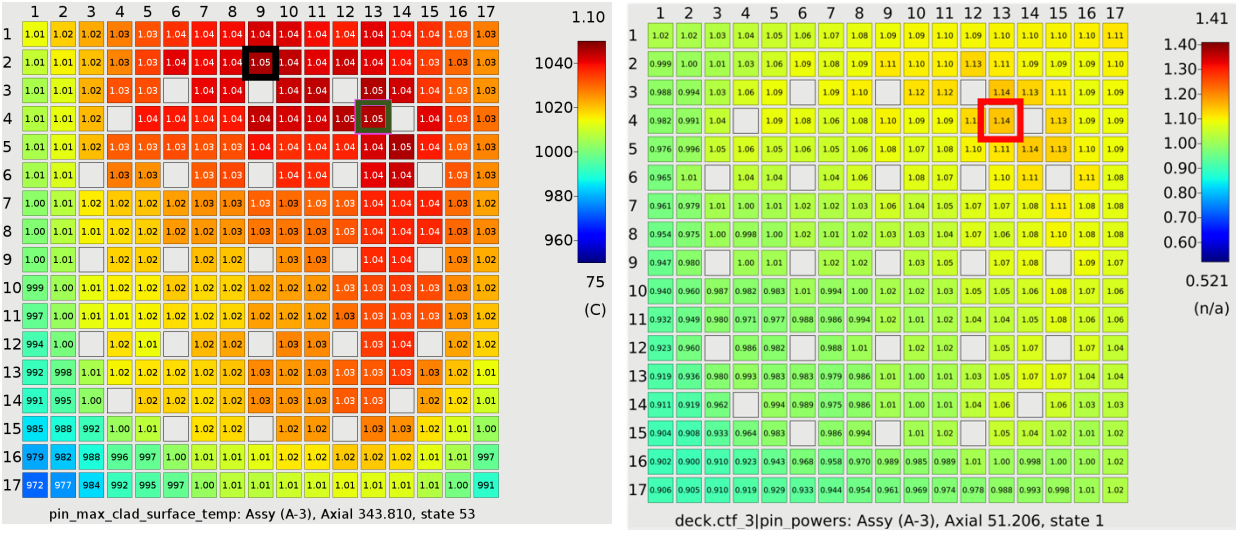

Figure *88*. Assembly D-11 radial PCT distribution in pin-resolved model at the axial location where PCT occurs (left) and radial power distribution (right). The red/green boxes indicate the peak power pin and the black box indicates the location of PCT.

Table *15*. Summary of PCT value in the high-power pin and actual PCT in the assembly for the pin-resolved subregion model

Assembly	PCT in hot pin [°C]	Maximum PCT [°C]	Difference [°C]
F-9	1,037	1,042	5
D-9	1,039	1,043	4
E-10	1,029	1,035	6
F-11	1,026	1,032	6
E-11	1,002	1,006	4
D-11	1,045	1,046	1

Because of the perceived impact of the neighbor assemblies on high-burnup assembly PCT behavior, additional pin-resolved CTF cases were run in which the 9 assemblies were kept separate from one another, so the assemblies were not connected, and there was no cross-flow. These were actually 9 separate models that were run in CTF, one for each assembly in the subregion model. The subchannels located between the assemblies in the connected subregion model were divided in halves or in quarters to preserve the velocity behavior. All other modeling parameters, including maximum timestep size, were kept consistent with the connected subregion model.

Figure 89 shows the maximum PCT distribution for each of the 9 assemblies. The normal connected case is shown in blue, and the single-assembly cases are shown using a translucent orange. Additionally, vertical dashed orange and blue lines are used to denote the median maximum PCT value for the single and connected models, respectively. The figure indicates a clear tendency for PCT to drop for some of the high burnup assemblies (F-9, D-9, and E-11) when the connections to the neighboring low-burnup assemblies are eliminated, which agrees with previous observations that energy seems to be entering the high-burnup assemblies from low-burnup ones. However, this trend is only mildly observed for the center high-burnup assembly, which has the most connections to low-burnup assemblies out of all other high-burnup assemblies. It is also observed that spread of the data is generally smaller in the assemblies when they are connected to other assemblies, potentially because mixing leads to a more uniform radial solution. When separated from the high-burnup assemblies, the higher-powered low-burnup assembly maximum PCT does generally increase over the connected case, but it also experiences much lower PCT values. The median values are typically close between connected and unconnected low-burnup assemblies.

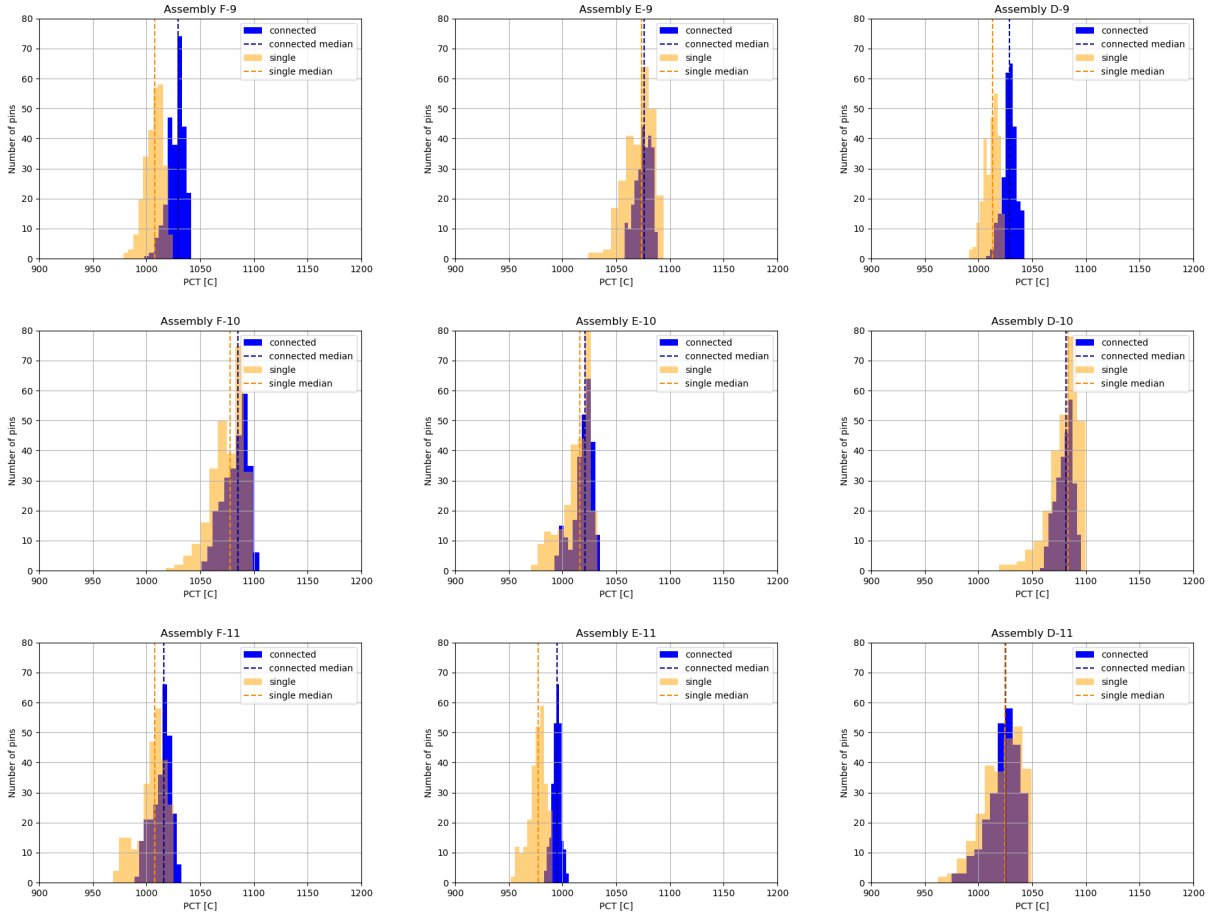

Figure *89*. **Comparison of distribution of maximum PCT in the CTF subregion model and individual CTF models of each separate assembly.**

Figure 90 through **Figure** 95 present a comparison between the PCT distribution in the connected and unconnected models. Each figure presents the connected model (cross-flow between assemblies) on the left and the single-assembly model on the right. The increased PCT of the connected model is evident, as is the shift in PCT location to the boundaries. In the single assembly results, the PCT generally follows the high-power pin location.

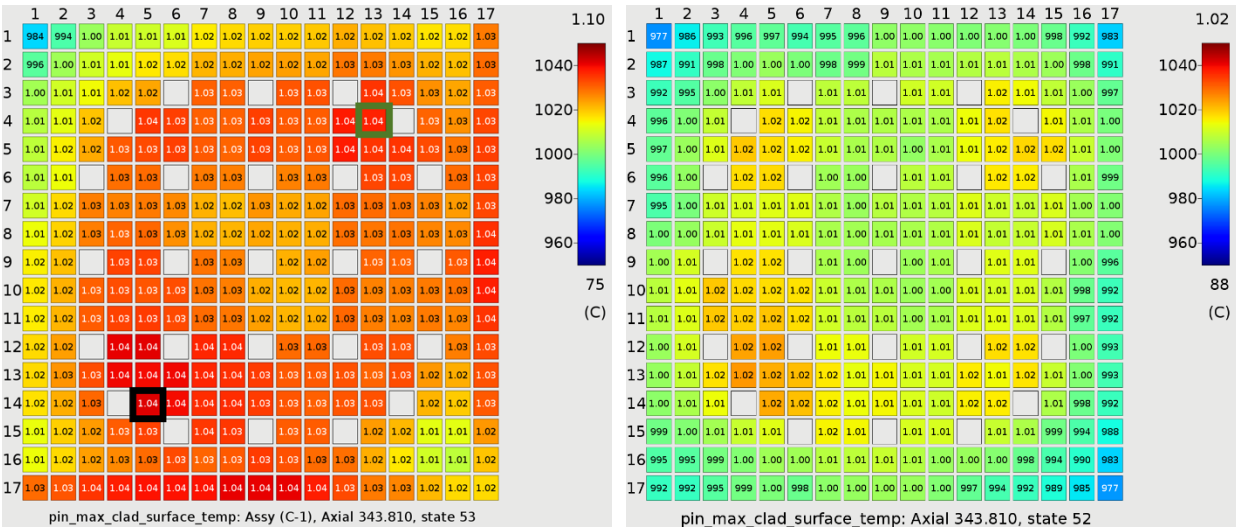

Figure *90*. Assembly F-9 radial PCT distribution in connected pin-resolved model (left) and radial PCT distribution in single assembly model (right). The black box denotes the maximum PCT location, and the green box denotes the high-power pin.

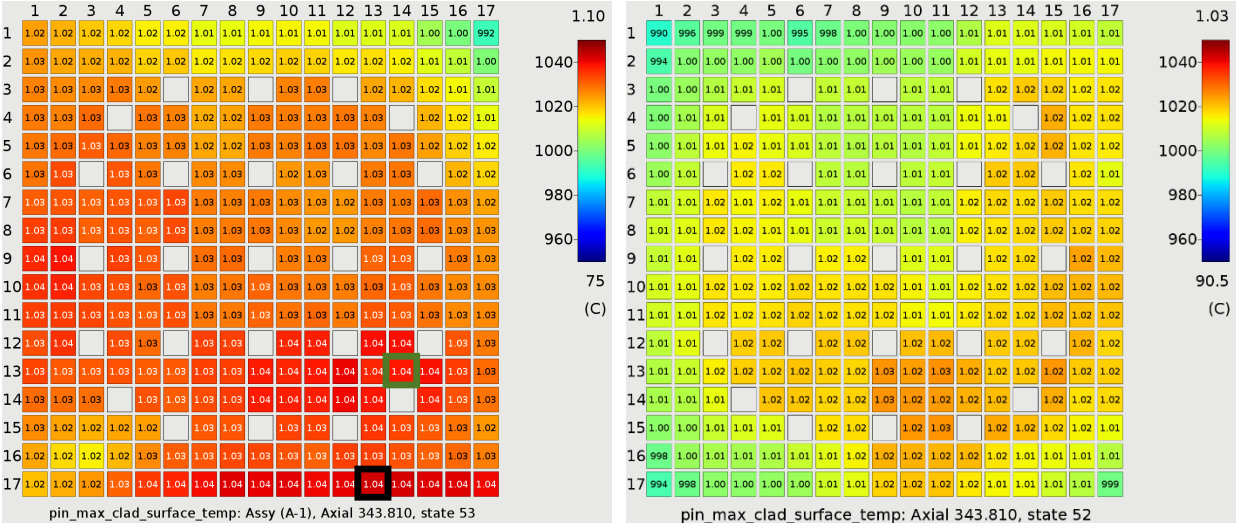

Figure *91*. Assembly D-9 radial PCT distribution in connected pin-resolved model (left) and radial PCT distribution in single assembly model (right). The black box denotes the maximum PCT location, and the green box denotes the high-power pin.

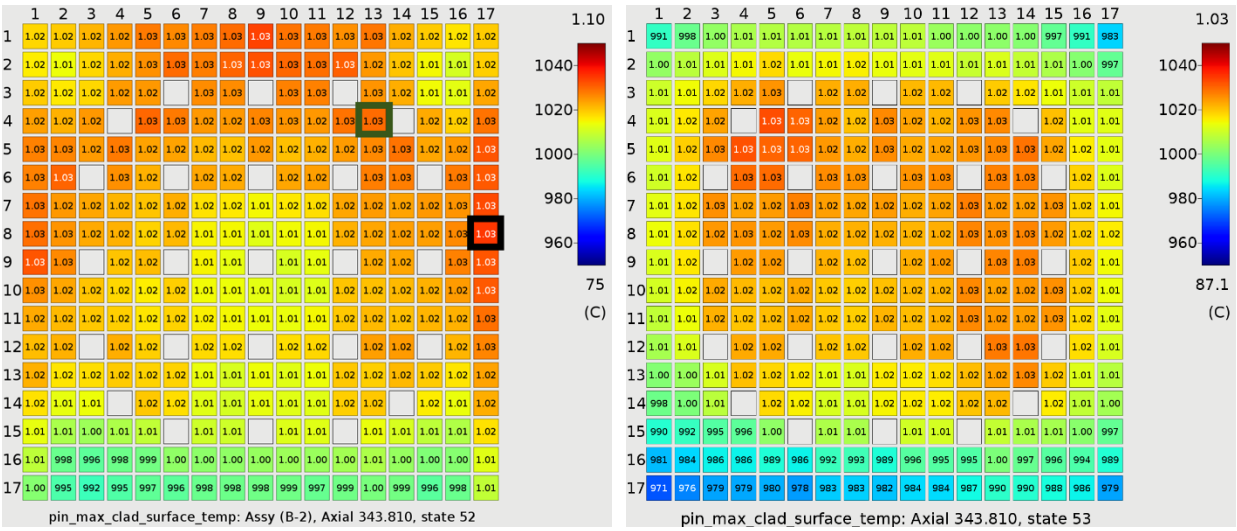

Figure *92*. Assembly E-10 radial PCT distribution in connected pin-resolved model (left) and radial PCT distribution in single assembly model (right). The black box denotes the maximum PCT location, and the green box denotes the high-power pin.

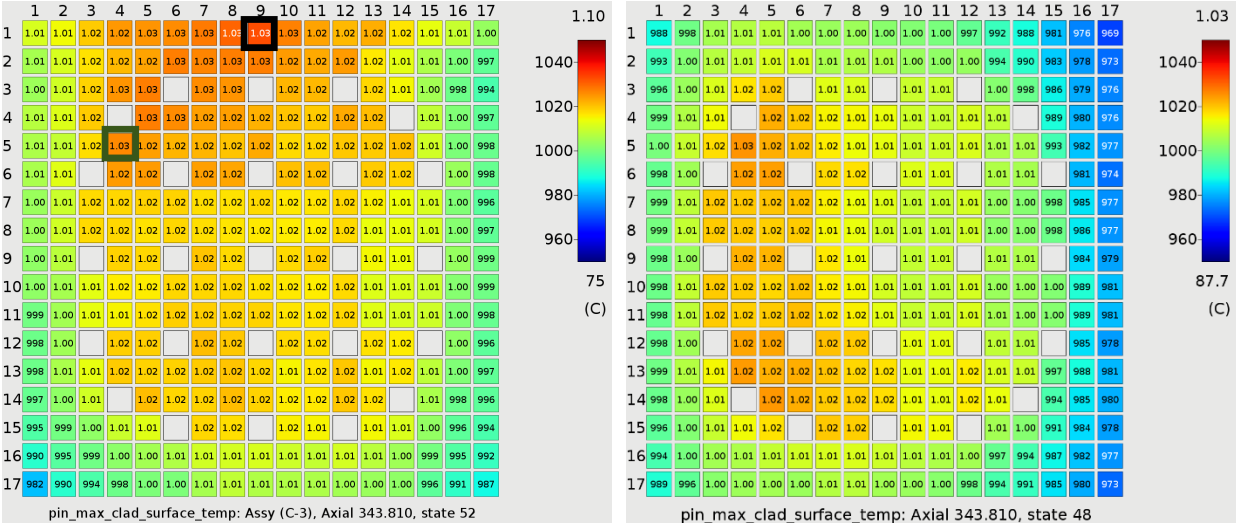

Figure *93*. Assembly F-11 radial PCT distribution in connected pin-resolved model (left) and radial PCT distribution in single assembly model (right). The black box denotes the maximum PCT location, and the green box denotes the high-power pin.

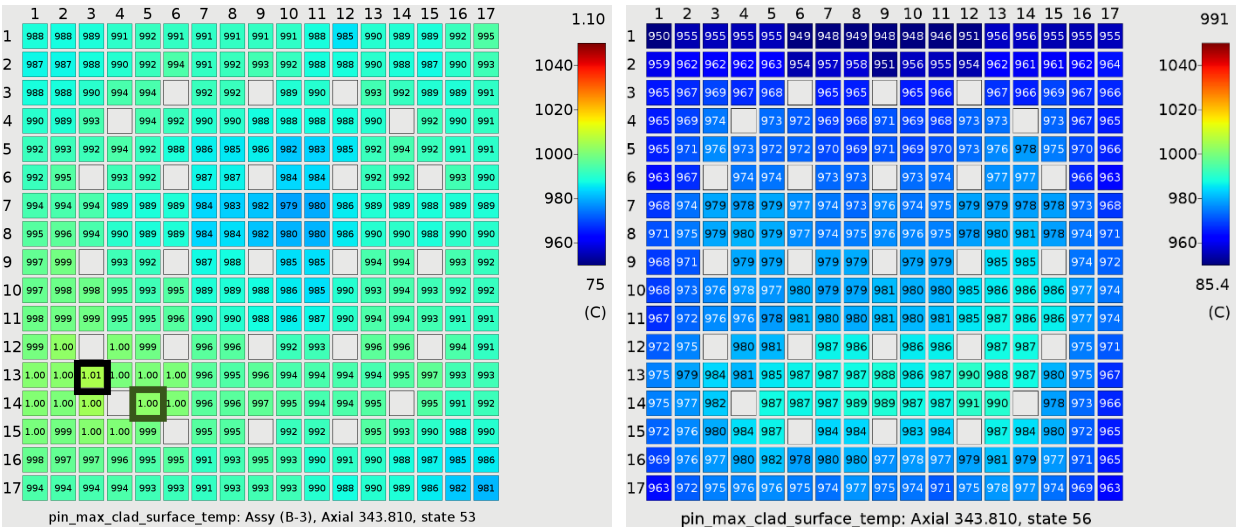

Figure *94*. Assembly E-11 radial PCT distribution in connected pin-resolved model (left) and radial PCT distribution in single assembly model (right). The black box denotes the maximum PCT location, and the green box denotes the high-power pin.

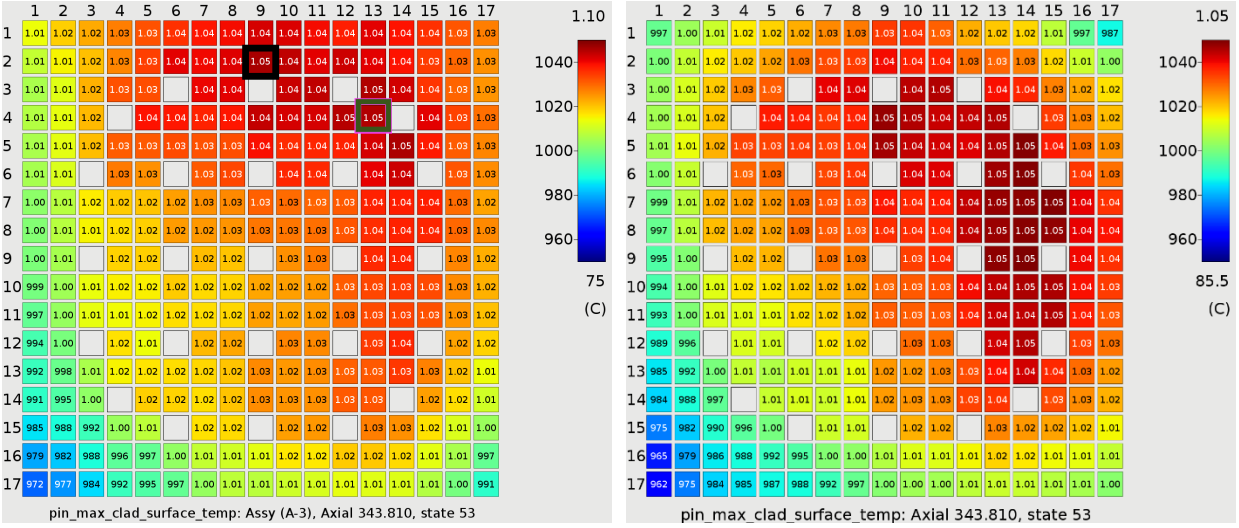

Figure *95*. Assembly D-11 radial PCT distribution in connected pin-resolved model (left) and radial PCT distribution in single assembly model (right). The black box denotes the maximum PCT location, and the green box denotes the high-power pin.

5. TRACE FULL CORE ANALYSES

In FY22, a full-system TRACE model was developed and applied to LBLOCA analysis in a high burnup core. This section details the numerous modifications and improvements made to this model to improve its accuracy and align the model with recommended usage and best practices. Many of these improvements address specific feedback provided by the NRC.

As shown in this section, the updated model showed better agreement with published LBLOCA benchmark results in terms of peak cladding and time of quench. The new model also proved more numerically stable and robust, with more predictable PCT trends and fewer case failures.

An additional goal of this work is to better understand the spatial dependence of TH phenomena in the core and vessel during LBLOCA and to explore the impact of spatial modeling fidelity on the LBLOCA fuel behavior. Although the impact of azimuthal core and vessel fidelity was found to be small, the radial core and vessel fidelity had a very large impact on the LBLOCA behavior. This suggests that spatial TH effects play an important role during LBLOCA and reinforces that higher fidelity modeling would be beneficial not only on a local subchannel/assembly level, but also on an overall core level.

5.1.1 Description of the FY22 TRACE LBLOCA Model

A detailed description of the previous TRACE LBLOCA model is given in the FY22 milestone report and the associated journal article (Capps, Hirschhorn, Wysocki, & Greenquist, 2022) (Greenquist, Wysocki, Hirschhorn, & Capps, 2023). A summary of the model is given here to provide context for the modeling changes discussed throughout the remainder of this section.

The starting point for the FY22 model was a legacy typical PWR model that is included in the TRACE code distribution. The model was based on the Zion nuclear power plant (NPP), a Westinghouse 4-loop reactor design. It was originally modeled in RELAP5 and then converted to TRACE.

The BEMUSE project (Reventos, Perez, Batet, & Pericas, 2008) was an international Organisation for Economic Co-operation and Development (OECD) modeling benchmark exercise which provided a set of model specifications for a selected PWR system and compared the results contributed by the thirteen international participants using a variety of different reactor systems thermal hydraulic codes. The benchmark specifications were based on a similar Zion NPP model as the legacy model described above. However, the BEMUSE specifications included several significant modifications and improvements relative to the legacy model. A key accomplishment of the FY22 milestone effort was to take the available legacy model and introduce the BEMUSE-specified improvements into it to improve the accuracy and representativeness of the model predictions. The results for this improved model were compared against the published BEMUSE participants' results to ensure its adequacy. Then the improved model was adjusted to match the specific plant operating conditions, power distributions, and burnup distributions for the representative high-burnup 24-month cycle in VERA that was discussed in Section 4. The TRACE model was run under these conditions for 281 high-burnup fuel rods (greater than 62 GWD/MTU) to establish the range of cladding conditions expected for high-burnup fuel rods during LBLOCA.

A depiction of the core channel and rod grouping scheme used in the FY22 TRACE model is given in **Figure** 96. The model included three rod groups: a rod representing a single high-burnup rod of interest, a lumped rod representing the remainder of the fuel rods in that assembly, and a lumped rod representing the remainder of the core. Using this modeling scheme, 282 separate TRACE cases were run, one for each of the 281 selected high burnup rods, plus an additional case for the highest power rod in the core to use as a reference point. The actual location in the core represented by the rod and assembly of interest therefore changes from case to case. The axial-dependent power and burnup profiles were extracted from VERA and averaged as appropriate to represent the given rod and assembly in each case.

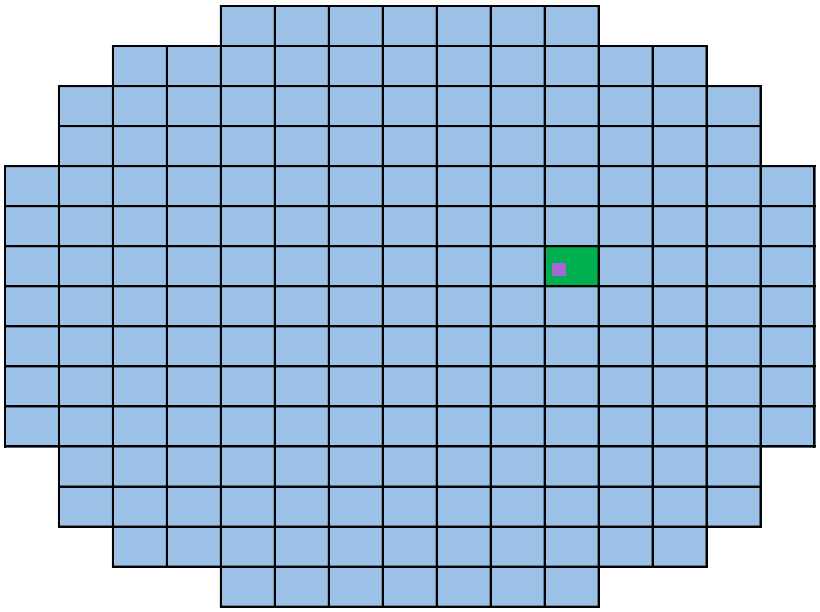

Number of Fuel Assemblies	Name	Number of Fuel Rods
192	Average Channel	39168
1	Assembly Surrounding the Rod of Interest	203
1 rod	Rod of Interest	1
193	TOTAL	39372

Figure *96*. TRACE core channel and rod grouping used in the current study (locations will vary depending on each case's rod of interest).

The primary system representation used in the FY22 TRACE model is depicted in **Figure** 97. Explicit modeling of the secondary side steam generator and various plant control systems and safety systems are included in the model, as well. The BEMUSE-specified improvements focused primarily on fuel rod modeling fidelity (fuel rod axial and radial discretization, and other fuel modeling assumptions), plant operating conditions, LOCA break assumptions, and reactor safety system configuration. Most of the thermal hydraulic flow configuration and geometric modeling approach was retained from the legacy model.

This includes the legacy modeling approach of representing the vessel flow path using a series of one-dimensional pipe components and side junction components. In total, approximately 30 pipe components and 100 side junction components (some but not all of which are depicted in **Figure** 97) were used for the downcomer, upper and lower plena, and core regions of the vessel. These side junctions were used to transport mass, energy, and momentum in the fluid in a lateral direction, across the upper and lower plena and between the three flow regions in the core.

Two discrete loops were modeled in the primary system in the FY22 model: a "broken loop" where the double guillotine break occurs, and a single solved "intact loop" which represents the three physical intact loops lumped together for modeling simplicity. Azimuthal dependency was crudely accounted for in the downcomer and plena by splitting these regions into a smaller lumped section representing one-quarter of these regions (connected to the single broken loop) and in a larger section representing the remaining three-quarters of these regions (connected to the lumped triple intact loop). These regions were connected to each other by side junctions as well to allow a coarse treatment of azimuthal transport.

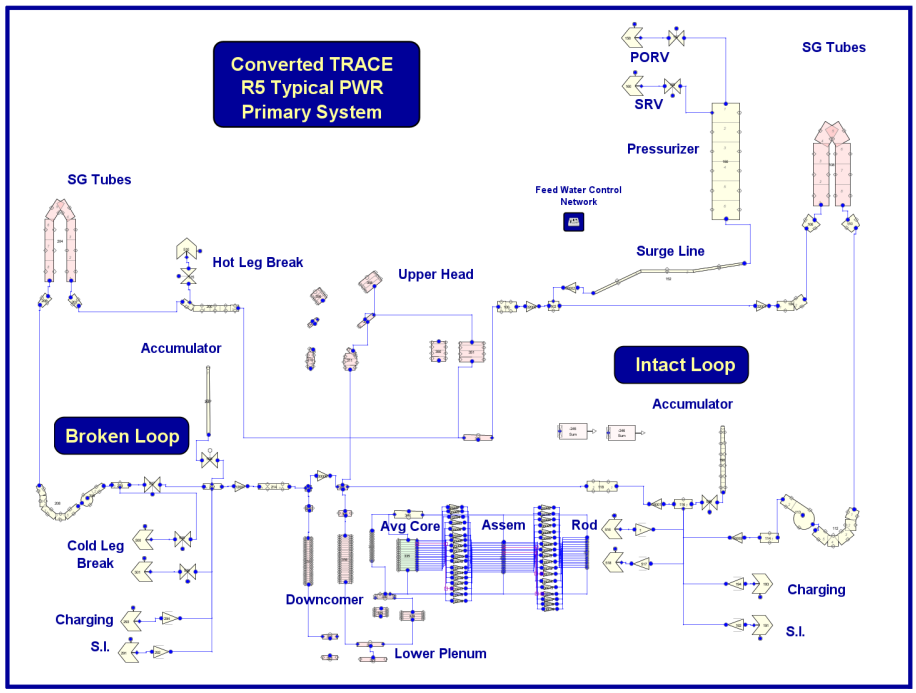

Figure 97. Visualization of the FY22 TRACE model with pipes and side junctions for the vessel.

5.2 FY23 Modeling Modifications

During a series of technical discussions between ORNL and NRC staff, several improvements to the TRACE model were recommended to better align the model with best practices and state of the art. These discussions were the main impetus for the FY23 efforts toward modifying and improving the TRACE high burnup LBLOCA model. The improvements achieved in the TRACE LBLOCA model in FY23 include the following:

- Update the latest available TRACE executable (version 5.0 Patch 7)
- Use vessel instead of pipes and side junctions
- Increase the radial modeling fidelity of the core, by employing two rings in the core and 8 azimuthal sectors
- Model each of the three intact loops in the plant explicitly instead of lumping the loops together
- Employ more realistic form loss factors in the vessel region
- Increase the fidelity of the fuel rod radial conduction solution
- Use realistic gap gas composition for high burnup

The implementation of these improvements and their impact on the predicted cladding behavior are presented in the following subsections. The analysis includes several sensitivity studies on modeling parameters such as nodalization and fuel rod modeling options to understand their impact on the PCT predictions.

5.2.1 Update to TRACE Version 5.0 Patch 7

The latest publicly released TRACE version available during the FY22 LOCA modeling efforts was TRACE Version 5.0 Patch 6. Since then, Version 5.0 Patch 7 has been released. Per the NRC's suggestions, all runs in the current report were performed with Version 5.0 Patch 7. The impact of code version on the original TRACE HB LOCA model from FY22 is shown in **Figure** 98.

Individual differences can be observed for specific cases, such as the highest power case (green line in **Figure** 98), as well as some outlier results, particularly with Patch 7. LOCA is a highly challenging problem from a physical and modeling perspective, where relatively small changes in input quantities and numerics can produce significant changes in results; therefore, a few outlier cases are not unexpected. As seen in later plots, as additional improvements were made to the model, the TRACE-predicted rod behavior became more reliable, and such outliers became much less common. Best-practice modeling improvements produced more numerically reliable and predictable behavior, providing greater confidence and reliability in the results.

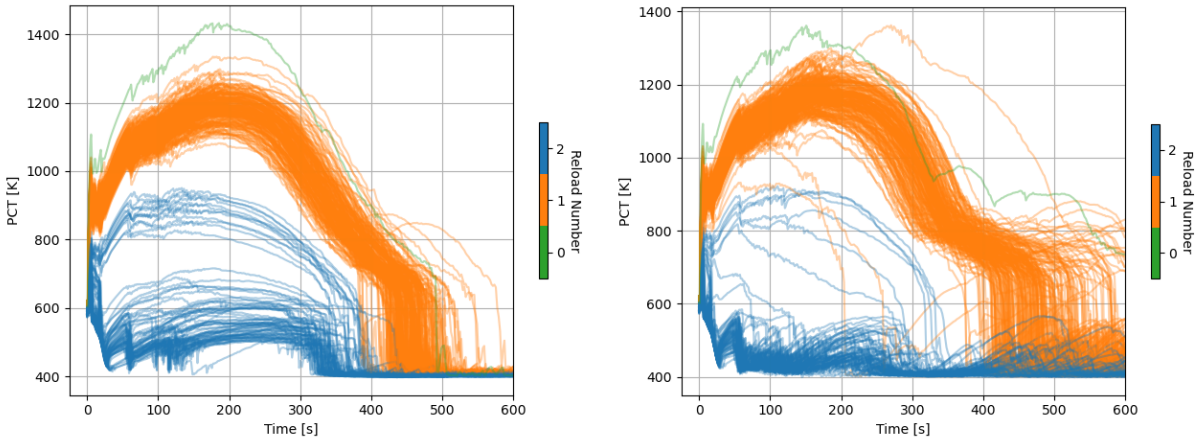

Figure *98*. **282-rod PCT results for the side junction model, with TRACE version 5.0 Patch 6 (left) and version 5.0 Patch 7 (right).**

5.2.2 Implementation of the TRACE vessel component

The use of pipes and side junctions in this manner (referred to as the "side junction approach" in the remainder of this section) is typical of older models that originated prior to TRACE's inception in the early 2000s. TRACE is capable of modeling 3D flow geometries by use of a dedicated 3D vessel component, a feature which the older RELAP5 code lacks. The user can define the appropriate axial, radial, and azimuthal discretization to represent the entire vessel and can model physical flow barriers such as the core barrel and other vessel internals by using the appropriate flow and volume restrictions. The 3D vessel component uses a more robust set of vertical and lateral transport equations which have been shown to provide more realistic solutions, particularly for challenging multidimensional flow scenarios such as LBLOCA. The NRC's developmental and validation basis for reactor transients, including LBLOCA, relies on the use of the vessel component, whereas the legacy pipe and side junction approach is not part of this validation basis (US Nuclear Regulatory Commission, 2012) (US Nuclear Regulatory Commission, 2022) and is not recommended for use by the NRC.

Clifford and Ferroukhi (Clifford & Ferroukhi, 2021) performed an assessment of LBLOCA behavior for a similar pipe and side junction--based TRACE PWR model compared to a 3D vessel component. Their analysis found that the side junction approach predicted a consistently and significantly higher peak PCT and a later quench time than the 3D vessel approach. Note that the FY22 TRACE model considered in the present study produced higher PCT and later quench time than that of all 13 BEMUSE benchmark participants. Therefore, it was considered likely that implementing a 3D vessel component would improve the TRACE model agreement with expected LBLOCA behavior.

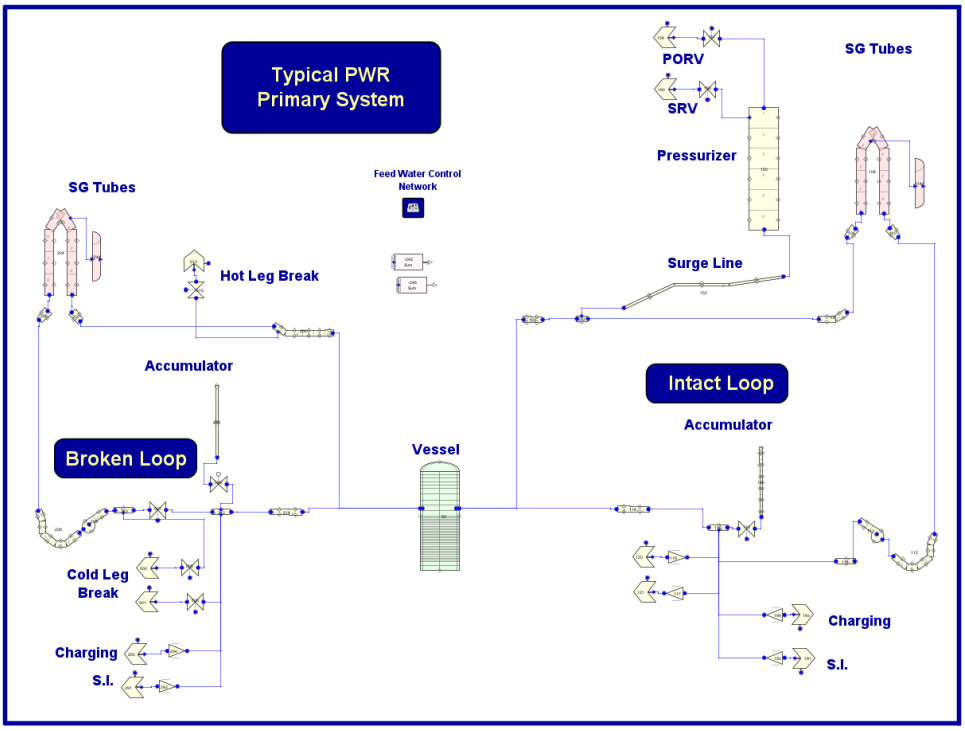

Figure *99*. Visualization of the improved TRACE model with a vessel component.

To conform with the NRC's recommendations and ensure the use of best practices in the TRACE model, the side junction approach was abandoned in favor of a 3D vessel component. To more easily examine the impact of modeling changes and streamline the model development process, a reduced subset of rods was selected for study in this and the following subsections. Out of the larger set of 281 representative high burnup rods, 6 rods were chosen as the most bounding rods (in either the minimum or maximum direction) in terms of rod-averaged power, rod-averaged burnup, and rod internal gas pressure among the high burnup (greater than 62 GWD/MTU) rods. The idea of selecting these rods is to attempt to span the expected conditions, including cladding temperatures, of the larger set of rods. A seventh rod was also included, which was the highest power rod, not only among high burnup rods but among all rods in the core. This gives context for how the high burnup rod conditions compare to the actual highest PCT rod in the core. These seven rods are described in **Table *16***.

Table 16. Potentially bounding rods used for the fuel temperature study

Description	Assembly	Pin Column	Pin Row	Value
Max. power rod	C-10	13	9	1.137
Min. power rod	E-15	17	17	0.115
Max. burnup rod	A-11	5	13	74.7 GWd/MTU
Min. burnup rod	F-11	16	16	61.7 GWd/MTU
Max. internal pressure rod	C-8	13	13	28.9 MPa
Min. internal pressure rod	B-13	17	1	8.7 MPa
Max. power rod (global)	G-13	13	14	1.393

For the first iteration of the vessel model, a coarse vessel nodalization was employed to resemble the side junction approach as closely as possible. Here, the vessel was discretized into only a single azimuthal sector and two radial rings: one for the downcomer and one for the core. The original axial discretization of 18 uniform nodes across the fuel was applied to the vessel. This nodalization meant that flow through the core was strictly one dimensional, with no azimuthal or radial effects modeled within the core. This is similar to how the core was modeled in the side junction approach, in that most of the core was contained in a single lumped core average flow channel.

Figure 100 compares the results for the side junction model and the initial vessel model for the seven limiting rods. With the initial vessel model, the temperature spike during the stored energy heat-up phase (first several seconds of the event) was more pronounced, and the quenching of the fuel rod during the decay energy heatup phase (remainder of the event) occurred much sooner. The quenching time can be deduced as the time when the cladding temperature sharply drops to around 400 K, indicating that the rod surface has left the post-CHF heat transfer regime and has once again been blanketed or quenched in liquid. For the highest power rod, the maximum PCT during the event was approximately 200 K less for the vessel approach than for the side junction approach. The lower maximum PCT and earlier quench time is more consistent with typical LBLOCA results, including those of the BEMUSE benchmark participants as discussed in a later section.

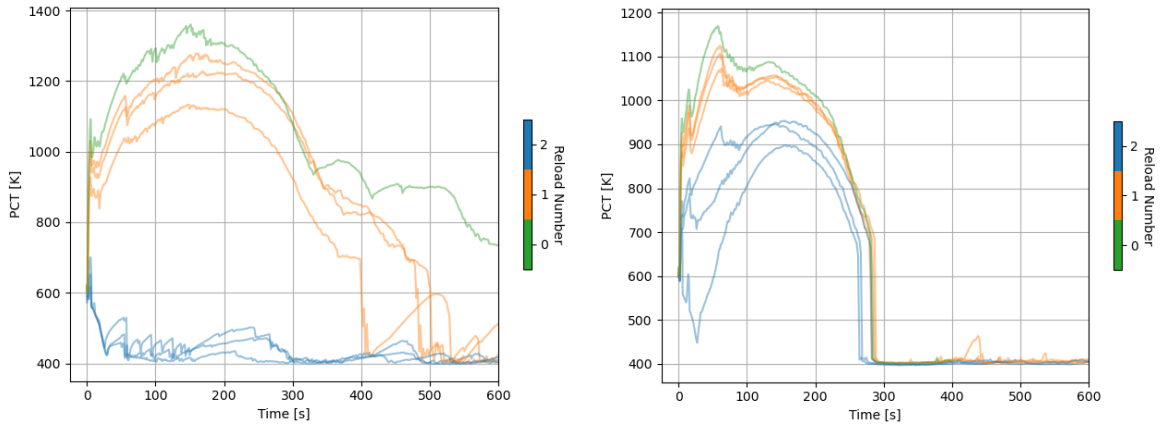

Figure *100*. **Limiting rod PCT results for the side junction model (left) and initial vessel model (right).**

A potential deficiency in this initial vessel model is that the twice-burned fuel rods (blue lines in **Figure** 100) achieved dramatically higher cladding temperatures during the event compared to the results from the side junction approach. Although the side junction approach lumped most of the core into a single channel, it did have separate flow channels for the rod and assembly of interest in each TRACE case. For rods with an average peaking factor near 1, similar TH conditions will be observed across these three channels. This condition has thermal hydraulics similar to that predicted in the initial vessel model, which collapses the entire core to a single channel.

However, for rods with a very low peaking factor, such as for twice-burned fuel, the three-channel approach accounts for the lower heat deposition in the fluid surrounding the rod of interest, whereas the single-channel vessel model does not. Instead, it applies the core average TH conditions to the rod of interest, resulting in PCT values at or above 800 K during the event compared to 500 K or lower for most of the event in the three-channel approach.

Therefore, this comparison demonstrates that (1) the vessel approach produces a much different cladding temperature evolution than the side junction approach which is more consistent with expected LBLOCA behavior, but also that (2) spatial TH effects across the core have an important impact on LBLOCA cladding temperatures, requiring greater radial and/or azimuthal fidelity than a single-channel vessel.

Therefore, the following sections focus mainly on improving the azimuthal and radial fidelity of the model to achieve the most accurate possible clad temperature predictions.

5.2.3 Splitting of the Intact Loops

As discussed above, the FY22 model represented the three intact loops of the plant as a single lumped loop, with an additional broken loop. Best modeling practices and NRC guidelines indicate that all plant loops should be modeled individually and each should connect to a different azimuthal node of the vessel. This was done to give realistic azimuthal dependence to the vessel and core predictions. Although each of the four loops is configured in the same way in terms of geometry, steam generator behavior, and so on, fluid interactions in the downcomer will ensure that the two intact loops closest to the broken loop will behave differently than the intact loop farthest from the broken loop. Lumping the three intact loops together will neglect this effect, as would modeling the vessel with fewer than four azimuthal sectors.

First, the lumped intact loop was divided into three individual loops. A given loop in the TRACE model consists of 40 pipe components, 1 heat structure component, and over 100 control system components. These model the primary flow and secondary steam generator flow, primary to secondary heat transfer, steam generator water level control, feedwater control, and bypass and relief valve controls. These components were rigorously duplicated such that each of the three intact loops contained a copy of all components.

Because of the complexity of this undertaking and the possibility of mistakes, a verification case was run first using the four separate loops connected to the simplified vessel in the previous section (which lacked azimuthal dependence). Because this vessel eliminates any azimuthal variation, the three intact loops should produce the same behavior as the lumped version in this idealized test case.

This was confirmed to be true in that the steady-state flow, temperature, and pressure values in the three separate intact loops were found to match within 0.01%, and the behavior across the three loops remained virtually identical throughout the LOCA transient, as well. As shown in **Figure** 101, this similarity in loop behavior resulted in very similar PCT behavior in the limiting fuel rods. Because no noticeable differences were found in the behavior of each of the three intact loops for this idealized test case, the minor PCT differences are attributed to pseudo-random variations from numerical effects. It was therefore concluded that the splitting of the intact loops was performed correctly.

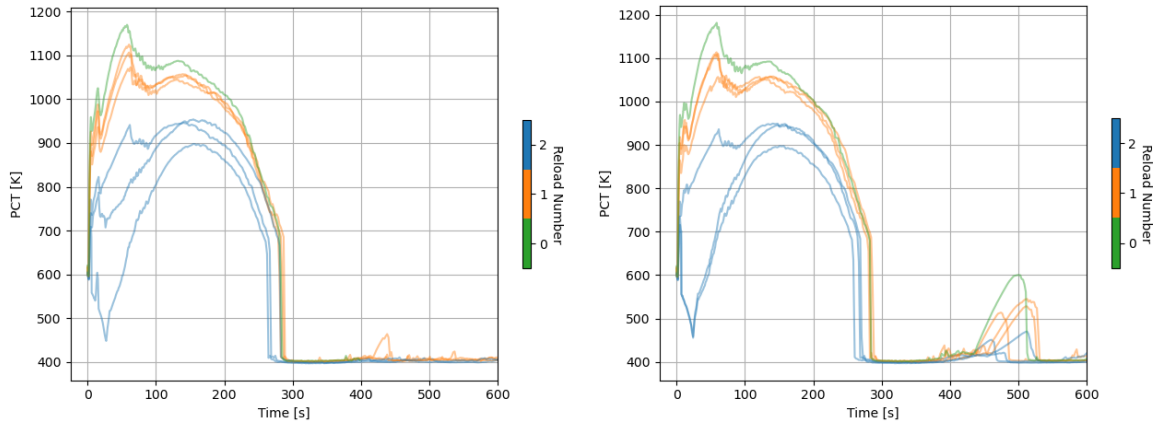

Figure *101*. Limiting rod PCT results for the lumped intact loop case (left) and separate intact loop case (right).

5.2.4 Four-Azimuthal Vessel

The next step was to introduce azimuthal dependence into the vessel component and assess the impact. Once the intact loops were split, realistic azimuthally dependent interactions between the vessel and the balance of plant became possible.

Figure 102 compares the results for the single-azimuthal and four-azimuthal vessel models. The rod results for the second azimuthal sector (the one connected to the broken loop) are shown. Because of this sector of the core's proximity to the broken loop, this sector was expected to give the most limiting PCT behavior. Note that the core loading pattern in this cycle design is eighth-core symmetric, such that the rod burnups and power peaking factors are identical in each of the azimuthal sectors. Therefore, TH effects are the only driver of the azimuthal variation in the results.

The inclusion of azimuthal dependence had a modest impact on the PCT results, with rod-by-rod peak PCTs typically within 20 K between the one- and four-azimuthal models.

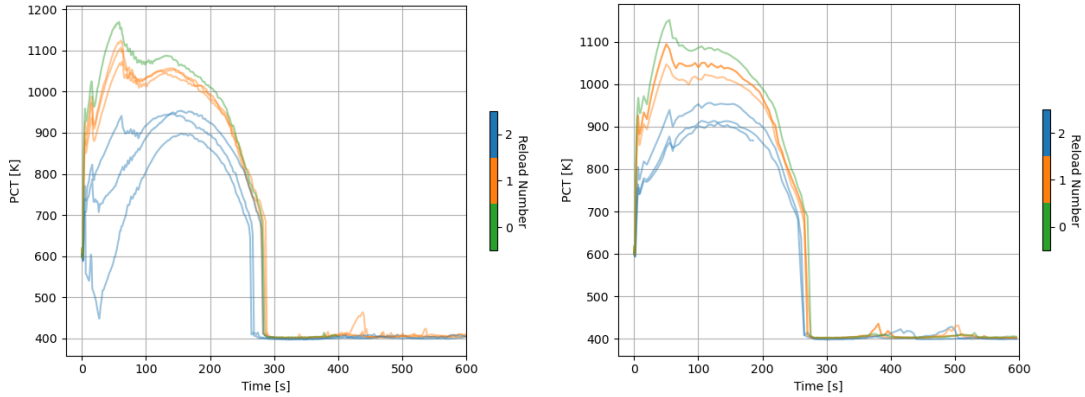

Figure *102*. Limiting rod PCT results for the single-azimuthal vessel model (left) and four-azimuthal vessel model (broken-loop sector) (right).

To investigate further, TH and rod conditions were compared across the four azimuthal sectors. Results were investigated for the first limiting rod shown in **Table *16*** (the high-burnup rod with the highest power) which corresponds to the once-burned rod with the highest PCT in **Figure** 102. These results, which are shown in **Figure** 103, indicate that very little variation exists in the azimuthal direction in terms of the flow and thermal conditions of the fuel rods. The broken loop is attached to Quadrant 2, which is the quadrant that was expected to give the most limiting PCT results, at least during the reflood phase. During the blowdown phase, coolant rushing out of the core causes a significant cooling effect on the fuel rods, which would be expected to have an especially strong effect in Quadrant 2 because it is closest to the break. Therefore, the PCT is not necessarily expected to be the highest in Quadrant 2 during this phase. However, during refill and reflood, the safety systems only inject cold coolant into Quadrants 1, 3, and 4 (the intact legs), so the downcomer and lower plenum of Quadrant 2 would be expected to receive a weaker cooling effect from the safety systems. Therefore, the Quadrant 2 fuel rods would be expected to give higher cladding temperatures, at least to some extent.

Surprisingly, though, Quadrant 3 exhibited the highest PCT, whereas the other three quadrants had approximately 30 K lower PCT. From observing the behavior across several different cases during this project, the ordering of the quadrants in terms of PCT appears to be essentially random due evidently to numerical "noise" rather than actual physical effects. For all practical purposes, the results can be considered azimuthally uniform.

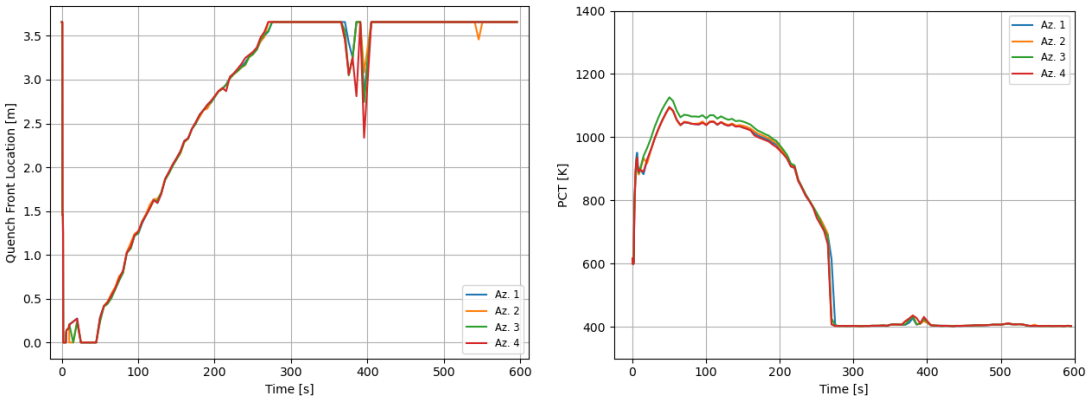

Figure *103*. Quench front location (left) and PCT (right) for Limiting Rod 1 in each azimuthal sector.

Closer examination was made of the vessel TH behavior to investigate further. The TRACE model predicts that by the time the coolant traverses the downcomer and lower plenum and enters the active core, the coolant will be sufficiently well-mixed so that any azimuthal variation is essentially nonexistent by that point. This is evident in the liquid temperature results shown in **Figure** 104. The liquid temperatures in Quadrant 2 are slightly higher than in the other quadrants at the downcomer cold leg inlet, but this azimuthal variation is smaller at the bottom of the downcomer and no longer evident at the core inlet. Similar behavior was seen in other quantities such as void fraction and flow rate. No experimental or computational studies were found in the literature that gave sufficient details to corroborate or contradict this finding of azimuthal uniformity, so the validity of this finding remains an open question.

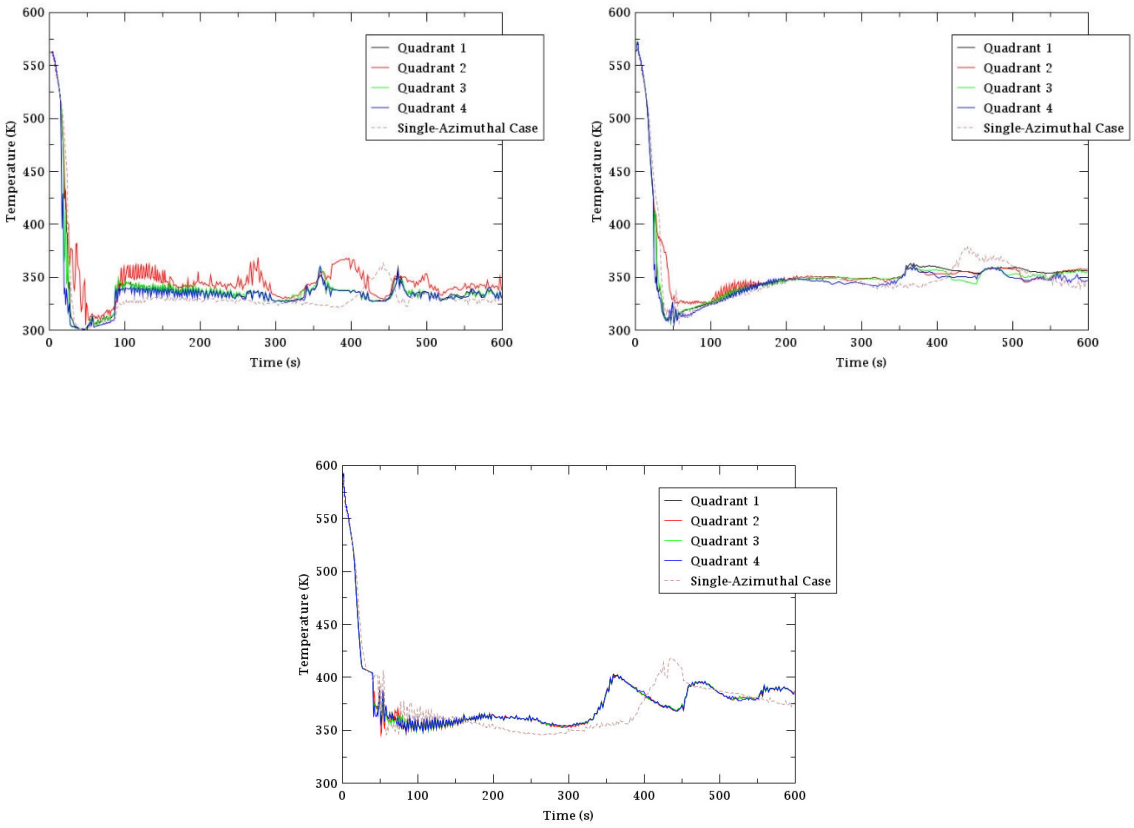

Figure *104*: Liquid temperature at the downcomer cold leg inlet (top left), lower downcomer (top right), and core inlet (bottom) as a function of azimuthal quadrant

A sensitivity study was performed on two downcomer modeling parameters to determine whether modeling the downcomer differently could impact the degree of azimuthal variation in the core. First, the flow area fraction along the cell boundaries between adjacent quadrants of the downcomer was adjusted from 1.0 (used in the results above) down to as low as 0.10. Next, the flow area fraction was kept at 1.0, but instead, form loss factors were applied to these cell boundaries that ranged from 0 (used in the results above) up to extreme values of 1,000 or higher. The intent of this study was to reduce the amount of fluid mass and energy mixing that occurs in the downcomer which would perhaps have increased the azimuthal variation by the time the fluid reaches the core.

However, not even these aggressive downcomer modifications produced a significant variation in behavior between the four quadrants. It appears that even the reduced mixing in the downcomer and the mixing in the lower plenum is sufficient to cancel out any azimuthal variation within the core.

5.2.5 Eight-Azimuthal Vessel

The NRC guidelines recommend 6 to 8 azimuthal sectors in the vessel. This in part is to accommodate cold leg vessel inlet nozzles which are often not spaced at regular 90° intervals around the vessel's outer shell. For example, the nozzles may have a 45°-135°-45°-135° spacing, with two pairs of inlets spaced closely together. An eight-azimuthal discretization can accurately place these inlets to properly account for azimuthal dependence as the flow enters the vessel and mixes in the downcomer.

Figure 105 shows the limiting rod results for the eight-azimuthal vessel model. Unfortunately, numerical issues were observed which caused five of the seven rod cases to fail prior to 100 seconds into the event. The cause of this numerical difficulty is unknown and requires further investigation. However, up until the point of failure, the limiting rod, once-burned rods, and at least one of the twice-burned rods exhibited very similar cladding temperatures in the eight-azimuthal case compared to the four-azimuthal case.

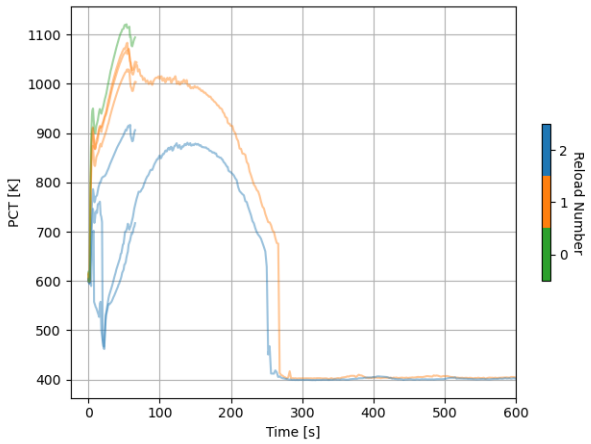

Figure *105*: Limiting rod PCT results for the eight-azimuthal vessel model.

Investigation of TH parameters revealed behavior similar to that shown in **Figure** 103 and **Figure** 104. Because of the numerical difficulties encountered in the eight-azimuthal model and the evidently sufficient accuracy of the four-azimuthal model, a four-azimuthal discretization was selected as the best choice for the remainder of this work.

5.2.6 Radially Discretized Core

Once the four-azimuthal model was established, additional radial fidelity was added to the core to examine the impact. The NRC guidelines recommend two radial rings in the core. Specifically, for a Westinghouse 4-loop, 193-assembly plant, the NRC recommends allocating the assemblies among the two rings as shown in **Figure** 106, with 56 full-core assemblies (14 quarter-core assemblies) in Ring 2. Note that first row and first column of **Figure** 106 represent half-assemblies because the core symmetry lines go through the middles of the actual assemblies; therefore, Assemblies 8 and 53 are half-assemblies, such that there are 14 quarter-core assemblies in Ring 2.

Of the seven limiting rods, three are twice-burned rods located in Ring 2. The remaining four rods (fresh and once-burned rods) are in Ring 1.

1	2	3	4	5	6	7	8
9	10	11	12	13	14	15	16
17	18	19	20	21	22	23	24
25	26	27	28	29	30	31	32
33	34	35	36	37	38	39	
40	41	42	43	44	45	46	
47	48	49	50	51	52		
53	54	55	56				

Figure *106*: Quarter-core assembly map showing Ring 1 assemblies (black) and Ring 2 assemblies (green).

A comparison of results using the one- and two-ring models is shown in **Figure** 107 and **Figure** 107. The increase in radial fidelity had a modest impact on the peak PCT in the Ring 1 fuel rods, but it had a dramatic impact on peak PCT in the Ring 2 fuel rods. This points to a large difference in TH conditions experienced in Rings 1 and 2. The much lower average power in the Ring 2 assemblies caused less energy to be deposited in the Ring 2 coolant. This resulted in not only a smaller rate of cladding heat-up in the initial stored energy heat-up (SEH) phase, but also a more rapid cooling of the fuel rods, earlier quenching, and lower peak PCT in the Ring 2 fuel rods in the decay energy heatup (DEH) phase.

Ring 1 contains 70% of all assemblies in the core, which may explain why the Ring 1 cladding temperature behavior closely followed the initial full core behavior observed in the single-ring model. This similarity was seen up through the first ~50 s of the event in terms of both the initial cladding heat-up rate and the peak PCT during the event. However, the behavior of the two models diverged significantly after that: Ring 1 of the two-ring model had a much faster decrease in cladding temperature and a much earlier quench time of approximately 180 s compared to the one-ring model at approximately 270 s.

The fact that both rings produced quicker cladding cooldown and quenched earlier than the single-ring model indicates that spatial effects may extend beyond the core. The increase in radial fidelity also impacts the nodalization in the lower and upper plena, as well as the vessel's upper internals. The increased nodalization in these regions could be contributing to the significant overall change in behavior observed during the event.

Because of the large impact caused by using a 2-ring model, it further radial refinement may also have a significant impact. Interior to the outermost ring of low-power high-burnup assemblies, an additional ring of high-power low-burnup assemblies referred to as the *ring of fire*, which be seen by examining the

radial burnup map in **Figure** 69. A logical next step in refinement is to model the ring of fire as a separate ring, thus resulting in a three-ring core treatment. An even finer approach would be to model the core using a cartesian vessel component, which allows modeling the core as a rectangular grid, thus allowing TH modeling of up to one channel per assembly in the core. A separate heat structure for each assembly, and perhaps the hot rod as well, could be attached to these TH channels to provide assembly-level fidelity in the core. These approaches would be useful to examine in future work to gain further understanding of the impact of core radial discretization.

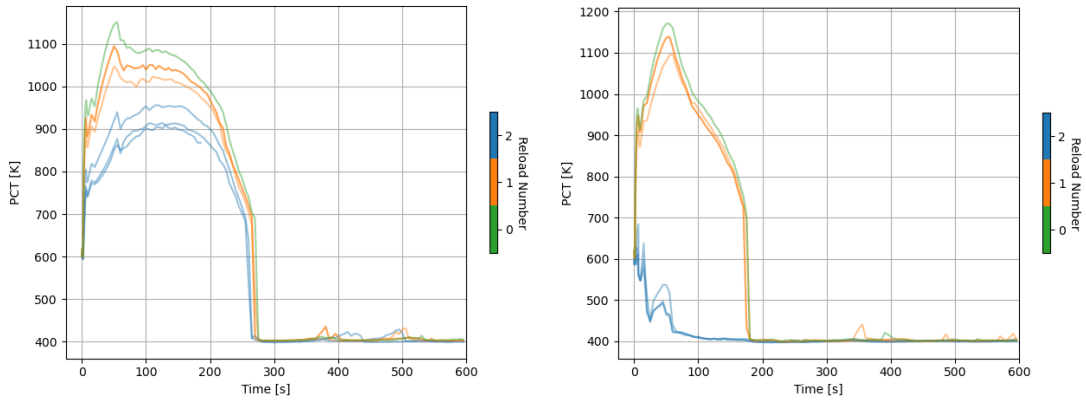

Figure *107*. Limiting rod PCT results for the four-azimuthal, one-ring model (left) and four-azimuthal, two-ring model (right).

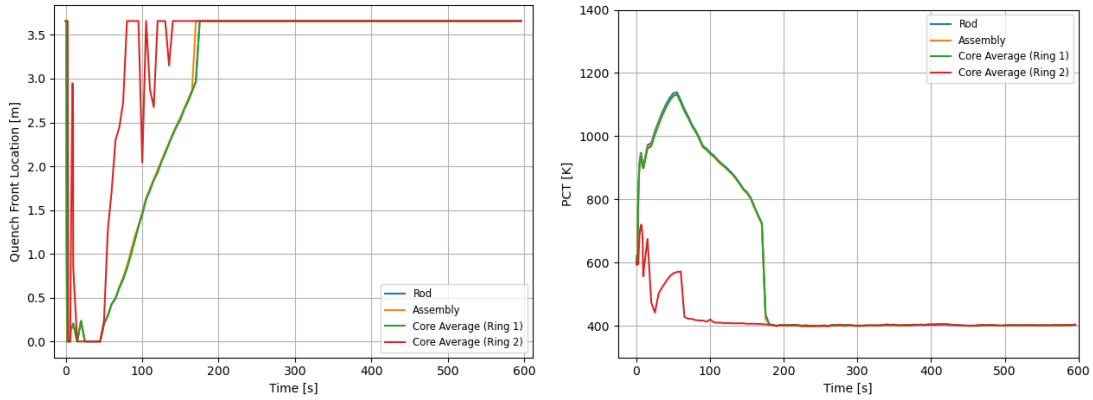

Figure *108*. Quench front location (left) and PCT (right) for each heat structure in Quadrant 2 for the Limiting Rod 1 case.

5.2.7 Radial Flow Area Sensitivity

The TRACE vessel component calculates a nominal flow area between adjacent cells in the radial, azimuthal, and axial directions based on the mesh spacing in each direction and assuming a basic cylindrical geometry. TRACE also allows a user-specified array of flow area fractions for each cell-to-cell connection in the radial, azimuthal, and axial directions separately. These flow area fractions represent the ratio of the actual flow area to the nominal flow area, thus accounting for the vessel's geometric considerations such as vessel curvature and flow obstructions resulting from the vessel's internal solid structures and core structures.

In the previous subsection, the radial and azimuthal flow area were set to 1.0, to allow for the maximum transport of mass, momentum, and energy laterally across the core regions without consideration of flow obstruction from fuel rods and guide tubes. However, a past study with the CTF code found that a reduced

lateral flow area accounting for the presence of fuel rods and guide tubes produces better agreement between nodal (quarter-assembly) and subchannel-resolved CTF models (Wysocki, Salko, & Arshavsky, 2023). A reduced lateral flow area was therefore recommended for use in the nodal model that is equal to the sum of the lateral flow areas in the rod-to-rod gaps among the constituent subchannels. This situation is similar to that in the present TRACE model, in which the detailed flow patterns within and between assemblies are being approximated by large, coarse flow channels.

To investigate the impact of a reduced lateral flow area in the TRACE LBLOCA model, the radial and azimuthal flow area fractions in the core were reduced from 1.0 to 0.249, which is the fraction of the lateral flow area not obstructed by fuel rods across a given plane of fuel rods in an assembly. This is consistent with the flow area reduction assumed in the previous CTF study (Wysocki, Salko, & Arshavsky, 2023).

Figure 109 and **Figure** 110 compare the results for lateral flow area fractions of 1.0 and 0.249 in the four-azimuthal two-ring core model. The impact of the lateral flow area fraction on cladding temperature was found to be minor, with only a small difference observed for the seven limiting rods. This could indicate that the lateral mixing between cells is relatively small, even for a 1.0 flow area fraction. As the size (i.e., volume) of cells increases, the ratio of the lateral flow area to the cell volume increases, which could make lateral transport relatively less significant.

This increase could simply be a consequence of the coarse radial fidelity, given that the entire core is being modeled with only two radial regions. In other words, there could still be significant subchannel-to-subchannel and assembly-to-assembly lateral mixing effects (which a higher fidelity model could address), but the lateral mixing on a full-core spatial scale may be less pronounced. Note that this only refers to the actual fluid transport across the cell boundaries; the core ring discretization still has a large effect in terms of where the decay heat is deposited in the core and how this impacts the local TH and cladding temperature conditions.

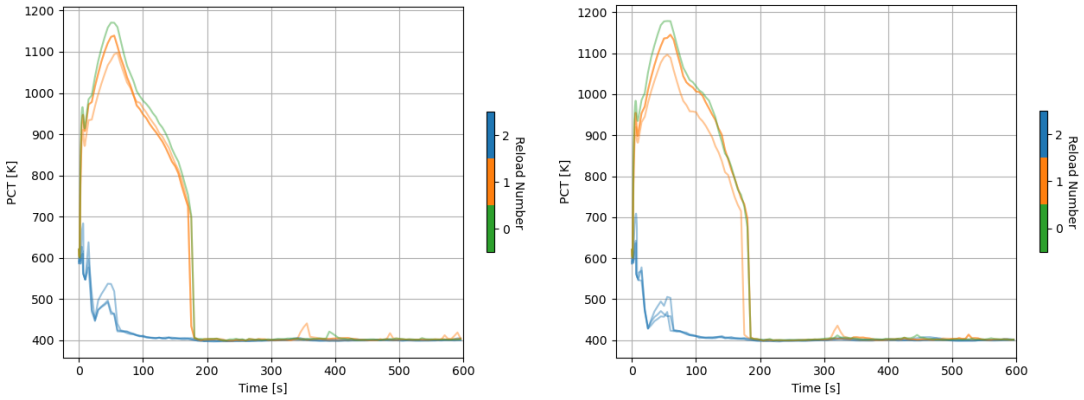

Figure *109*. Limiting rod PCT results for the four-azimuthal two-ring model with a core lateral flow area fraction of 1.0 (left) and 0.249 (right).

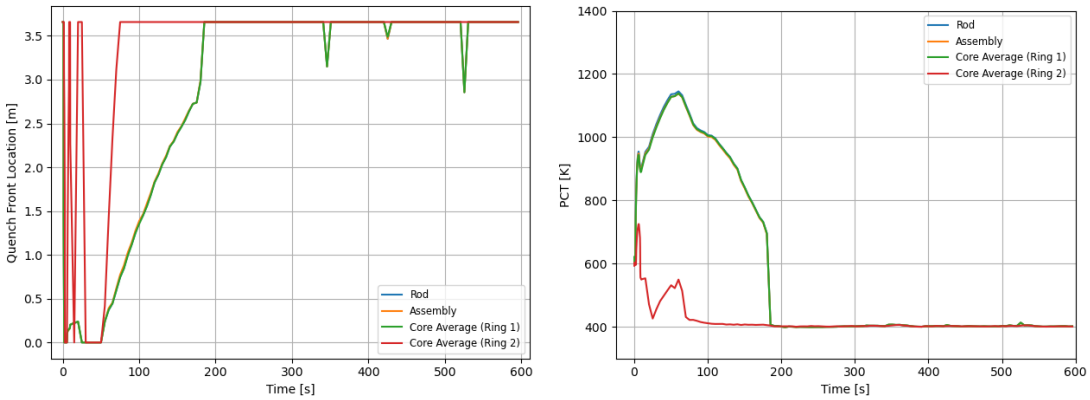

Figure *110*. Quench front location (left) and PCT (right) for each heat structure in Quadrant 2, when using a flow area fraction of 0.249.

5.2.8 Fuel Modeling Changes

The NRC recommended two improvements to the heat transfer modeling within each fuel rod. The first was to increase the number of radial nodes in the pellet and cladding. The FY22 model used three radial rings in the pellet and one in the cladding, which is consistent with the BEMUSE specifications. Based on NRC recommendations, this was increased to six rings in the pellet and two in the cladding.

The second recommendation was to apply a more realistic gas composition within the pellet-cladding gap and upper/lower plenum in the fuel rod. The FY22 model used a gas composition of 100% helium, which is consistent with fresh fuel. However, gaseous fission products—primarily xenon and krypton— are generated within the fuel pellet as a function of burnup, and a certain fraction of these is released into the cladding, depending on the power history of the reactor during operation.

BISON calculates the fission gas release fraction for each of the high burnup rods. To provide a more realistic value in TRACE, the fission gas release fraction was averaged across all the BISON-analyzed high burnup rods at the end of cycle 30, when the LBLOCA was assumed to occur. This amounted to a gap gas mole composition of 89.4% helium, 9.0% xenon, and 1.6% krypton for the high burnup rods. These values were applied to the TRACE model.

Note that transient fission gas release will occur during the LBLOCA transient in reality, but this is not accounted for in the TRACE model. This is not expected to significantly impact the cladding temperatures during the event. The gas composition impacts the calculated gap conductance, which impacts the initial steady state temperatures in the fuel rod. This in turn impacts the amount of leaving the fuel rod at the start of the LBLOCA and therefore impacts the initial cladding heat-up rate. However, additional gas composition change caused by transient fission gas release during the LBLOCA does not have a significant impact on the transient cladding temperatures. This is because the rod powers are sufficiently low during the event (because of the scram at 0 sec) so that the temperature gradient across the gap and the rest of the fuel is small. Transient fission gas release does impact the rod's internal pressure and burst susceptibility; however, burst is not modeled in this TRACE analysis. (Note that in FY22, it was modeled with transient BISON simulations instead). Because TRACE is only being used for determining the cladding temperatures and fluid conditions, transient fission gas release does not need to be taken into account here.

The increase in radial fuel modeling fidelity combined with the change in gas composition resulted in the Rod 1 steady-state fuel temperatures shown in **Figure** 111. The temperatures predicted by BISON for Rod 1 are also shown. The average difference in centerline fuel temperature between TRACE and BISON was approximately 80 K; for the FY22 model, the average centerline fuel temperature difference was approximately 50 K. However, previous analyses have estimated the uncertainty in BISON fuel centerline temperatures to be ±10% at any burnup (Williamson, et al., 2016). For the ~1,500 K centerline temperatures shown in **Error! Reference source not found.**, the estimated uncertainty would be ~150 K. T his 80 K difference between TRACE and BISON is well within this estimated uncertainty range and therefore is considered acceptable for this analysis.

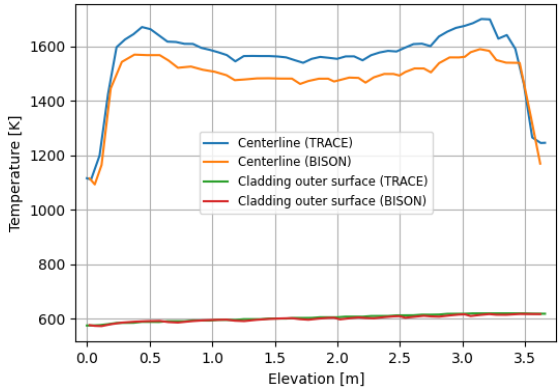

Figure *111*. Steady-state TRACE-BISON fuel rod temperature comparison for Rod 1.

As seen in **Figure** 112, the fuel rod radial discretization and gas composition changes produced an increase of 30 K to 50 K in cladding temperature after the initial heatup (first 5 seconds) in the Ring 1 (fresh and once-burned) fuel rods. This translated to a similar increase in their peak PCT and a slight delay in quench time. The Ring 2 (twice-burned) fuel rods were not significantly impacted because of their rapid cooling during the event.

The right-hand plot in **Figure** 112 constitutes the final results for the seven limiting rods once all recommended model improvements were implemented. Section 5.3 applies the final TRACE improvements to the BEMUSE benchmark case to assess the change in those results, and Section 5.4 presents the final high-burnup LBLOCA results for all 281 high-burnup rods.

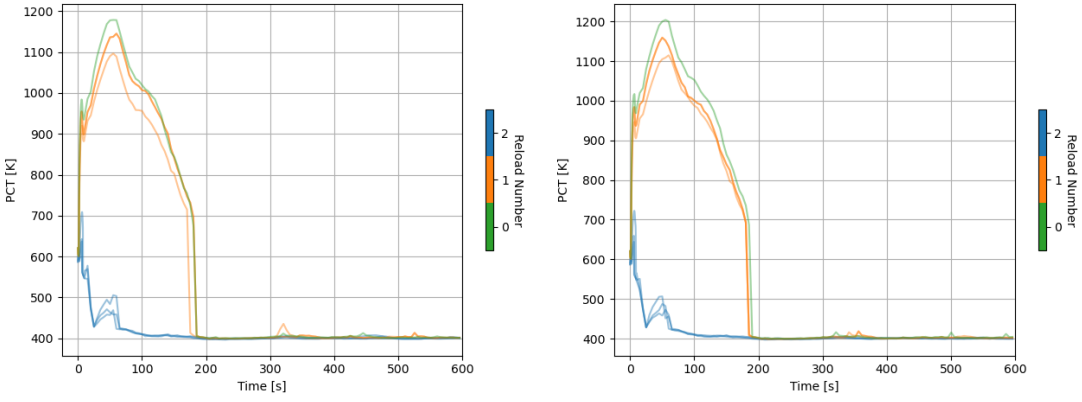

Figure *112*. Limiting rod PCT for the original (left) and new (right) fuel rod parameters.

5.3 Updated LBLOCA Benchmark Results

The final high burnup TRACE model discussed above was adapted once again to the BEMUSE benchmark conditions using the same approach that was used in the benchmark comparisons performed in

FY22 (Capps, Hirschhorn, Wysocki, & Greenquist, 2022). This included applying the BEMUSE-specified total core power, total core flow rate, primary system pressure, axial fuel rod power profiles, and radial fuel rod power peaking factors for the three solved rods (hot rod, hot assembly, and remainder of the core).

Additional modeling and benchmark details are given in the previous work (Capps, Hirschhorn, Wysocki, & Greenquist, 2022). This subsection presents only the updated benchmark results to confirm that the TRACE primary and secondary system models still produce the intended behavior and to reassess how well the TRACE cladding temperature results agree with the benchmark participants.

Table 17 compares the steady-state core and system conditions in the updated TRACE BEMUSE model compared to the FY22 model and the intended values specified in the BEMUSE report. All values match the FY22 values closely, with only minor differences. Note that, as discussed in the previous report (Capps, Hirschhorn, Wysocki, & Greenquist, 2022), the secondary pressure was intentionally adjusted in the TRACE model to achieve the target core outlet temperature. It was concluded previously that some differences exist between the TRACE and BEMUSE steam generator modeling which impact the secondary pressure required to achieve a given average primary coolant temperature. However, the secondary pressure adjustment resulted in the same effective steam generator heat transfer efficiency in TRACE vs. BEMUSE, which ensures similar LBLOCA behavior.

Table *17*. Steady-state conditions of the TRACE model compared to published BEMUSE values

Operating condition	Units	TRACE (FY22)	TRACE (Updated)	BEMUSE
Power	MW	3250	3250	3250
Hot leg pressure	MPa	15.53	15.62	15.5
Pressurizer level	m	8.8	8.8	8.8
Core outlet temperature	K	603	602	603
Core flow rate	kg/s	17,357	17,357	17,357
Secondary pressure	MPa	7.44	7.44	6.7
Feedwater flow per loop	kg/s	436	434	439
Accumulator gas volume	m^3	15.1	15.1	15.1
Accumulator liquid volume	m^3	23.8	23.8	23.8
RCP speed	rad/s	118.26	126.32	120.06

The most relevant primary system transient responses during the LBLOCA are shown in **Figure** 113 through **Figure** 117, with comparison to typical results seen in the published BEMUSE benchmark participants' analyses. All system quantities show excellent agreement with the BEMUSE published values and no significant deviations from the FY22 TRACE values. This is not unexpected, because the changes made to the TRACE model focused mainly on the vessel and core. The one change made to the balance of plant was to split up the lumped intact loop into three individual loops, but this primarily impacts the fluid conditions entering the vessel and does not greatly change the primary loop response overall.

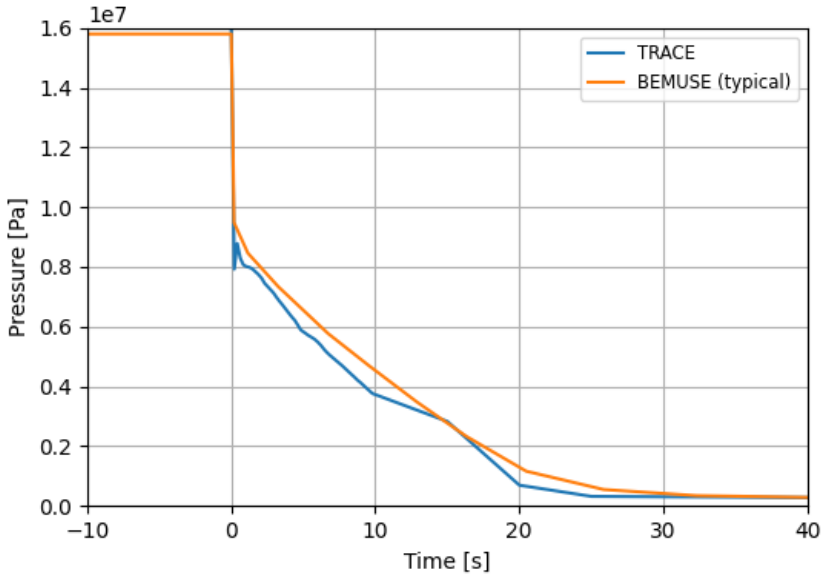

Figure *113*. LBLOCA break pressure.

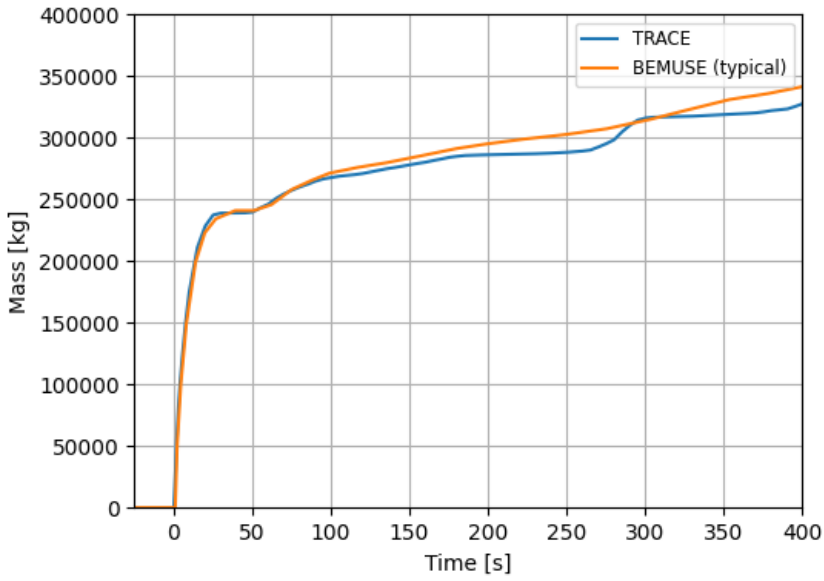

Figure *114*. LBLOCA integral break flow rate.

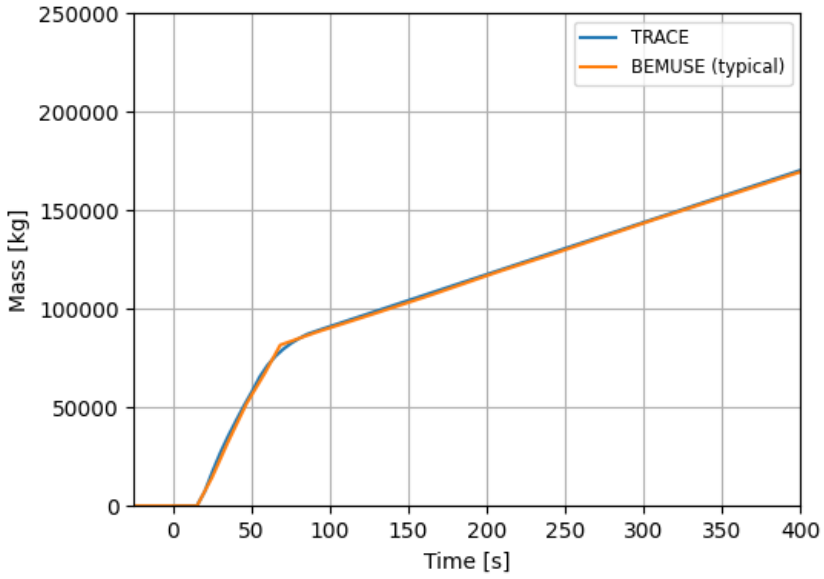

Figure *115*. LBLOCA total emergency core cooling system (ECCS) flow rate.

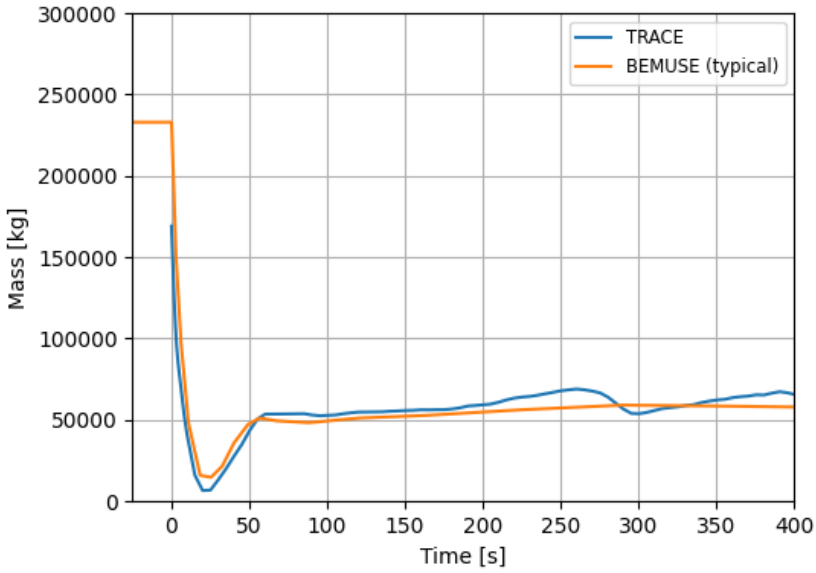

Figure *116*. LBLOCA primary system fluid mass.

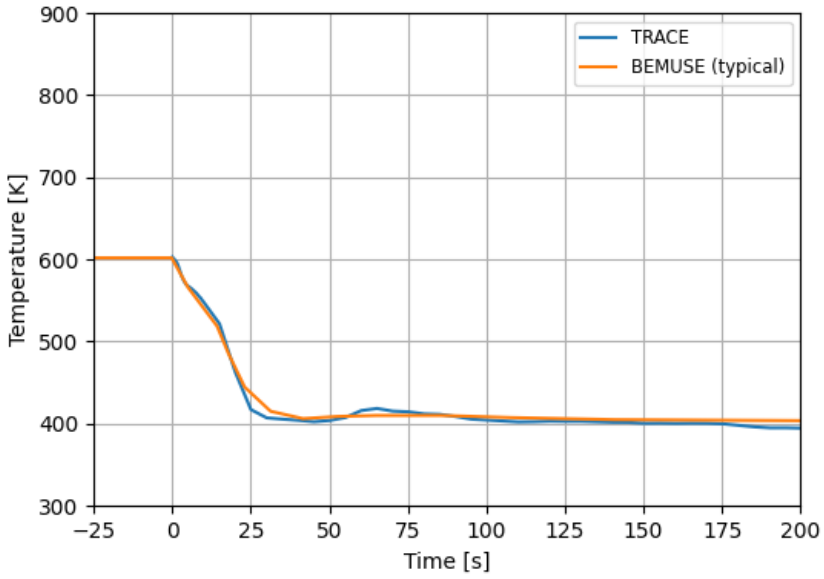

Figure *117*. LBLOCA intact loop hot leg temperature.

Figure 118 compares the PCT response for the hot fuel rod with the FY22 results and three of the benchmark participants. As discussed in the FY22 report (Capps, Hirschhorn, Wysocki, & Greenquist, 2022), because tabular time-dependent results were not published for BEMUSE, three of the thirteen participants' results were manually extracted from the published plots to provide a representative comparison. These three sets of results constitute the lowest peak PCT (CEA), highest peak PCT (EDO), and an intermediate peak PCT (AEKI) among the thirteen participants. They also include the earliest (EDO), latest (CEA), and an intermediate (AEKI) quench times among all participants.

The FY22 TRACE results exhibited a higher peak PCT and a later quench time than any of the participants' results. Although this indicated that the model was conservative (and therefore the high-burnup analyses were likely conservative, as well), the intent of this study was to provide a best-estimate quantification of LBLOCA behavior. The updated TRACE results better serve this function because the peak PCT and quench time are both well inside the range of the benchmark participants' predictions.

One interesting caveat is that the initial temperature rise during the SEH phase (first 5 s) was lower in TRACE than in the participants' predictions. The initial temperature rise in the FY22 model was on the low end of the participants' predictions, but the updated model temperature increase was notably less. The exact reason for this is unclear. Based on examination of the earlier results given in Section 5, it appears that the initial temperature rise showed slight decreases across each of several different modeling changes, with no single model modification standing out as a single cause. However, one possibility is that the FY22 model included a dedicated channel representing the subchannel around the hot rod, but the updated model does not. In the updated model, TH conditions for the hot rod are assumed to be the same as for the remainder of rods in that radial ring. This could contribute to the more rapid temperature rise in the FY22 model, because the hot subchannel may vaporize faster and lead to more immediate departure from nucleate boiling (DNB) than in the updated model. This would point once again to the importance of

radial fidelity on the LBLOCA predictions. However, future analysis would be required to confirm this effect.

Nevertheless, the longer term DEH cladding temperature evolution in the updated TRACE model provides greatly improved agreement with the BEMUSE participants' results. In FY22, most if not all of the cladding failures were found to occur in the DEH phase of the event, and the updated TRACE model appears to be significantly more realistic during this phase.

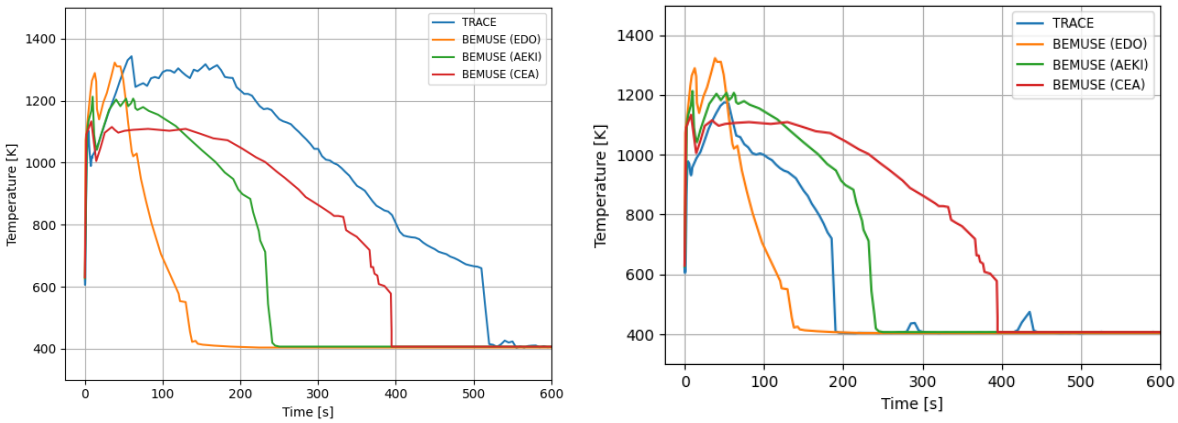

Figure *118*. BEMUSE results comparison for the FY22 TRACE model (left) and the updated model (right).

5.4 Final TRACE results for the 281 high burnup rods

The final PCT results for the updated TRACE model, for all 281 high -burnup rods plus the highest power rod are shown in **Figure** 119. These results correspond to those shown in Section 5.2.8, but they account for all rods instead of only the seven limiting rods.

Recall that the FY22 results for these 282 rods are shown in the left-hand plot in **Figure** 98. Consistent with the results shown in the remainder of Section 5, the updated TRACE model predicts substantially lower peak PCT and quench times than the FY22 model overall. This is true for most of Ring 1 fresh and once-burned rods and is especially true for the Ring 2 twice-burned rods.

The highest power rod exhibited a 239 K decrease in peak PCT, from 1,433 K to 1,194 K. The safety limit for PCT is 1,478 K as defined by 10 CFR 50.46. This gave only a 55 K margin to the limit in the FY22 results, which is not generally typical for best-estimate LOCA analyses with no application of uncertainties or conservatisms applied on plant conditions, operating conditions, or core and fuel modeling parameters. From that perspective, as well as the improved agreement of the BEMUSE model to the benchmark results, the updated TRACE model is a substantial improvement in terms of peak PCT and quench time.

Another interesting finding, however, is that the spread in peak PCT was only approximately 60 K among the once-burned rods in the updated model vss approximately 200 K in the FY22 model. Among the twice-burned rods, this spread was even greater. These trends are attributed to the use of the two-ring core model, which applies the same TH conditions to all rods in each of these two rings. The FY22 model included a channel representing the fluid around the hot rod, as well as a channel for the surrounding assembly, which allowed more localized TH effects to be predicted.

The CTF subchannel results in Section 4 clearly indicate that subchannel-scale TH effects increased the spread in cladding temperatures compared to when lumped assembly channels were used. This is likely an important reason why the spread in the current TRACE PCT results was less than in FY22.

However, the CTF subchannel results also indicate that neighboring assemblies impact the local assembly and rod behaviors. This is especially true for rods near the assembly periphery. The FY22 approach did not include any TH impact from neighboring assemblies. The FY22 model effectively assumes that the conditions outside the current assembly are at the core average TH conditions. The updated model at least provides some influence from nearby assemblies in terms of assuming uniform conditions across the entire ring and azimuthal sector. Effectively, this accounts for the fact that the assemblies adjacent to a given Ring 2 assembly will most likely be low power, whereas assemblies surrounding a Ring 1 assembly will be higher power on average.

Therefore, it is likely that the updated core nodalization better predicts the average cladding temperature in each ring overall (compared to the FY22 model), but it may underpredict the rod-to-rod temperature variation from local subchannel effects.

Based on these results and the Section 4 results, it is clear that spatial TH effects are important on multiple spatial scales, perhaps spanning from the full-core scale down to the subchannel scale. This provides further justification of examining spatial TH effects during LBLOCA on a low subchannel scale as described in Section 4 with CTF.

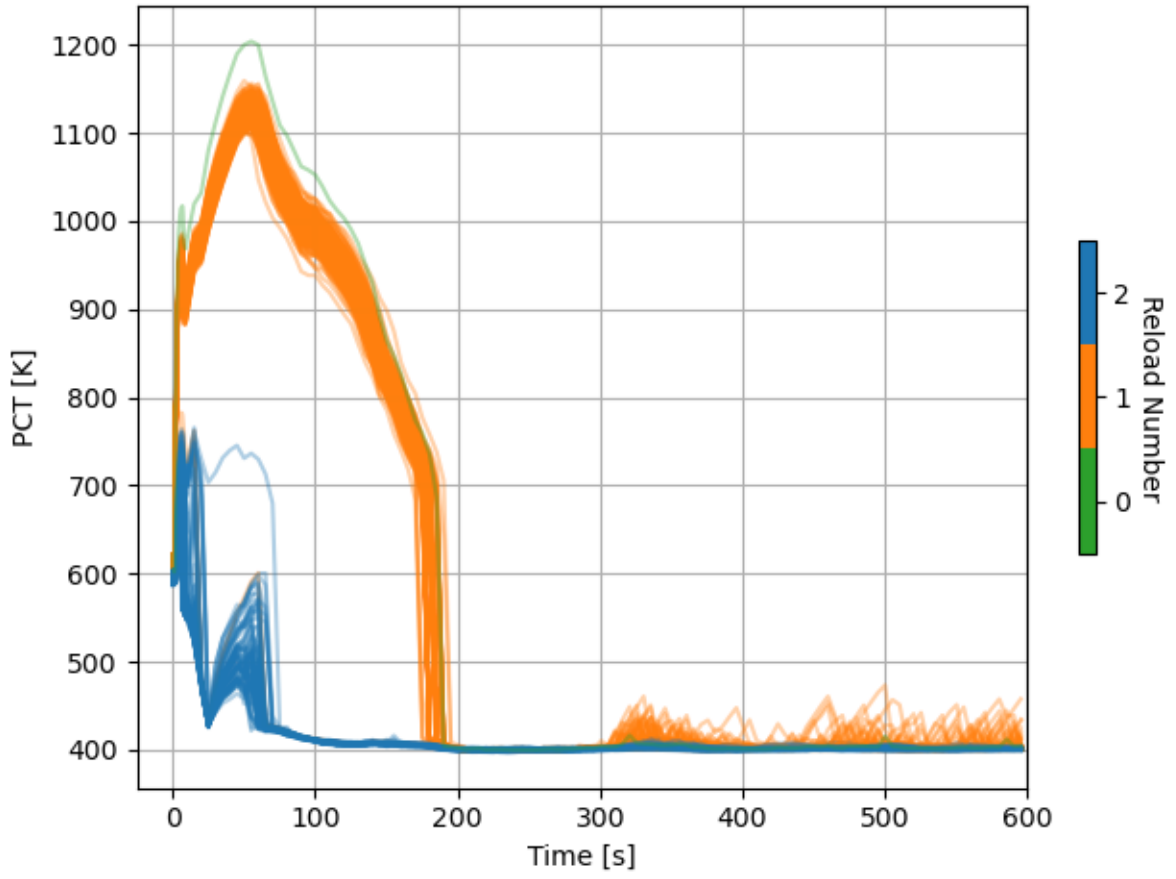

Figure *119*. Updated LBLOCA results for the 281 high-burnup rods and the highest power rod.

A large number of scatterplots and histograms was presented in the FY22 work to characterize the distribution of and correlation between various input and output quantities among the high-burnup rods. Several key plots are recreated here based on the updated results to assess whether any FY22 conclusions have changed.

The PCT during the SEH phase is shown in **Figure** 120. For these purposes, the SEH phase is defined as a transient time from 1 s to 15 s during the event, which covers the time from when the break and scram begins to impact the cladding temperatures to the time by which all rods have experienced their initial rise resulting from stored energy in the fuel. For most rods, this occurred between 5 and 7 sec, but 15 sec was chosen to ensure all rods were captured.

The overall positive trend of increasing SEH PCT with increasing rod-average LHR is as expected. The SEH PCT values are within roughly 50 K less than their FY22 values for most rods. However, compared to FY22, there is an especially large PCT difference between the twice-burned and the fresh or once-burned fuel. This is attributed to the use of two distinct core rings, which causes a difference in steady-state coolant and cladding surface temperatures, as well as more pronounced differences during this phase of the event.

As before, a clear trend was found in PCT vs. LHR, but not in PCT vs. burnup.

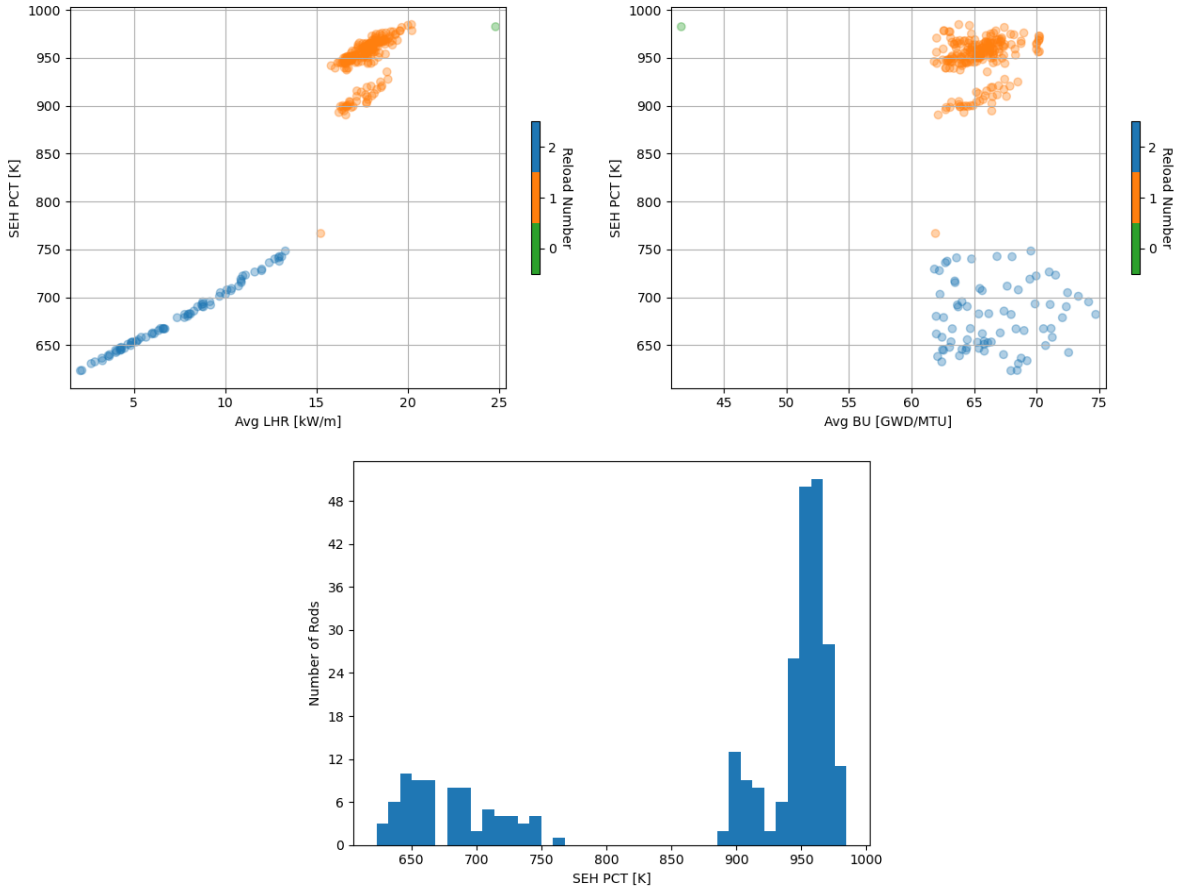

Figure *120*. **SEH PCT vs. rod-average LHR (left), vs. rod-average burnup (right), and as a histogram (bottom).**

The same results are presented for the DEH phase in **Figure** 121. The DEH phase is taken as the remainder of the event after 15 sec and includes cladding heat-up caused by decay heat production, followed by the eventual cooling and quenching caused by the ECCS. As expected, the DEH PCT values were lower for most rods than they were in FY22. However, as with the SEH phase, the once-burned rods (Ring 1) had especially higher PCT than the twice-burned (Ring 2) rods. Still, the trend of increasing PCT with increasing LHR remains clear, although there is once again no clear trend of PCT with respect to burnup.

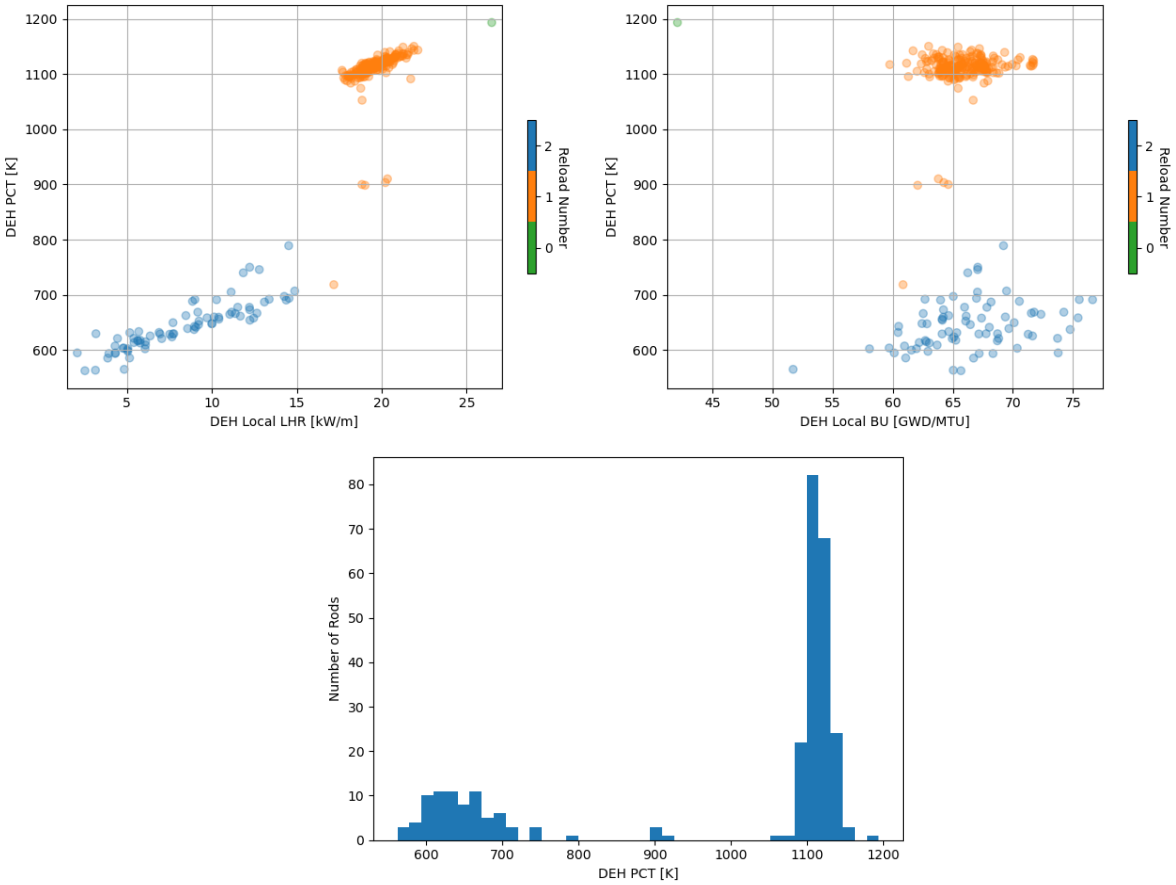

Figure *121*. **DEH PCT vs. rod-average LHR (left), vs. rod-average burnup (right), and as a histogram (bottom).**

In the FY22 analysis, for the majority of the rods, the local burnup where PCT occurred was less than the rod-average burnup by typically 5 to 18 GWD/MTU. Interestingly, this was not found to be the case in the updated TRACE results shown in **Figure** 122. The local and average burnups appear to be nearly the same in most rods, with no clear bias in either direction. However, this could in part be caused by the neglect of local subchannel TH effects in the updated model, which could be masking some radial and/or axial effects on a subchannel and rod-by-rod level.

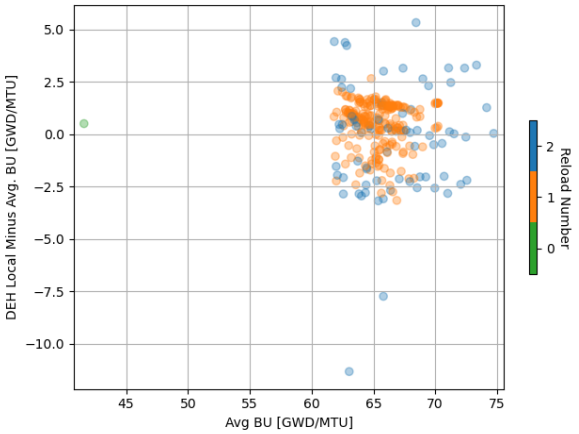

Figure *122*. Difference between the local burnup where the DEH PCT occurred and the rod average burnup.

6. SUMMARY

This report documents efforts to develop a more advanced TH modeling capability for analysis of PWR LOCA transient analysis in support of modeling FFRD. The report builds on previous activities in NEAMS to model FFRD, which used coarser TH methods for LOCA analysis. Specifically, a more advanced TRACE model is being developed using current best practices for modeling of LOCA to determine system response during all phases of the LOCA transient. Secondly, the CTF subchannel code is being used to develop a pin-resolved model of the core region of a high-burnup core.

Because of the lack of CTF-related LOCA modeling activities in the past, this report provides a preliminary validation of CTF LOCA capabilities using the FEBA reflood experiments as well as code-to-code benchmarking against TRACE. Prior to performing the validation, a Dakota-driven sensitivity analysis was performed using 44 different model multipliers in CTF, which were anticipated to impact LOCA reflood results. This study was used to identify models of high importance, which drove an assessment of the CTF LOCA models and comparison against legacy documentation on previous versions of COBRA-TF. This review resulted in several corrections of CTF LOCA models. In addition to this work, several numerical improvements were made to better control the CTF iterative solution for better stability of pin-resolved reflood cases. In addition to the CTF sensitivity study, a similar study was performed on TRACE. Although the most important models in CTF were mainly related to droplet quantity and size, the most important models in TRACE were related to post-CHF heat transfer models; however, it must be noted that only one explicitly droplet-related sensitivity parameter (droplet interfacial drag) is adjustable in TRACE. Except for that single, low-importance parameter, the rest of the impact of droplets are lumped into the TRACE post-CHF heat transfer models because of the lack of a dedicated independent droplet field in TRACE.

For the conditions of the selected FEBA test, the agreement between CTF and TRACE single-channel models are generally reasonable in terms of quench time and PCT prediction, with CTF typically predicting a slightly faster quench of the pins. The resolved CTF case generally underpredicts PCT and quench time in the center of the bundle, which indicates that there is either too much heat transfer in the DFFB heat transfer regime or not enough mixing with the periphery subchannels; however, the exact reason for this under-prediction was not found. An analysis of CTF models was showing the impact of droplet entrainment, spacer grid droplet breakup, and spacer grid quenching. Only the droplet entrainment was enabled in the FEBA validation, and it was found that this significantly lowers predicted PCT, so it is possible that this model should be reviewed. The droplet breakup and grid quench models also lower

PCT, but mainly in the top of the bundle, which was always over-predicted by both TRACE and CTF; however, not enough details were given in the FEBA specification to accurately enable these models for these validation tests, which is why they were not originally included. Enabling those models may help improve prediction in the top of the bundle.

The impact of flooding rate was investigated by modeling a second FEBA test in CTF with double the flooding rate of the initial test. It was observed that CTF correctly predicts the trend of lower PCT and faster quench compared to the low-flooding rate test; however, CTF continues to predict quench times that are faster than experimental values. PCT was generally better predicted for the high flooding-rate case, which more commonly encounters the IAFB heat transfer regime when compared to the low flooding rate test. Future activities should include further review of the DFFB heat transfer regime and should test different available models for vapor convective heat transfer and droplet heat transfer effects in CTF.

A final investigation was performed to test the impact of inlet enthalpy on PCT and quenching time. The FEBA tests do not include significant variation of inlet enthalpy, so a code-to-code benchmark was primarily used for this study. It was found that CTF was able to predict the expected trend of PCT increasing with decreasing inlet enthalpy, which is because more subcooled liquid leads to lower vaporization, lower vapor velocity, and thus lower vapor heat transfer. However, in the middle and upper regions of the bundle, CTF predicted a faster quench time for the high inlet enthalpy case, which is opposite of the expected trend. This again points to a potential issue with the DFFB heat transfer regime.

After completion of the validation of CTF and TRACE, a core-scale reflood simulation was performed using TRACE and CTF coarse-mesh models, as well as a pin-resolved CTF model. This core model included a high-burnup core loading pattern based on a VERA depletion simulation and used the FEBA flooding rate and inlet enthalpy as boundary conditions for simulating the reflood. This activity indicated reasonable agreement between the coarse mesh version of CTF and TRACE in terms of PCT. The resolved version of the model was able to capture a much wider range of pin PCT, which usually resulted in PCT that was as much as 40 K higher than the hot pin in the lumped model. The resolved model also resulted in some pins having lower PCT than the average pin in the lumped model. The discrepancy between TRACE and CTF lumped models' prediction of quenching time was more significant than that bserved in the FEBA validation case. Because boundary conditions and initial conditions were similar to those in the FEBA case, the rod geometry differences or dynamic gap conductance model may be causing the different behavior. An analysis of radial pin PCT distribution in the high-burnup assemblies revealed a clear trend of PCT being higher on the boundaries of high-burnup assemblies when those assemblies were adjacent to lower burnup, higher power assemblies. This indicates that pin power distribution alone may not be sufficient in determining location of the limiting pin in a high-burnup assembly because of the impact of cross-flow and local TH effects on PCT behavior. The culmination of the results suggests a subchannel model may predict fuel rod temperatures higher and lower than a coarse model, depending on fuel assembly and rod location within the core. FFRD susceptibility is first and foremost predicated based on whether the fuel rod ruptures, and then, depending on the chosen fuel fragmentation model, terminal temperature. The previous TRACE analysis results suggest that failure occurred in the majority of the rods in the center of the core, and the terminal temperatures in those failed rods exceeded the fuel fragmentation terminal temperature. Therefore, the results presented in this report suggest margin to FFRD susceptibility may be available if a subchannel TH code where used.

Several modifications and improvements were made to the full-system TRACE model in this work to better align the model with industry and NRC best practices and to improve the accuracy of the LBLOCA predictions. The model developed in FY22 originated from a legacy model and employed the original pipe and side junction--based approach for modeling the reactor vessel. However, this model is no longer supported by the current TRACE validation basis and lacks the important models and physics afforded by

3D vessel components. Incorporating the 3D vessel component into the TRACE model caused a significant decrease in PCT and resulted in an earlier quench time. Additional modeling improvements, including the introduction of azimuthal and radial dependence in the vessel and core, further decreased the quench time and gave a pronounced dependence of cladding temperature on core radial location. The BEMUSE LBLOCA benchmark comparisons performed in FY22 were repeated with the updated TRACE model, producing much better agreement to the published benchmark results in terms of peak PCT and quench time. The analysis of the 281 representative high-burnup fuel rods from FY22 was also repeated with the updated model, reinforcing the finding that PCT depends strongly on rod LHR and has no clear trend with rod burnup. It was found that the axial location where PCT occurs typically had a local burnup similar to the rod's average burnup. The sensitivity of the TRACE predictions to additional modeling assumptions was dalso examined to quantify the impact of these assumptions and to improve model accuracy.

An interesting finding of the TRACE full system analysis was that, although the radial TH conditions differed significantly between each of the two radial core rings, the cladding temperature variation within each ring was relatively small. This was consistent with the CTF subchannel analysis in Section 4, which demonstrated that subchannel- and pin-resolved modeling provides a significantly greater variation in cladding temperatures than lumped channel modeling. The two-ring approach allows a natural division of the core into large zones based on fuel loading patterns, with the outer ring representing the low power, twice-burned peripheral assemblies, and the inner ring representing the fresh and once-burned assemblies. The inner ring could be further split into the ring of fire high-power assemblies and the remaining innermost assemblies for further fidelity enhancement in future work. Therefore, the two-ring, four-azimuthal core model used in TRACE likely provided a reasonable approximation of TH conditions on a larger core scale. However, it does not account for the checkerboard effect of high-power (low-burnup) and low-power (high-burnup) assemblies adjacent to each other in the core interior; nor does it account for localized subchannel and neighboring assembly effects, both of which were found to be significant in the CTF subchannel analysis.

Several future activities may be undertaken to continue improving this capability. The data used for validation were limited and it would be ideal to improve on that testing database to include other LOCA experiments such as FLECHT-SEASET (Hochreiter, 1985) and RBHT (Rosal, Lin, McClellan, Brewer, & Tien, 2010), which will allow better assessment of droplet models and the impact of operating conditions. Additionally, because this report focused on the reflood phase only, the assessment should be extended to the depressurization phase. As results of this study have shown, further investigation of different models for the post-CHF heat transfer regimes in CTF is warranted. Furthermore, some CTF modeling features were not adequately tested because of limited data such as spacer grid design information, which would benefit from additional assessment if the necessary data become available. Furthermore, enabling these models in large-scale VERA models will require modifying the CTF preprocessor capability to add the new required input to the CTF input file. Further investigation into the numerics of the CTF solution is also warranted to attempt to reduce the timestep refinement requirements for large-scale pin-resolved models requiring longer run times.

Additional spatial fidelity enhancements could be made to the TRACE model to further investigate spatial TH effects and to improve predictions. The number of radial rings in the core could be increased from two to three or perhaps beyond. Alternatively, a cartesian vessel component could be implemented in the core to model the full core on an assembly-by-assembly basis using a cartesian grid. These improvements would better resolve the spatial core TH effects found to be important in this work.

7. BIBLIOGRAPHY

Bajorek, S., Bernard, M., Gingrich, C., Hoxie, C., Ireland, A., Kelly, J., . . . Whitman, J. (2015). Development, Validation, and Assessment of the TRACE Thermal-Hydraulics Systems Code. *NURETH-16.* Chicago, IL, USA.

Capps, N., Hirschhorn, J., Wysocki, A., & Greenquist, I. (2022). *Assessment of the Effect of Prototypic High-Burnup Operating Conditions of Fuel Fragmentation, Relocation, and Dispersal Susceptibility.* Oak Ridge, TN: Oak Ridge National Laboratory.

Capps, N., Wysocki, A., Godfrey, A., Collins, B., Sweet, R., Brown, N., . . . Hoxie-Key, S. (2021). Full core LOCA safety analysis for a PWR containing high burnup fuel. *Nuclear Engineering and Design (379)*, 111194.

Clifford, I., & Ferroukhi, H. (2021). Assessing the effects of switching from multi-channel to three-dimensional nodalisations of the core in TRACE. *Nuclear Engineering and Design, 383*(11446).

Dalbey, K., et al., "Dakota, A Multilevel Parallel Object-Oriented Framework for Design Optimization, Parameter Estimation, Uncertainty Quantification, and Sensitivity Analysis: Version 6.16 Theory Manual", Sandia National Laboratories, SAND2022-6172, 2022.

Flanagan, M., Askeljung, P., & Purana, A. (2013). *Post-Test Examination Results from Integral High Burnup Fueled LOCA Test at Studsvik Nuclear Laboratory.* US NRC, Office of Nuclear Regulatory and Rsearch, NUREG-2160.

Faya, A., Wolf, L., and Todreas, N. *Canal Users Manual*. MIT-EL-79-028. 1979.

Gordon, N., Gilkey, L., Blyth, T., Smith, R., Tatli, E., Sung, Y. *Initial Application of Hi2Lo Approach to Turbulent Mixing Model Improvement L3:AMA.CP.P14.04*. Consortium for Advanced Simulation of Light Water Reactors. CASL-X-2017-1292-000. 2017.

Greenquist, I., Wysocki, A., Hirschhorn, J., & Capps, N. (2023). Multiphysics Analysis of Fuel Fragmentation, Relocationa, and Dispersal Susceptibility--Part 1: Overview and Code Coupling Strategies. *Annals of Nuclear Energy, 191*(109913). doi:https://doi.org/10.1016/j.anucene.2023.109913

Hales, J., Williamson, R., Novascone, S., Pastore, G., Spencer, B., Stafford, D., . . . Liu, W. (2016). *BISON Theory Manual: The Equations behind Nuclear Fuel Analysis.* Idaho National Laboratory (INL/EXT-13-29930 Rev 3).

Hochreiter, L. (1985). *FLECHT-SEASET Program Final Report.* Westinghouse Electric Company, NUREG/CR-4167.

Ihle, P., & Rust, K. (1984). *FEBA---Flooding Experiments with Blocked Arrays Data Report 1, Test Series I through IV.* Institut fur Reaktorbauelemente Projekt Nukleare Sicherheit, KfK 3658.

Ihle, P., & Rust, K. (1984). *FEBA---Flooding Experiments with Blocked Arrays Evaluation Report, KfK 3657.* Institut fur Reaktorbauelemente Projekt Nukleare Sicherheit.

Kropaczek, D., "Consortium for Advanced Simulation of Light Water Reactors: CASL Phase II Summary Report", Consortium for Advanced Simulation of Light Water Reactors, CASL-U-2020-1974-000, ORNL/SPR-2020/1759, 2020.

Martin, R., & O'Dell, L. (2005). AREVA's realistic large break LOCA analysis methodology. *Nuclear Engineering and Design, 235*(16), 1713-1725.

R. Salko, B. Hizoum, A. Graham, B. Collins, M. Asgari, "Summary of CTF Modeling and Numerical Improvements for Boiling Water Reactor Simulations", Oak Ridge National Laboratory, ORNL/TM-2021/2004, 2021.

R. Salko, A. Wysocki, B. Hizoum, N. Capps (2023). Assessment and Testing of CTF for LOCA Reflood Conditions. *The 20th International Topical Meeting on Nuclear Reactor Thermal Hydraulics (NURETH-20).* Washington, D.C.

R. Salko, et al., "CTF: A modernized, production-level, thermal hydraulic solver for the solution of industry-relevant challenge problems in pressurized water reactors", Nuclear Engineering and Design (397), 2022, https://doi.org/10.1016/j.nucengdes.2022.111927.

Rosal, E., Lin, T., McClellan, I., Brewer, R., & Tien, K. (2010). *Rod Bundle Heat Transfer Test Facility Description.* US Nuclear Regulatory Commision, NUREG/CR-6976.

Shaw, R., Larson, T., & Dimenna, R. (1988). *Development of a phenomena identification and ranking table (PIRT) for thermal-hydraulic phenomena during a PWR LBLOCA.* NUREG/CR-5074.

T. Fuketa, F. N. (2010). *Safety Significance of the Halden IFA-650 LOCA Test Results.* Nuclear Energy Agency of the OECD (NEA).

Thurgood, M., Kelly, J., Guidotti, T., Kohrt, R., & Crowell, K. (1982). *COBRA/TRAC - A Thermal-Hydraulic Code for Transient Analysis of Nuclear Reactor Vessels and Primary Coolant Systems: Equations and Constitutive Models.* Pacific Northwest Laboratory (NUREG/CR-3046).

US Nuclear Regulatory Commission. (2012). *TRACE V5.0 Assessment Manual: Main Report.* Washington, D.C., USA: ADAMS Accession Number ML120060208.

US Nuclear Regulatory Commission. (2022). *TRACE V5.0 Developmental Assessment, Addendum 7A: V5.0 Patch 7.* Washington, D.C., USA.

Williamson, R., Gamble, K., Perez, D., Novascone, S., Pastore, G., Gardner, R., . . . Mai, A. (2016). Validating the BISON fuel performance code to integral LWR experiments. *Nuclear Engineering and Design, 301*, 232-244.

Wysocki, A., Salko, R., & Arshavsky, I. (2023). Coupling of CTF and RELAP5-3D within an enhanced fidelity nuclear power plant simulator. *Nuclear Technology*.

Young, M., Bajorek, S., Nissley, M., & Hochreiter, L. (1998). Application of code scaling applicability and uncertainty methodology to the large break loss of coolant. *Nuclear Engineering and Design, 186*(1-2), 39-52.